

Performance Characterisation and
Cavitation Detection of Variably Angled
V-Shaped Opening Ball Valves

Performance Characterisation and Cavitation Detection of Variably Angled V-Shaped Opening
Ball Valves

By
Ali Mahdavi Rad, B.A.I.

A THESIS
Submitted to the School of Graduate Studies
in Partial Fulfillment of the Requirements
for the Degree
Master of Applied Science

McMaster University
Hamilton, Ontario, Canada

© Copyright by Ali Mahdavi Rad, October 2013, all rights reserved.

Permission to Use

In presenting this thesis in partial fulfillment of the requirements for a Postgraduate degree from McMaster University, I agree that the Libraries of this University may make it freely available for inspection. I further agree that the permission for copying this thesis in any manner, in whole or in part for scholarly purposes, may be granted by the professors who supervised my thesis work or, in their absence, by the Head of the Department or the Faculty Dean in which my thesis work was conducted. It is understood that any copying or publication or use of this thesis or parts thereof for financial gain shall not be allowed without my written permission. It is also understood that due recognition shall be given to me and McMaster University in any scholarly use which may be made of any material in my thesis. Requests for permission to copy or to make other use of material in this thesis, in whole or part, should be addressed to:

Head of the Department of Mechanical Engineering
McMaster University
Faculty of Engineering
1280 Main Street West
Hamilton, Ontario L8S 4L6
Canada

MASTER OF APPLIED SCIENCE (2013)
(Department of Mechanical Engineering)

McMaster University
Hamilton, Ontario, Canada

BACHELOR OF ART OF ENGINEERING (2011)
(Department of Mechanical Engineering)

Trinity College Dublin
Dublin, Rep. of Ireland

TITLE: Performance Characteristics and Cavitation Detection
of Variable Angled V-Shaped Opening Ball Valves

AUTHOR: Ali Mahdavi Rad

SUPERVISOR: Dr. James Cotton

NUMBER OF PAGES: xxiii, 168

Abstract

The objectives of this thesis are to characterise the performance of variably angled V-shaped opening ball valves in terms of pressure drop and cavitation. Both numerical and experimental techniques are utilised here to study the effects of apex angle of the V-opening on pressure drop and cavitation characteristics. Three different ball sizes are used to investigate scalability of the V-ball valves in terms of cavitation inception and pressure coefficient. The results of the pressure drop experiments show that as the size of the ball and the apex angle of the valve increases, the pressure coefficient tends towards a constant value. This means that larger V-opening ball valves can be scaled using pressure coefficient within 17.5%.

It has been well established that cavitation causes high frequency noise. Therefore dynamic pressure transducers were used to detect acoustic cavitation noise by considering the high energy content in the 2 kHz to 45 kHz frequency band. To measure the energy levels, spectral analysis was performed and the power spectrum density was acquired using fast Fourier transform algorithm and the area under the curve was integrated in three different frequency intervals of 2 to 5 kHz, 5 to 10 kHz and 10 to 45 kHz to capture the frequency band at which cavitation onset occurs. This energy was compared to the reference energy levels in the same frequency intervals when no valve was installed. Two criteria were chosen to represent a cavitating flow, the first criteria was the start of a steep exponential increase in the energy from the reference energy in at least one of the frequency ranges defined and the second criteria is an increase in the coherence function

in any of the three frequency ranges. This procedure was performed for all valves tested at 10% opening increments starting at fully open position and the inception cavitation number was recorded to define the onset of cavitation. It was observed that as the apex angle decreases, cavitation number also decreases where the size of the valve did not affect cavitation number. The conclusion was that as the opening decreases, cavitation inception occurs at higher pressure drops. However some deviations from this general trend were observed. These deviations are perhaps due to the turbulent structures such as flow separation and vortices, suggested by the pressure fluctuations in the static pressure.

Finally numerical modelling of 1 inch 60V valves were performed using ANSYS Fluent computational fluid dynamics (CFD) software for three openings using two different turbulence models, standard $k-\epsilon$ and SST $k-\omega$. The results were contrasted against the experimental data to evaluate which model performs the best for this application. From the results obtained, standard $k-\epsilon$ predicts the pressure drop within 15% of the experimental data. Also flow separation is a major cause of high local pressure drops and therefore cavitation and SST $k-\omega$ predicts cavitation better than standard $k-\epsilon$. This is due to better performance of SST $k-\omega$ at predicting turbulence characteristics of flow separation region.

Acknowledgments

First of all I would like to show my gratitude to my supervisor Dr. Jim Cotton, who has provided excellent guidance, support and motivation to me throughout this project without which the completion of this thesis would have not been possible. His superior knowledge of fluid mechanics and two phase flows and constant motivation were most valuable. Also I would like to thank Dr. Chan Ching who has provided me with notable suggestions and has motivated me with his exceptional quotes. I would like to thank my parents for their constant support although they were far away. I would also like to thank Dr. Ross L. Judd and Dr. Samir Ziada for the interesting and constructive discussions.

I would like to acknowledge the kind guidance and practical solutions, the Mechanical Engineering Department technicians, namely Jim McLaren, Joe Verhaghe, Michael Lee, Mark Mackenzie and Ron Lodewyks provided to me throughout this thesis. Furthermore I would like to thank National Science and Engineering Research Council (NSERC) and Gosco valves CEO, Tom Gosling who has provided financial support which made the completion of this project viable. Last but not the least I would like to thank Gosco Valve engineering department who have provided me with all the valves I needed within a short time frame and have taught me practical engineering approaches during my time at Gosco Valves as a part of my scholarship.

Table of Contents

Permission to Use	iii
Abstract	v
Acknowledgments.....	vii
Table of Contents	viii
Table of Figures	xii
Nomenclature	xxii
1. Introduction.....	1
2. Literature Review.....	5
2.1. Bubble Formation and Growth.....	5
2.1.1 Bubble Formation and Collapse Modelling.....	6
2.1.2 Cavitation Damage Causation.....	10
2.1.3 Cavitation Noise.....	13
2.1.4 Cavitation Effects on Hydrodynamic Performance	17
2.2. Cavitation Quantification	18
2.3. Cavitation in Fluids	21
2.4. Internal Flows and Non-visual Detection Techniques	31
2.5. Ball Valve Characterisation	38

2.6.	Numerical Investigations of Pressure Drop and Cavitation	40
3.	The Experimental Facility	44
3.1.	The Test Section	46
3.1.1	The Ports	47
3.2.	The Sensors & Signal Conditioning	48
3.3.	Experimental Procedure:	51
3.4.	Data Acquisition and Analysis Program:	52
4.	Results and Discussion	57
4.1.	Pressure Drop Performance	57
4.1.1	Effects of Reynolds Number on Flow Coefficient	57
4.1.2	Effects of Valve Opening on Pressure Drop Performance	60
4.1.3	Pressure Coefficient and Scalability of Valves	63
4.1.4	Summary	68
4.2.	Cavitation Detection	68
4.2.1	Frequency Range Establishment	69
4.2.2	Cavitation Detection Using Dynamic Pressure	73
4.2.3	Cavitation Detection Using Accelerometer	82
4.2.4	Discussion of Frequency Spectral Behaviour	90
4.2.5	Cavitation Inception Characteristics	93

4.3.	Cavitation Damage	102
4.4.	Summary	103
5.	Numerical Investigations	104
5.1.	Numerical Study Methodology	104
5.1.1	The Model	104
5.1.2	Solution Method.....	107
5.1.3	Inlet Boundary Condition Justification	108
5.1.4	The Turbulence Models	109
5.1.5	Grid Independence Study	110
5.2.	Numerical Results	111
5.2.1	Flow Coefficient Determination	111
5.2.2	Cavitation Detection Determination	117
5.3.	Summary	131
6.	Conclusions	132
6.1.	Future Work	134
7.	Appendices	135
Appendix A.	Geometry of Ball Valves	136
	The Ball Valve	136
Appendix B.	Standard Port Results	139

Appendix C. Derivations	142
Flow Coefficient	142
Appendix D. Error Analysis	144
Appendix E. Pressure Fluctuations.....	156
Appendix F. Scaling Example.....	158
Appendix G. Computational Grid.....	159
References	161

Table of Figures

Figure 2-1 Numerical study of bubble collapse stages from an initial spherical bubble [9]	11
Figure 2-2 Comparison of numerical and experimental bubble shape in different stages of bubble collapse, solid lines represent numerical predictions and open circles represent the experimental data [10]	12
Figure 2-3 Radiated sound spectrum of a cavitation bubble [11]. The dashed lines indicate the asymptotic cut off frequency for a given condition as investigated by Fitzpatrick et al. [11]	14
Figure 2-4 Frequency spectrum of the noise generated in a cavitating spool valve at different cavitation numbers as observed by [13]. The graph was reproduced by [8] in higher quality.	15
Figure 2-5 Average frequency spectrum of cavitation acoustic noise generated for different cavitation numbers [14].....	16
Figure 2-6 System Pressure operating under different ambient pressures with the same velocity.....	20
Figure 2-7 the hemispherical body with a step, $Re = 3.6 \times 10^5$ [19]. Note the 1 mm step after the hemisphere.	23
Figure 2-8 Cavitation inception probability within nearfield of the jet. Ran et al. [24]	27
Figure 3-1 Schematic of the test facility	44
Figure 3-2 Front View of the Test Section	47

Figure 3-3 Assembly of the pressure transducer port	48
Figure 3-4 Schematic of the static pressure measurement monitoring system	49
Figure 4-1 Variations of flow coefficient with Reynolds number for 2 inch 60V full port valve	58
Figure 4-2 Variations of flow coefficient with Reynolds number for 1 inch 60V standard port valve	58
Figure 4-3 Variations of flow coefficient with Reynolds number for 1 inch 30V standard port valve at various openings	59
Figure 4-4 Variations of flow coefficient with opening for 1 inch full port valves with different inlet V apex angles	60
Figure 4-5 Variations of flow coefficient with opening for 1.5 inch full port valves with different inlet V apex angles	61
Figure 4-6 Variations of flow coefficient with opening for 2 inch full port valves with different inlet V apex angles	61
Figure 4-7 Variations of flow rate with change in valve opening for 2 inch full port valves with different V apex angles. (Arbitrary constant pressure drop, 10 psi)	62
Figure 4-8 Pressure coefficient vs. valve opening for different sizes of 10V full port valves	64
Figure 4-9 Pressure coefficient vs. valve opening for different sizes of 30V full port valves	64
Figure 4-10 Pressure coefficient vs. valve opening for different sizes of 60V full port valves	65

Figure 4-11 Pressure coefficient vs. valve opening for different sizes of 90V full port valves	65
Figure 4-12 Coherence function between upstream and downstream pressure transducers	71
Figure 4-13 Coherence function between downstream accelerometer and downstream pressure transducers	71
Figure 4-14 Power spectrum density of the upstream dynamic pressure transducer (No Valve).....	72
Figure 4-15 Power spectrum density of the downstream dynamic pressure transducer (No Valve).....	72
Figure 4-16 Power spectrum density of the accelerometer (No Valve).....	73
Figure 4-17 Energy of upstream pressure transducer in the 2 to 5 kHz frequency range (No Valve)	74
Figure 4-18 Energy of downstream pressure transducer in the 2 to 5 kHz frequency range (No Valve)	74
Figure 4-19 Energy of upstream pressure transducer in the 5 to 10 kHz frequency range (No Valve)	75
Figure 4-20 Energy of downstream pressure transducer in the 5 to 10 kHz frequency range (No Valve)	75
Figure 4-21 Energy of the upstream pressure fluctuations in the 10 to 45 kHz frequency range (No Valve).....	76

Figure 4-22 Energy of downstream pressure fluctuations in the 10 to 45 kHz frequency range (No Valve).....	76
Figure 4-23 Upstream 2 to 5 kHz frequency range energy level for 1 inch 30V Standard Port valve vs. no valve installed for some openings	78
Figure 4-24 Downstream 2 to 5 kHz energy level for 1 inch 30V standard port valve vs. no valve installed for some openings	78
Figure 4-25 Upstream 5 to 10 kHz frequency range energy level for 1 inch 30V Standard Port valve vs. no valve installed for various openings.....	79
Figure 4-26 Downstream 5 to 10 kHz frequency range energy level for 1 inch 30V Standard Port valve vs. no valve installed for various openings	80
Figure 4-27 Upstream 10 to 45 kHz frequency range energy level when for 1 inch 30V Standard Port valve vs. no valve installed for various openings	80
Figure 4-28 Downstream 10 to 45 kHz frequency range energy level when for 1 inch 30V Standard Port valve vs. no valve installed for various openings	81
Figure 4-29 Energy of accelerometer in the 2 to 5 kHz frequency range (No Valve).....	83
Figure 4-30 Energy of accelerometer in the 5 to 10 kHz frequency range (No Valve).....	83
Figure 4-31 Accelerometer 2 to 5 kHz energy level for 1 inch 30V Standard Port valve vs. no valve installed for various openings	84
Figure 4-32 Accelerometer 5 to 10 kHz frequency range energy level for 1 inch 30V Standard Port valve vs. no valve installed for various openings	85
Figure 4-33 Accelerometer output in time domain, Pipe Reynolds number = 138,200	87

Figure 4-34 Accelerometer under non cavitating operation for 1 inch 30V standard port valve 100% open	88
Figure 4-35 Accelerometer under intermittent cavitation inception operation for 1 inch 30V standard port valve 100% open	88
Figure 4-36 Accelerometer under onset of fully developed cavitation operation for 1 inch 30V standard port valve 100% open	89
Figure 4-37 Inception cavitation number vs. opening for 1 inch full port valves.....	94
Figure 4-38 Inception cavitation number vs. opening for 1.5 inch full port valves.....	95
Figure 4-39 Inception cavitation number vs. opening for 2 inch full port valves.....	95
Figure 4-40 Comparison of inception cavitation number vs. opening for three different sizes of full port 90V valves	96
Figure 4-41 Comparison of inception cavitation number vs. opening for three different sizes of full port 60V valves	97
Figure 4-42 Comparison of inception cavitation number vs. opening for three different sizes of full port 30V valves	97
Figure 4-43 Comparison of inception cavitation number vs. opening for three different sizes of full port 10V valves	98
Figure 4-44 Standard deviation of pressure fluctuations for different 10V FP valves	100
Figure 4-45 Variation of average of standard deviations for different openings.....	100
Figure 4-46 Pitting damage caused by cavitation inside of a 1 inch standard port 60V valve (Diameter of the bore = 0.75 in).....	103

Figure 5-1 Graphical representation of 1 inch 60V full port valve at 70% Opening, The light blue is the effective opening	105
Figure 5-2 Inlet grid geometry, the yellow grid indicates wall and the blue mesh is inlet of the ball valve	105
Figure 5-3 Outlet grid geometry, the yellow grid indicates wall and the blue mesh is outlet of the ball valve.....	106
Figure 5-4 Computational domain of 1 inch 60V full port.....	106
Figure 5-5 Comparison of velocity profile of 8D upstream pipe model at 2 diameters upstream of the valve vs. fully developed velocity profile (35D velocity profile).....	109
Figure 5-6 Comparison of pressure drop prediction of different grid size for 50% open valve at $Re = 63000$ using standard $k-\epsilon$	111
Figure 5-7 Comparison of pressure drop predicted by standard $k-\epsilon$ for various pipe Reynolds numbers for 1 inch 60V Full port at 50% opening	112
Figure 5-8 Comparison of pressure drop predicted by SST $k-\omega$ for various pipe Reynolds numbers for 1 inch 60V Full port at 50% opening	112
Figure 5-9 Comparison of numerical predictions of pressure drop vs. experimental results for 1 inch 60V Full port valve at 100% opening.....	113
Figure 5-10 Comparison of numerical predictions of pressure drop vs. experimental results for 1 inch 60V Full port valve at 70% opening	114
Figure 5-11 Comparison of numerical predictions of pressure drop vs. experimental results for 1 inch 60V Full port valve at 50% opening	114

Figure 5-12 Comparison of CFD predictions of SST k- ω , standard k- ϵ and Gosco CFD and the experimental data for three different openings	115
Figure 5-13 Minimum absolute pressure vs. cavitation number prediction of different turbulence models at 70% open	118
Figure 5-14 Minimum absolute pressure vs. cavitation number prediction of different turbulence models at 50% open	118
Figure 5-15 Comparison of cavitation inception prediction of different turbulence models vs. experimental data	120
Figure 5-16 Downstream 2 to 5 kHz frequency range energy level for 1 inch 60V Full Port valve vs. no valve installed for various openings.....	120
Figure 5-17 Pressure contours predicted by standard k- ϵ for 1 inch 60V FP valve at 70% opening, Re = 88,900 near the apex.....	122
Figure 5-18 Pressure contours predicted by standard k- ϵ for 1 inch 60V FP valve at 70% opening, Re = 88,900 in the middle of the pipe.....	122
Figure 5-19 Pressure contours predicted by standard k- ϵ for 1 inch 60V FP valve at 70% opening, Re = 88,900 near the base of the V	123
Figure 5-20 Top view of the pressure contours predicted by standard k- ϵ for 1 inch 60V FP valve at 70% opening. The cut plane is the symmetry plane	123
Figure 5-21 Velocity contours predicted by standard k- ϵ for 1 inch 60V FP valve at 70% opening at Re = 88,900 in the pipe mid plane	124
Figure 5-22 Velocity contours predicted by standard k- ϵ for 1 inch 60V FP valve at 70% opening at Re = 88,900 in the pipe mid plane	124

Figure 5-23 Velocity contours predicted by standard k- ϵ for 1 inch 60V FP valve at 70% opening at $Re = 88,900$ in the pipe mid plane	125
Figure 5-24 Top view of the velocity contours predicted by standard k- ϵ for 1 inch 60V FP valve at 70% opening. The cut plane is the symmetry plane	125
Figure 5-25 Velocity vector field predicted by standard k- ϵ for 1 inch 60V FP valve at 70% opening, $Re = 88,900$. The vector field is zoomed in the first half of the ball valve after the step of the V. The black circles show the probable trajectory of cavitation bubble convection	127
Figure 5-26 Velocity contours predicted by SST k- ω for 1 inch 60V FP valve at 70% opening at $Re = 88,900$ near the apex	128
Figure 5-27 Velocity contours predicted by SST k- ω for 1 inch 60V FP valve at 70% opening at $Re = 88,900$ in the pipe mid plane	128
Figure 5-28 Velocity contours predicted by SST k- ω for 1 inch 60V FP valve at 70% opening at $Re = 88,900$ near the base of the V	128
Figure 5-29 Top view of the velocity contours predicted SST k- ω for 1 inch 60V FP valve at 70% opening. The cut plane is the symmetry plane.....	129
Figure 5-30 Velocity vector field predicted by SST k- ω for 1 inch 60V FP valve at 70% opening, $Re = 88,900$. The vector field only shows the first half of the ball valve after the step of the V. The black circle shows the probable trajectory of a cavitation bubble	129
Figure 5-31 Velocity contours predicted by SST k- ω for 1 in. 60V FP valve at 50% opening, $Re = 63,500$	130
Figure 7-1 Blank Ball Drawing (Courtesy of Gosco Valves).....	136

Figure 7-2 Drawing of the 60V ball valve; as the angle of the V changes, the drawing is changed accordingly. (Courtesy of Gosco Valves).....	137
Figure 7-3 Full port valve; the diameter of the flange does not change and it is the same as the piping.	138
Figure 7-4 Standard port valve; the diameter of the flange changes from the size of the piping to the next smaller size (red dashed lines)	138
Figure 7-5 Variations of flow coefficient with opening for 1 inch standard port valves with different apex angles	139
Figure 7-6 Variations of flow coefficient with opening for 1.5 inch standard port valves with different apex angles	139
Figure 7-7 Variations of flow coefficient with opening for 2 inch standard port valves with different apex angles	140
Figure 7-8 Inception cavitation number vs. opening for 1 inch standard port valves.....	140
Figure 7-9 Inception cavitation number vs. opening for 1.5 inch standard port valves ..	141
Figure 7-10 Inception cavitation number vs. opening for 2 inch full port valves.....	141
Figure 7-11 Pressure calibration curve for Honeywell 50 psi gauge pressure transducer	152
Figure 7-12 Pressure calibration curve for Honeywell 25 psi gauge pressure transducer	153
Figure 7-13 Pressure calibration curve for Honeywell 2.5 psi gauge pressure transducer	153

Figure 7-14 Pressure calibration curve for Validyne DP 15 differential pressure transducer	154
Figure 7-15 Flow rate calibration curve for Omega FTB-1425 Flow meter	154
Figure 7-16 Calibration Sheet of the accelerometer	155
Figure 7-17 Valve pressure determination methodology.....	156
Figure 7-18 Standard deviation of pressure fluctuations in the pipe when a valve is installed compared to no valve case scenario	157

Nomenclature

Symbols

A_d	Cross Sectional Area	k	Turbulent Kinetic Energy
C	Constant	P_b	Bubble Pressure
Coh_{xy}	Coherence between x and y	P_∞	Bulk Pressure
C_{ih}	Isochoric Heat Capacity	\bar{P}	Average Pressure
C_p	Pressure Coefficient	p'	Pressure Fluctuation Power
C_v	Flow Coefficient	PSD	Spectral Density Flow Rate
D	Diameter	Q	Heat Flux
D_h	Hydraulic Diameter	Q_h	Radius
E	Energy	R	Pipe Reynolds Number
f	Frequency	Re	Surface Tension
G_{xy}	Cross Correlation of x and y	S	Sound Pressure Level
G_{xx}	Auto-Spectral Density of x	SPL	Specific Gravity
G_{yy}	Auto-Spectral Density of y	SG	Temperature
H	Head	T	Time
H_{SH}	Suction Head	t	Velocity
I_t	Turbulent Intensity	u	
K_a	Ooi Scaling Factor		
L_t	Turbulent Kinetic Energy		

Greek Symbols

Γ_s	Circulation	<i>abs</i>	Absolute
Δ	Difference	<i>c</i>	Critical
γ	Specific Weight	<i>down</i>	Downstream
δ	Uncertainty	<i>g</i>	Permanent Gas
ε	Turbulent Dissipation Rate	<i>i</i>	Initial Condition
ϵ	Small Change	<i>in</i>	Inlet
κ	Adiabatic Constant	<i>l</i>	Liquid
λ	Polytropic Constant	<i>out</i>	Outlet
μ	Dynamic Viscosity	<i>up</i>	Upstream
ν	Kinematic Viscosity	<i>v</i>	Vapour
ρ	Density	∞	Bulk Property
σ	Cavitation Number		
τ	Time Constant		
ω	Angular Frequency		

Subscripts

0	Reference
1	Condition 1, Position 1
2	Condition 2, Position 2
<i>amb</i>	Ambient

1. Introduction

In industrial processes, controlling the flow rate or achieving a certain pressure drop is necessary for the operation of the plant. This is achieved often by using regulatory valves as a mean of passive control of the flow rather than changing the input to the pump or the compressor. There are many different types of regulatory valves used in the industry today, ball valves being one of them. A ball valve can be placed in fully open position by turning the stem only by 90 degrees or performing a “quarter turn”. This allows for more accurate control of the position of the valve compared to other types of valves where a gear controls the regulation of the opening. The fine control of a ball valve has made them an interesting choice for flow and pressure regulatory operations to achieve the required flow rates or pressure drops.

Gosco Valves manufactures ball valves for shut off and flow control purposes. The control valves have V-shaped openings on the inlet and a circular opening on the downstream side. The pneumatic controller on these valves ensures the required opening with very small error making them suitable for high performance applications and therefore understanding their exact performance characteristics at a given opening is very important.

The first variable is the flow coefficient of a valve commonly referred to as C_v which relates the opening with the amount of flow passing through it at a given pressure drop. It is preferred to design the valve such that it does not change with Reynolds number so it

becomes constant for a given position to reduce the number of variable for control purposes.

Another issue which exists in most hydraulic systems is cavitation. Cavitation is the term given to the phenomena where a bubble is formed due to a drop in pressure and then collapsed as a result of pressure recovery. This term was suggested by Froud [1] who has used the Latin word "*cavus-a-um*" meaning "hollow" to name this phenomenon [2]. Cavitation was initially noted in the design of battleships in the nineteenth century as it caused severe underperformance in a vessel that was supposedly the fastest battleship designed at the time. This phenomenon causes severe damage to fluid machinery, dams, tunnels, etc. in the form of pitting and mass transfer. This issue is observed in all types of valves and the occurrence of cavitation in ball valves is eventually unavoidable if the pressure drop is large enough.

In the present work, pressure drop performance of Vari-V ball valves produced by Gosco Valves is investigated. Also scaling of valves is attempted as testing large valves with large flow rates and high pressure drops is not possible in the experimental facility. An effort is made to investigate and identify trends in these valves with increasing ball diameters or a change in the apex angle of the upstream opening.

An experimental investigation of cavitation occurrence will also be performed. Since cavitation causes severe damage to different components of the valves, the operating conditions which involve cavitation must be identified. These conditions should be avoided or harder materials should be used to ensure cavitation does not shorten the life

span the valve was designed for. However there are some challenges to the cavitation detection techniques used. Using flow visualisation was not a viable option as the size of the bubbles are in the order of μm in diameter at cavitation inception and the resolution and focus of the camera becomes a serious issue. This means a method must be employed which does not require optical visualisation of the flow and yet is as effective and reliable.

Another issue with cavitation is the increased pressure drop and the deviation from expected predictions. If cavitation occurs and the flow coefficient reduces, then non-cavitating data is no longer applicable. This will cause problems for the operating plant and the valve manufacturer and will result in error.

The aim of the cavitation investigations are also to compare the performance of different valves to understand the important factors in cavitation and characterise cavitation occurrence in a valve with respect to the opening of the valve and the size of the ball. Also the possibility of scaling cavitation in a valve using a dimensional analysis is investigated since larger valves cannot be tested in the experimental facility and scaling will provide valuable data for larger ball sizes.

A numerical investigation is also performed. Gosco Valves have used SolidWorks Flow Simulator to estimate the pressure drop in their valves. However, some discrepancies between the numerical solution and the experimental studies existed. A numerical methodology is developed here to estimate the pressure drop and evaluate the best

turbulence model for the application and develop a numerical technique for cavitation onset identification validated by experimental studies.

2. Literature Review

One of the most important problems encountered when characterising the performance of a valve is cavitation. A background theory and literature review is provided to improve the understanding of the problem, the causes of cavitation and the flow phenomena which accelerate occurrence of cavitation. In addition pressure drop characteristics of a ball valve is one of the most important aspects of performance of a valve which is also introduced and discussed in detail in this literature review.

2.1. Bubble Formation and Growth

Cavitation is the same mechanism as boiling except it has a different thermodynamic path. Cavitation occurs as a result, by reducing the pressure in an ideally isothermal process and then recovering the pressure which causes bubble collapse. The first section is only concerned with formation of a bubble and the background theory surrounding this issue.

In cavitation, the regions of high velocity and low pressure are normally in the bulk of the fluid away from the surfaces. This means that nucleation seeds are required to be available in the bulk of the flow rather than the solid boundaries. One of the commonly acceptable explanations is the existence of nucleation seeds suspended in the flow. Harvey et al. [3] have performed analysis and experiments with bubbles in capillaries and small surfaces and proposed the formation of nucleation seeds on cells in animals. Also in the same study the other nucleation seeds identified are the gas bubbles. When micro air

bubbles are present, they allow vapour formation by homogenous nucleation or fast mass diffusion. As the local pressure reaches the vapour pressure, the vapour will diffuse into the air bubble creating an air-vapour bubble which will then increase the size of the initial gas bubble. A set of theoretical equations were developed to explain these analytically which will be discussed here.

2.1.1 Bubble Formation and Collapse Modelling

As the pressure drops below the vapour pressure, a bubble starts to form which overcomes the tensile strength of the liquid. Assuming a spherical bubble, with an internal pressure P_b , the differential pressure between the two boundaries of the bubble is given by:

$$P_b = P_\infty + \frac{2S}{R} \quad 2.1$$

From equation 2.1, it can be observed that as the local pressure within the bulk of the fluid drops below the vapour pressure, a bubble will form and as long as equation 2.1 is not satisfied, the radius of the bubble will continue to change. In a pressure recovering flow such as that after an orifice or a nozzle, the bulk pressure (P_∞) recovers and increases and assuming the pressure within the bubble (P_b) to be constant, R will decrease until equation 2.1 is satisfied.

However the model above is a very simplistic model. The change of radius of the bubble is a function of upstream pressure changes and it has a dynamic behaviour. The investigation of changes in bubble size due to pressure changes has been extensively

studied in the past 100 years due to the destructive effects of bubble formation and collapse. Rayleigh [4] was the first researcher to consider the collapse of a cavity and provided an analysis. In this analysis Lord Rayleigh has neglected surface tension, liquid viscosity and also assumed incompressible liquid. Starting with momentum equation in spherical coordinates one can reduce the equation to the form:

$$R \frac{\partial^2 R}{\partial^2 t} + \frac{3}{2} \left(\frac{\partial R}{\partial t} \right)^2 = \frac{P_\infty - P_b}{\rho_l} \quad 2.2$$

Plesset [5] has included the surface tension effects in the equation using a force balance at the bubble surface. The net force acting at the bubble surface is given by:

$$\text{Radial Stress} + P_b - \frac{2S}{R} \quad 2.3$$

Where the radial stress itself is given by:

$$\text{Radial Stress} = -P_R + \frac{2\mu_l}{R} \frac{\partial u}{\partial r} \quad 2.4$$

If no mass transport occurs between the bubble and the liquid, then equation 2.3 will be equal to zero and therefore:

$$\frac{P_b(t) - P_\infty}{\rho_l} = R \frac{d^2 R}{dt^2} + \frac{3}{2} \left(\frac{dR}{dt} \right)^2 + \frac{4\mu_l}{R} \frac{dR}{dt} + \frac{2S}{\rho_l R} \quad 2.5$$

In the above equation, pressure variations govern the change in the radius of a bubble and dictate whether the bubble radius increases or decreases or in an extreme case, collapses.

The effects of undissolved gas bubbles present in the fluid were included by Noltingk and Nepiras [6] into the equation. They were concerned with ultrasonic induced cavitation and therefore they based their argument on a pressure field represented by two components where an oscillating pressure field is superimposed on an average static pressure, the same as a time variable pressure component proposed by [5] where the time variability of pressure is known. Assuming an isothermal volume change in the gas bubble and neglecting viscous effects the above equation becomes:

$$\frac{-P_{\infty} + \left(P_{\infty} + \frac{2S}{R}\right)\left(\frac{R_0}{R}\right)^3}{\rho_l} = R \frac{d^2 R}{dt^2} + \frac{3}{2} \left(\frac{dR}{dt}\right)^2 + \frac{2S}{\rho_l R} \quad 2.6$$

The effects of viscosity on the Rayleigh Plesset equation were initially investigated by Portisky [7]. Poritsky showed that if the effects of viscosity were to be included in the original equation, they will cancel out and the effects will only be included in the boundary condition which reduces the complexity of analysis. Also non-dimensionalised radii and pressure were used to solve the equations numerically for a given liquid pressure and initial radius size. When this analysis was combined with that of Noltingk et al. [6] a more complete equation can be obtained which describes collapse and the growth of a bubble more accurately.

$$\begin{aligned} \frac{P_v(T_{\infty}) - P_{\infty} + \left(P_{\infty} + \frac{2S}{R}\right)\left(\frac{R_0}{R}\right)^3}{\rho_l} \\ = R \frac{d^2 R}{dt^2} + \frac{3}{2} \left(\frac{dR}{dt}\right)^2 + \frac{4\nu_l}{R} \frac{dR}{dt} + \frac{2S}{\rho_l R} \end{aligned} \quad 2.7$$

One must note that in the analysis performed above it was assumed that a permanent gas bubble exists which is in equilibrium with surroundings and has a partial pressure of:

$$P_g = P_\infty + \frac{2S}{R} \quad 2.8$$

where subscript g denotes a bubble made of permanent gases only.

Brennen [8] has improved the presentation of 2.7 to include the effects of thermal boundary condition of the bubble rather than assuming isothermal bubble:

$$\frac{P_v(T_\infty) - P_\infty + P_g \left(\frac{R_0}{R}\right)^{3\lambda}}{\rho_l} = R \frac{d^2 R}{dt^2} + \frac{3}{2} \left(\frac{dR}{dt}\right)^2 + \frac{4v_l}{R} \frac{dR}{dt} + \frac{2S}{\rho_l R} \quad 2.9$$

Here λ is the polytropic constant. In the equation above if the value of λ is equal to 1, then the bubble is assumed to be isothermal and if λ has the value of adiabatic constant (κ) then the change in bubble size is adiabatic. This is an improvement since it considers the thermodynamic process in which the bubble changes occur whether heat transfer also occurs or not.

By considering equation 2.9 and imposing a small change in the equilibrium radius such that $R = R_e(1 + \epsilon)$, where ϵ is much smaller than one, Brennen [8] has been able to show that if the duration of pressure changes is much shorter than gas diffusion, the critical radius is given by:

$$R_c = \left(\frac{9\lambda m_g T_b C_g}{8\pi S} \right)^{\frac{1}{2}} \quad 2.10$$

Here λ is the polytropic constant, m_g is the mass of the gas, T_b is the temperature of the bubble and C_g is the gas constant. By assuming isothermal behaviour and for a given constant mass of the permanent gas present in the nuclei, Brennen [8] showed that the equilibrium radius will first increase as P_∞ decreases and when it reaches the critical radius and the critical surrounding liquid pressure, the smallest decrease in liquid pressure will cause an explosive unstable growth. This is important especially in turbulent flows where pressure fluctuations exist. If the fluctuations are large, then nuclei which were at equilibrium could reach the critical condition and start to grow. In a low pressure region, all nuclei with a radius larger than critical radius will grow and become cavitation bubbles and those smaller than the critical radius will not grow.

2.1.2 Cavitation Damage Causation

Plesset et al. [9] investigated the shape of a bubble at different stages of collapse using numerical techniques. This study assumed pure vapour bubble, incompressible and constant ambient and vapour pressure. The set of the equations are non-dimensionalised and the important parameters are the initial radius of the bubble, distance of the centre of the bubble to the solid wall and the ratio of the differential pressure between ambient pressure and vapour pressure to the water density ($\Delta P/\rho$). The investigations were performed using a differential pressure to water density ratio of 1 atmosphere to 1000 kilograms per liter for two cases. In the first case the bubble is initially touching the solid wall. In the second case the distance from the centre of the bubble to the solid wall is $1.5 R_0$. Figure 2-1 shows the changes in the bubble shape as it collapses for the first case.

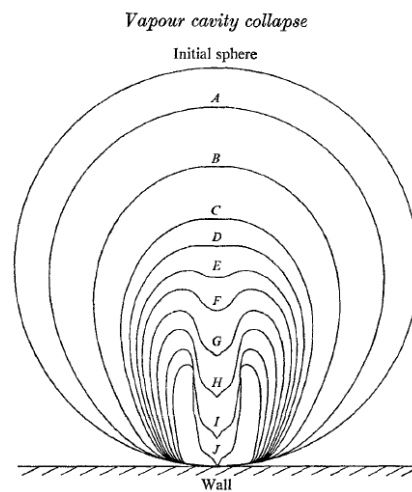


Figure 2-1 Numerical study of bubble collapse stages from an initial spherical bubble [9]

The results of these time stepped simulations showed that in the final stage of the collapse, velocities as high 130 m/s and 170 m/s could be reached in the first and second cases respectively. The water hammer effect of these jets for a bubble 1 mm in size can cause stresses as high as 2000 atm with a duration in the order of 10^{-7} seconds where the stagnation pressure in the first case is as high as 800 atmospheres and a duration in the order of 10^{-6} seconds which is most likely the damaging mechanism.

This numerical study subsequently was validated by the experimental investigation performed by Lauterborn et al. [10]. In this experiment two ruby laser beams were used and converged to create a bubble and the collapse of the bubble was observed.

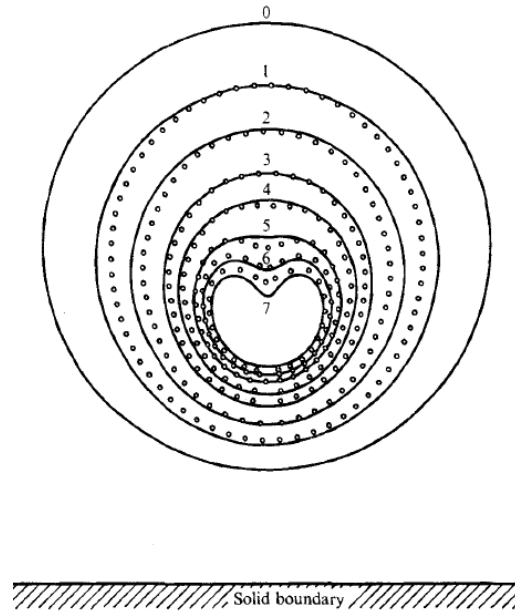


Figure 2-2 Comparison of numerical and experimental bubble shape in different stages of bubble collapse, solid lines represent numerical predictions and open circles represent the experimental data [10]

The results of this study have shown velocities as high as 120 m/s. Previously Plesset et al. [9] had shown velocities as high as 170 m/s. It is unclear whether velocities as high as 170 m/s were available and were not detected due to the state of the technology at the time or such high velocities were not present at all. Given the imaging rate of 300,000 frames per second, technically it was possible to measure velocities even higher than 170 m/s but this study does not give any reasons why the numerical study and the experimental study did not agree when it comes to maximum velocity reached near the boundary.

In the next part, cavitation in turbulent flows will be discussed and the flow structures which cause extreme pressure drops will be introduced in different studies.

2.1.3 Cavitation Noise

It has been well established that cavitation causes acoustic noise and vibration. The basic investigations in cavitation noise are provided here. To be able to study cavitation noise, it is important to quantify collapse duration. Assuming a spherical bubble throughout all stages of bubble collapse and using the Rayleigh Plesset equation (2.2), the total time for collapse of a bubble was theoretically found to be [4]:

$$\tau_c = 0.915R_i\sqrt{\rho_l/(P_l - P_v)} \quad 2.11$$

where τ is the total duration of collapse, R_i is the maximum initial bubble radius, ρ_l is the density of the fluid, P_l is the pressure of the surrounding liquid and P_v is the vapour pressure.

Radiated noise from bubble collapse was first thoroughly investigated by Fitzpatrick et al. [11]. Their analysis shows that the high compressible volume changes of the vapour at the late stages of bubble collapse.

Figure 2-3 shows the ideal spectrum of radiated sound from a cavitation bubble. The variable on the x axis can be approximated as frequency times collapse time as explained by Blake [12]. This is helpful in identifying the dominant frequency ranges of acoustic noise generated due to bubble collapse.

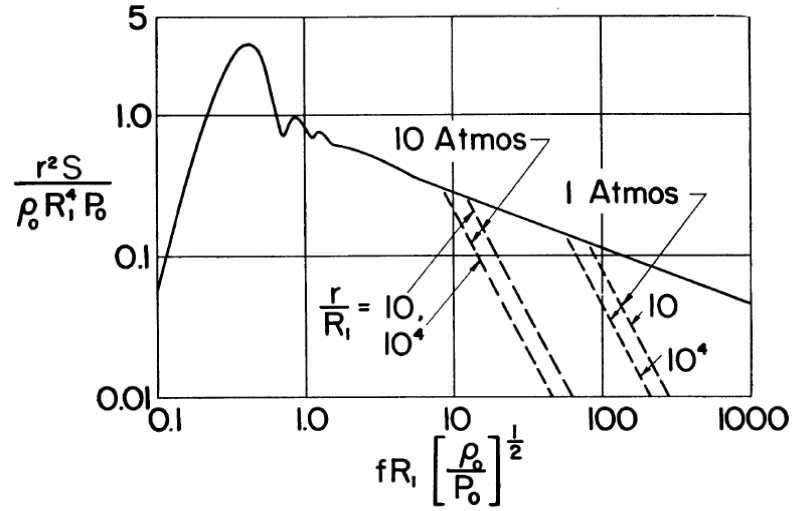


Figure 2-3 Radiated sound spectrum of a cavitation bubble [11]. The dashed lines indicate the asymptotic cut off frequency for a given condition as investigated by Fitzpatrick et al. [11]

Considering a cavitation bubble of radius size 0.5 mm in water to collapse in a liquid at 100 kPa, the time constant for this bubble is approximately 4.6×10^{-5} . To obtain the highest pressure levels of bubble collapse and achieve a sound pressure level greater than 1, value of the spectrum variable (x-axis on figure 2-3) should approximately be 0.2 to 0.6. Then the frequency range of bubble collapse for the example cavitation bubble is [12]:

$$f_{High} = \frac{SPL}{\tau_c} = \frac{0.6}{4.6 \times 10^{-5}} = 13,000 \text{ Hz}$$

$$f_{Low} = \frac{SPL}{\tau_c} = \frac{0.2}{1 \times 10^{-4}} = 4300 \text{ Hz}$$

The radius of the bubble chosen in this argument is the maximum size of the nuclei typically found in the municipal water lines. Since this is the maximum radius it results in the lowest frequency ranges and as the radius of the bubble decreases, time constant

decreases consequently and therefore frequency has to increase to keep the spectrum variable constant between 0.3 and 0.5. This explains why smaller bubbles emit sound at higher frequencies compared to larger ones. At cavitation inception the size of the bubbles are small and emit high frequency noise and the lower the negative pressure becomes, the larger the bubbles and the lower the frequencies.

Some experimental studies were also performed on cavitation noise and the frequency range of the audible noise generated. Martin [13] performed studies on spool valves using microphones. The frequency spectrum is shown in figure 2-4 which shows the effective range of cavitation noise is from 5 kHz and up. They have also shown as cavitation number decreases, the minimum frequency increases which is in agreement with the theoretical approach of Fitzpatrick et al. [11] as a decrease in cavitation number means larger bubbles and therefore a reduction in the noise frequency.

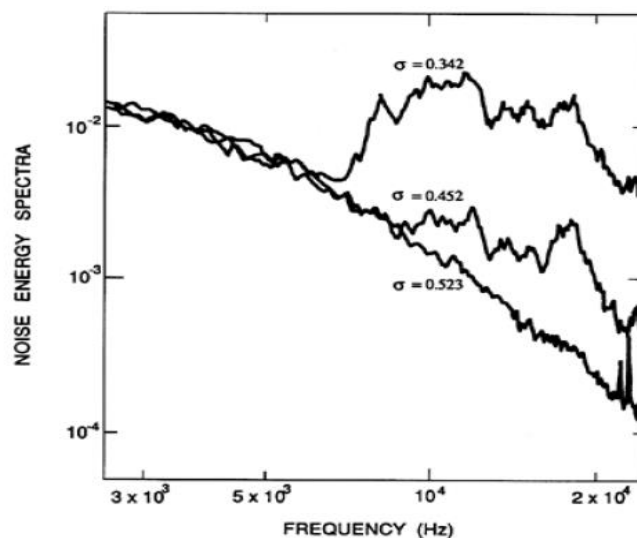


Figure 2-4 Frequency spectrum of the noise generated in a cavitating spool valve at different cavitation numbers as observed by [13]. The graph was reproduced by [8] in higher quality.

Another study was performed by Ceccio et al. [14] on cavitation in external flows past Schiebe headforms (an axisymmetric oval shaped body). This study utilised visual and acoustic methods to study cavitation. To perform the acoustic study the acoustic impulses were averaged and using discrete Fourier transform the frequency spectrum was obtained. Figure 2-5 shows the frequency spectrum against an arbitrarily normalised value as the amplitude of fluctuations. The noise generated by these bubbles was broadband and it was in the region of 0.3 to 10 kHz. After this frequency a decline in the amplitude is observed. The sharp drop at 80 kHz is due to the limiting frequency of the hydrophone used.

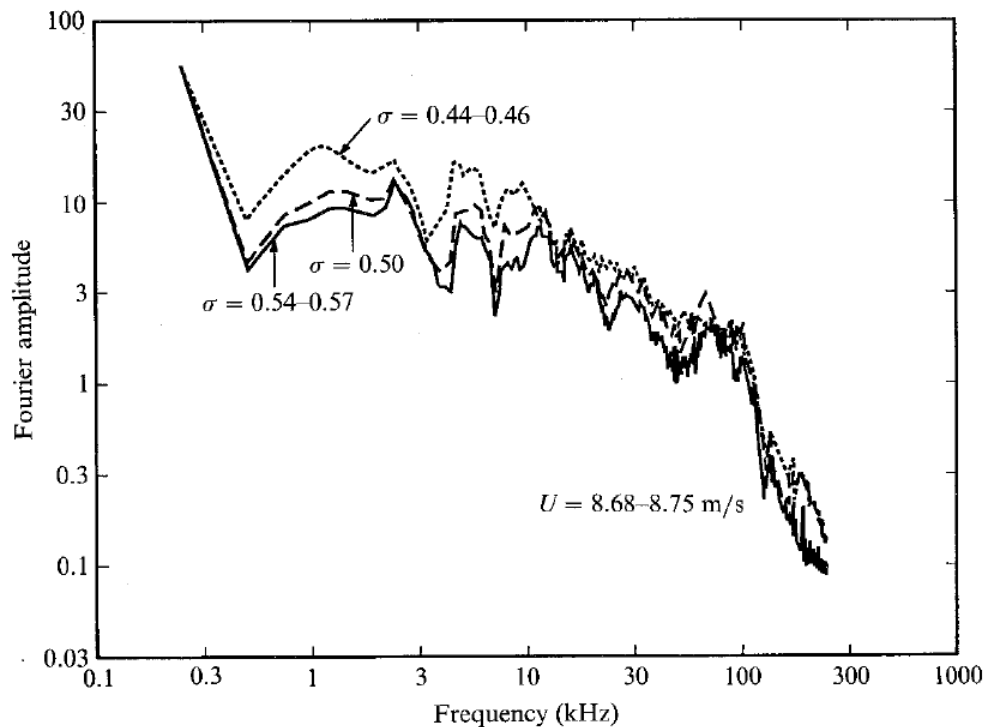


Figure 2-5 Average frequency spectrum of cavitation acoustic noise generated for different cavitation numbers [14]

The reason behind the existence of such low frequencies here is due to existence of large bubbles. The maximum size of the bubbles in this study was as high as 5mm. This study

also agrees with the theoretical development of Fitzpatrick et al. [11], however an exact correlation is not provided. It is expected that if the exact size of the bubble was studied some deviations from the theoretical formulation would be observed due to existence of permanent gases and changes in the shape of the bubble at the final stages of the collapse.

2.1.4 Cavitation Effects on Hydrodynamic Performance

An important issue with multiphase flows is the increase in drag and the pressure drop associated with it. A cavitating flow is a form of liquid vapour flow and the pressure drop characteristics of it are different to that of a non-cavitating single phase flow. Thorneycroft [1] who was designing the fastest battle vessel at the time did not reach their predicted performance. In another study, effects of cavitation were studied on hydrofoils and it was shown that appreciable performance drop was observed in the operation of the hydrofoils tested [15]. However this drop in performance was not observed at initial stages of cavitation inception while cavitation became more dominant, this reduced performance was observed. Therefore understanding the physics behind this drop in performance is important.

As cavitation onset occurs, the fluid flow is no longer a single phase flow. As bubbles start to grow and increase in number, the flow becomes a two phase flow and the appropriate two phase Navier-Stokes enclosure equations must be used. At cavitation inception, bubbles are created and they collapse and therefore they do not appreciably affect the flow field. However, when cavitation becomes more developed and the bubbles start to collapse further downstream, the associated pressure drop can be formulated using

correlations for bubbly flows. As pressure drop increases even further, bubble clouds are formed which then then break up into smaller bubbles and collapse. In the last case, the characteristics of the flow are very close to that of a slug flow.

The reason behind this increased pressure drop is the increased shear stress within the fluid at the fluid bubble interface. As the size or number of the bubbles increases in a given cross section, the drag force increases which cause an increased pressure drop. If these bubbles are to exist in the flow for longer, cavitation clouds are formed prior which creates slug flow and causes increased pressure drop [16].

2.2. Cavitation Quantification

So far the concept of bubble formation, nucleation and bubble collapse has been covered. These studies were only interested in the mechanics involved with one single bubble. However in many engineering applications, this process is continuous and is caused by the pressure drop in the flow.

To investigate cavitation in a flowing liquid, a set of parameters must be introduced to be able to characterise the phenomenon. The common practice in fluids engineering is the definition of dimensionless numbers. Since many factors, such as viscosity, contaminants and etc. affect cavitation, it is the common practice in fluids engineering to define a simple cavitation parameter and show deviations from this dimensionless parameter due to different effects [17]. The easiest method is to approach cavitation using dynamic scaling.

The flow of fluids over or through a solid body can be described using streamlines. A non-dimensional parameter, commonly known as pressure coefficient, is used to describe the pressure drop in a streamline which is:

$$C_p = \frac{P_1 - P_2}{0.5 \rho u^2} = \frac{\Delta P}{0.5 \rho u^2} \quad 2.12$$

where P_1 is the first reference pressure and P_2 is the second reference pressure. If a flow is assumed to cavitate as P_2 reaches vapour pressure at a given temperature, then there exists a streamline with pressure coefficient of:

$$\sigma_i = \frac{P_1 - P_v}{0.5 \rho u^2} \quad 2.13$$

Equation 2.13 is referred to as cavitation number. A cavitation number exists for any given flow as long as the velocity, density and mean pressure (P_1) are known in the flow. However by decreasing the pressure or increasing the velocity, the cavitation number can be changed until incipient cavitation is observed. Figure 2-6 shows two identical systems, operating under identical conditions but different pressures. In this figure, it is observed that condition 2, which has a lower pressure, cavitates where condition 1 does not. Since the two systems are identical, the velocity and mean density are the same (assuming density of the fluid does not change significantly with pressure). However, the upstream pressures (P_1) are different in the two systems, resulting in lower cavitation number in condition 2. This shows that a cavitation number can be calculated for any flow.

However, only when cavitation number reduces to an incipient cavitation number, onset of cavitation is expected.

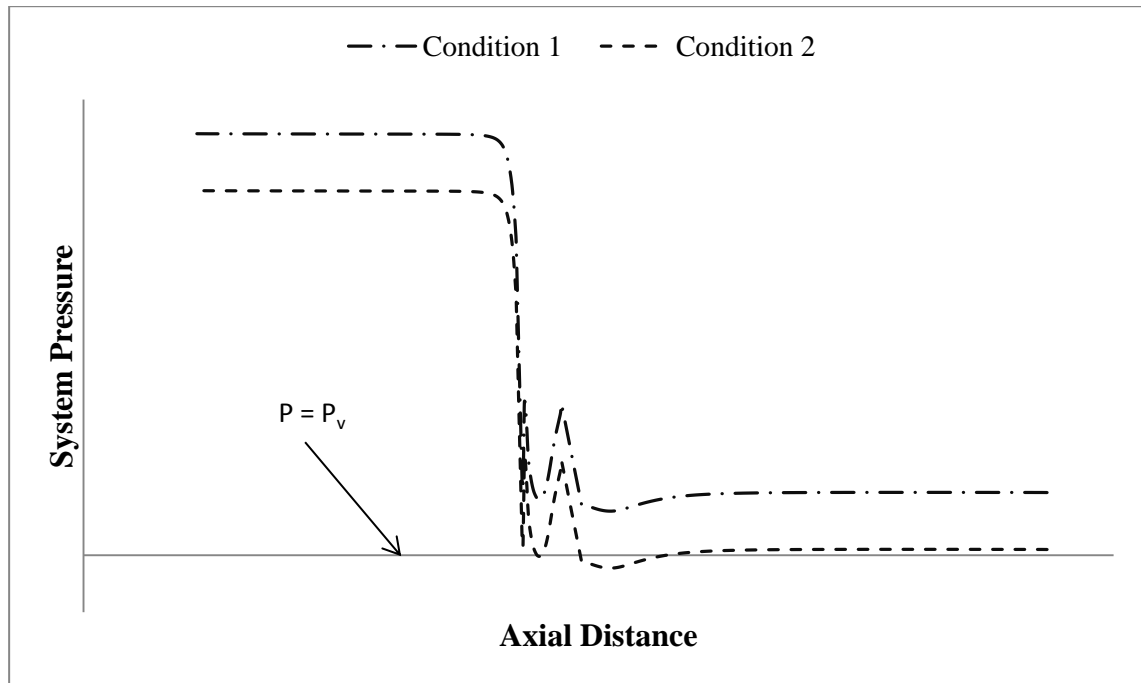


Figure 2-6 System Pressure operating under different ambient pressures with the same velocity

Using equation 2.13 in internal flow applications is not a good practice as the ratio of head produced is much larger than the dynamic head. An example of it would be the investigation of cavitation in pumps and another definition for cavitation number is required. If a set of non-dimensional parameters are obtained for a pump, one of them will be of the form:

$$\sigma = \frac{H_{SH}}{H} \quad 2.14$$

where H is the head produced by the pump and variable H_{SH} is the suction head which is defined as:

$$H_{SH} = \frac{P_{amb}}{\gamma} + \frac{P}{\gamma} + \frac{u^2}{2g} - \frac{P_v}{\gamma} \quad 2.15$$

Where P is the pressure supplied, P_{amb} is the ambient pressure and γ is the specific weight.

However dynamic head is usually very small in pumps compared to the dynamic head and therefore equations 2.14 and 2.15 reduce to:

$$\sigma = \frac{P_{amb} + P - P_v}{P_1 - P_2} = \frac{P_{abs} - P_v}{\Delta P} \quad 2.16$$

Here P_{abs} is the upstream pressure. This work was first performed by Thoma [18] on turbines. Equation 2.16 can also be used with other internal flow devices such as valves and it has been the non-dimensional parameter widely accepted for study of pumps, turbines and valves where equation 2.13 has been used for hydrofoils and submerged geometries. In the present work, equation 2.16 is used as cavitation number. Here a literature review of cavitation inception parameter with different flow structures and conditions is provided.

2.3. Cavitation in Fluids

The effects of cavitation in external turbulent flows and the factors affecting the onset of cavitation are provided here. This part of the literature review focuses on fundamental studies performed on factors which affect cavitation inception.

Katz [19] has performed studies on axisymmetric hemispherical geometries with a 2 inch cylindrical smooth body attached to the flat face of the hemisphere as shown in figure 2-7. The effect of the laminar separation, turbulent shear layer and turbulent reattachment on inception of cavitation was investigated by cutting the cylindrical body by 1 mm to create a step prior to the hemisphere. This resulted in a change to the height of the laminar separation and the results were contrasted against two blunt cylinders which have the highest possible separation region with 2 inch and 0.5 inch diameters.

The results of this study show that for blunt bodies cavitation occurs in the turbulent reattachment region where for hemispherical bodies it is within the turbulent region of the flow separation. The interesting finding in this investigation was that bubbles were formed within the fluid regions and away from the solid boundaries. The importance of this study comes to light when one notices that coherent structures are the main regions of bubble formation rather than the bulk turbulent flow. The author has used visualisation techniques and has also taken account of dissolved gas concentration in the water which was 10 parts per million with initial radius of 10 to 25 μm . To visualise the flow salt water has been used, which could introduce possible nucleation seeds by adding salt into the water.

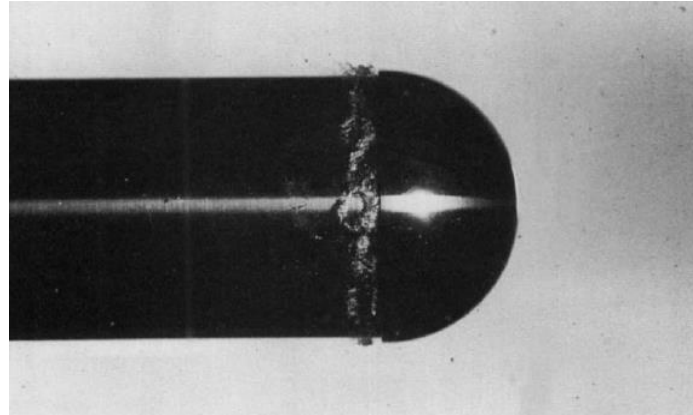


Figure 2-7 the hemispherical body with a step, $Re = 3.6 \times 10^5$ [19]. Note the 1 mm step after the hemisphere.

Ooi [20] studied the effects of jet size, jet velocity and nucleation site population with respect to dissolved air bubbles in submerged water jets. This study shows that at least for jet diameters smaller than 10 mm, Reynolds number has a negligible effect on cavitation inception in submerged jets for a given air bubble population. This study also showed how the pressure fluctuations affect cavitation occurrence. The argument of this study was that if the pressure fluctuates and the peak value is the same as cavitation onset pressure, cavitation will not occur unless the duration of that peak was greater than the bubble response time. The scaling factor was defined in terms of initial bubble radius present in the water and the pressure fluctuations and a new incipient cavitation number was defined as:

$$\sigma_i = K_a - \Delta\sigma_i \quad 2.17$$

where

$$K_a = \frac{1}{\rho u^2} \left(2(\bar{P} - P_v) + \frac{8S}{3R} \right) \quad 2.18$$

and

$$\Delta\sigma_i = \frac{8S}{3R\rho u^2} \quad 2.19$$

Here \bar{P} is the mean pressure. If equation 2.17 is replaced with 2.18 and 2.19 then we will arrive at:

$$\sigma_i = \frac{2(\bar{P} - P_v)}{\rho u^2} \quad 2.20$$

Using cavitation number was successful here as cavitation inception was not a function of Reynolds number for jets of the sizes investigated here. It can be seen in this study that cavitation occurrence is dependent on the jet diameter or cross sectional area. Here the inception did not occur in the coherent large eddy structures and rather it occurred in the fine dissipative structures. This study introduced pressure fluctuations as an important factor in cavitation inception which has made a major contribution in understanding cavitation. The authors noted that using peak pressure fluctuations rather than mean squared values perhaps would have produced better results.

O'Hern [21] has performed experiments using sharp edged plates to investigate cavitation in their wakes at larger scales than performed previously. These investigations showed that cavitation inception occurs in the shear layer behind the plate and also revealed the existence of spanwise and streamwise vortices. The results of the experiments showed

that cavitation inception occurs in the streamwise vortices meaning the cores of these vortices had much lower pressures compared to the mean pressure of the flow. The interesting trend observed in this study is the dependency of cavitation inception and Reynolds number in the shear layer cavitation. Although pressure fluctuations are measured no trend is observed. O'Hern suggested that the air injection technique used for pressure fluctuation measurements was the reason for not obtaining a trend as these bubbles entered the recirculating regions, influencing pressure fluctuations in bulk. It is argued that pressure in the centre of the streamwise vortices is the cause of cavitation as the equation below suggests.

$$P_c = P_\infty - \rho \left(\frac{\Gamma_s}{2\pi r_c} \right) \quad 2.21$$

where Γ_s is the circulation and subscript c denotes core of the vortex. Equation above suggests that an increase in circulation will cause a drop in pressure for a vortex of known radius which was noted [21].

Ran et al. [22] performed experiments on 1 inch submerged jets which is an extension to the work performed by Ooi [20] only with a larger jet. Their experiments included acoustically excited flows and the results were compared against same flow conditions without acoustic excitation. The authors concluded that that the jet velocity affects the cavitation inception index and is a factor that should be considered when scaling cavitation but it is not a Reynolds number effect on the boundary layer. Their experiments were performed using constant jet velocity and cavitation number was changed by

changing the ambient pressure as the rig was pressurised. The investigations showed that as jet velocity increases, cavitation inception number decreases. A very interesting explanation was given in this study. As velocity increased, coherent structures broke down earlier into small scale turbulence which eliminated the pressure peaks in the core vortex which in turn decreased inception cavitation number. This study has also shown that acoustically excited jets have different flow structures compared to unexcited jets but yet the effects on cavitation inception is minimal. This study is not in agreement with that of Ooi [20] when it comes to the scaling factors as here velocity of the jet is an important factor where in the previous it was shown that inception is almost independent of nozzle Reynolds number. Ooi [20] used smaller jets, nearly an order of magnitude smaller. The comparison between the two studies shows that size of the nozzle has significant effects on factors which needs to be incorporated in the cavitation inception number. Again the importance of pressure fluctuations on cavitation inception are shown here which agrees with the study performed by Ooi [20].

Ran et al. [22] have also studied cavitation from a statistical point of view. They have shown that there exists a range of cavitation numbers where cavitation inception is a probability.

Figure 2-8 shows the probability of cavitation inception in the near field of the jet. The flow field was seeded with air bubbles (nucleation seeds) and the bubble population density was measured and the results were compared against cases where the distribution of these bubbles were controlled such that either the average number of bubbles per unit area was the same throughout the jet (“uniform bubble density”) or the number of the

bubbles are the same throughout the jet (“uniform bubble flux”) which means as jet progresses forward and expands the bubble population density decreases. As one can see, the occurrence of cavitation at inception is a probability for a range of cavitation numbers and uncontrolled nuclei distribution increases the probability of cavitation inception.

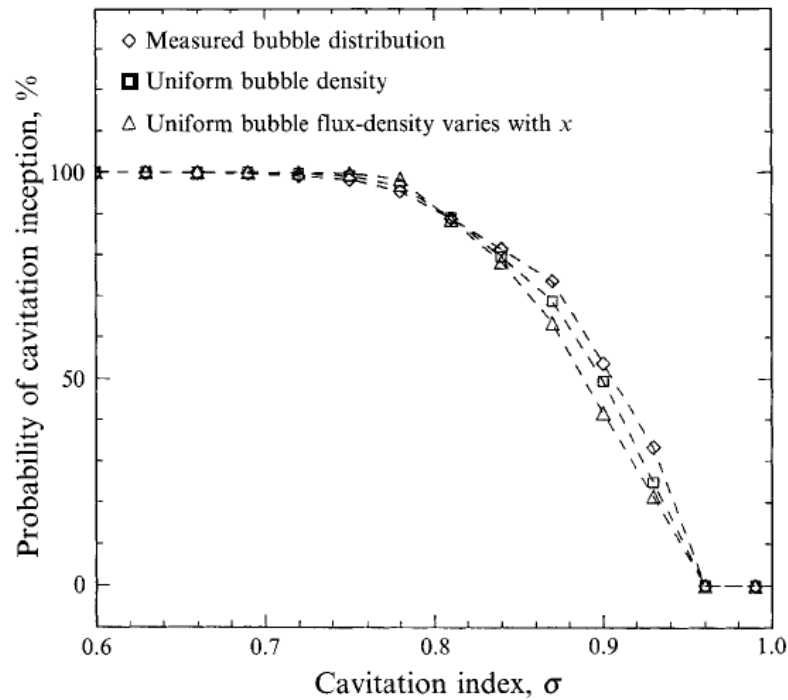


Figure 2-8 Cavitation inception probability within nearfield of the jet. Ran et al. [24]

Kuhn de Chizelle et al. [23] have performed a study on Schiebe head forms which are an axisymmetric body. Three different sizes from 5.08 cm to 50.8 cm were used to conduct experiments. In this study, a hydrophone was used as well as visual techniques for acoustic studies. The results show that cavitation inception occurs at higher cavitation numbers for larger diameters. This means that for the same cavitation number, the smaller body may be not cavitating where the larger body is undergoing cavitation for the same

velocity and given air content. The difference is due to the effects of the size on pressure drop and pressure variations in the same non-dimensional streamline distance; hence the larger cavitation inception number for larger bodies is justified. In this study the characteristics of the bubbles formed were also investigated using visual techniques and it was shown that the form of the bubbles deviated from a perfect spherical shape as the size of the bubble increased. This departure from sphericity is due to the smaller effects of surface tension in the larger bubbles and as the bubble becomes smaller, the effects of surface tension causes the bubble to hold on to its sphericity. An acoustic investigation was also performed which showed that for high void fractions in the cavitation regions where bubble-bubble interactions can no longer be neglected, the acoustic characteristics changes and the acoustic noise could reduce greatly. Plesset et al. [9] speculated that the high velocity jet causes noise and vibration. As void fraction increases, the potential of bubble cloud to collapse is less as it initially forms smaller bubbles and these bubbles of different sizes collapse at different stages causing less noise at one time. Ran et al. [22] reported similar observation of smaller cavitation inception numbers for higher velocities.

Belahadji et al. [24] have studied cavitation inception and development in rotational structures of a turbulent wake. They have also employed acoustic methods using dynamic pressure transducers as well as visual methods for their studies. In this study, the author notes the fact that cavitation bubbles affect the turbulent structure even at inception when bubbles are small. However, he makes the assumption that if it is only at the inception point, the alteration of turbulent structures are negligible meaning that it does not change the flow structures considerably and using solid particles for visualisation is not required.

This study clearly shows the effect of cavitation on the rotational structures and how fully developed cavitation alters these structures using Strouhal number recorded by the acoustic sensors. Here it was shown that cavitation inception has a dependency on $Re^{1/2}$ in this particular case as well as cavitation number.

Goplan et al. [25] have performed another study on submerged jets with 50.8 mm (2 inch) diameters. Particle Image Velocimetry (PIV) was employed as well as acoustic methods for cavitation detection. PIV was used for non cavitating flow as well as cavitating flow which provided verification to the assumption made by Belahadji et al. [24] who suggested that turbulent flow structures are not altered at the early stages of cavitation. The boundary layer was experimented with by tripping it and comparing the results with the untripped boundary layer. The results showed that for the untripped boundary layer cavitation occurred earlier in the near field at $x/D = 0.6$ where for the tripped boundary layer it occurred at $x/D = 2$. The results of the study show that in untripped boundary layer, cavitation occurs in the near field three dimensional structures where in the tripped boundary layer it happens in the primary vortical structures as the boundary layer becomes very similar to “Kelvin-Helmholtz vortex rings with weak secondary vortices”. A detailed study of the turbulence in the near field of the two cases was performed to investigate the reason. The turbulent stresses showed higher Reynolds stress magnitudes of $\overline{u'^2}$, $\overline{v'^2}$ and $-\overline{u'v'}$ for untripped boundary layer. The effects of turbulent structures in the core region and the boundary layer were shown to be a major contributing factor to cavitation inception. Again the importance of initial flow conditions and turbulent flow structures are shown here.

Lyer et al. [26] conducted an experimental study on cavitation of turbulent shear flows. The final results showed that cavitation in shear layers does not affect the mean pressure and velocity fields in the downstream. However, cavitation increases the streamwise fluctuations and decreases Reynolds stresses and cross-stream fluctuations. Another effect of cavitation is significant alteration of turbulent wakes, particularly the frequency of vortex shedding. Single phase numerical simulations were also performed and as the minimum pressure reached vapour pressure, cavitation inception was assumed to occur. However, the resolution of the mesh is very important to be able to capture turbulence features and local minimum pressures. They investigated unsteady phenomena using Large Eddy Simulations (LES). An interesting observation was that once a non cavitating vortex is stretched due to conservation of angular momentum, rotation will increase and as a result core pressure will decrease. However, in a cavitating vortex the core pressure can be constant and increasing rotation will only cause more vapour formation.

Many more studies were performed on the different aspects of interactions between cavitation and turbulent structures such as those performed recently by Aeschlimann et al. [27] who studied cavitating and non cavitating flows inside mixing layers and showed that compressible effects are not the cause of different physics but rather it is the existence of two phase flow which causes interactions between small scale and large scale eddies

The studies here show the effects of turbulent structures and pressure fluctuations on cavitation inception. The primary cause of cavitation onset in a flow is the pressure drop in the coherent structures such as vortices and wakes or boundary layer separation.

Inherent pressure fluctuations of the flow also play a role in earlier onset of cavitation. It seems that in the design of hydraulic systems, extensive studies must be performed on the turbulent structures and the local pressure drop associated to them.

2.4. Internal Flows and Non-visual Detection Techniques

Detection of cavitation using non-visual techniques has been the focus of industrial research as it is not possible to visualise the flow in hydraulic devices such as large pumps, turbines or valves. Techniques and instruments used for cavitation detection without flow visualisation and characterising cavitation in internal flows is the focus of this section.

One of the first cavitation detection studies on spool valves was performed by Martin et al. [13] where cavitation in spool valves was examined for 2 different sizes. A pioneering method for cavitation detection using accelerometers and dynamic pressure transducers was introduced. The authors have recognised the increase in the high frequency energy as a result of cavitation and have formulated the energy in pressure fluctuations as $\overline{p'^2}$ for a given frequency band. To detect cavitation, they have obtained the area under the curve for the pressure fluctuations by integrating numerically for a given frequency range using:

$$E = \int_{f_1}^{f_2} \overline{p'^2} df \quad 2.22$$

Here E is the energy, p' is the pressure fluctuations and f is the frequency. In a more general form equation 2.22 becomes:

$$E = \int_{f_1}^{f_2} PSD(f) df \quad 2.23$$

Here $PSD(f)$ is the power spectrum density of the signal acquired which has the square of the units, the time domain measurements were performed in. For example if the time domain signal is pressure with the unit of Pa, then $PSD(f)$ has the unit of Pa^2 which is the case in this study.

The energy was normalised against the noncavitating energy and when the value obtained for a given cavitation number was larger than 1, it was deemed to be at cavitation inception.

Detecting acoustic emissions is another method used for cavitation detection. Alfayez et al. [28] have performed studies on cavitation in pumps using acoustic emission methods for frequencies between 100 kHz and 1000 kHz to investigate the ultrasonic emissions of cavitation as the theory of Fitzpatrick et al. [11] suggests the existence of very high frequency contents. Their studies showed the method to be successful but they did not quantify the energy levels.

Cernetic [29] studied cavitation in kinetic pumps using vibrations and noise measurements. This study showed that examining frequency ranges less than 1000 Hz is not as useful as considering the content in frequency bands in the kHz range. When it comes to noise measurements, studying frequencies above 3 kHz was shown to be even more useful as an increase in the power spectrum in this range was observed. However,

since this increase was not quantified, exact cavitation inception could not be detected.

Again this is in agreement with the theory of Fitzpatrick et al. [11].

Takahashi et al. [30] performed investigations on perforated orifices and investigated installing butterfly valves upstream of an orifice at different distances. They have employed shock pressure measurements using a film pressure sensor for cavitation detection method and have also used accelerometers. The shock pressure detection method is based on the high shock waves generated after bubble collapse as investigated fundamentally using numerical techniques by Plesset [9]. Their experiments show that for smaller openings, cavitation occurs at higher cavitation numbers if the orifice is 1D after the valve and cavitation occurs at the same number if the orifice is at 3 diameters downstream or more. This shows the effect of downstream flow on cavitation. Installation of a butterfly valve has caused an earlier onset of cavitation. This study clearly shows how cavitation is prone to flow conditions upstream and downstream. The method employed for cavitation detection is new and they have shown that shock pressure increases as cavitation number decreases.

Sato et al. [31] have investigated cavitation phenomena in circular cylinders. The geometry is a sudden change from a larger pipe into smaller pipe. They have used accelerometers and flow visualisation techniques for this study. From their investigations, the energy of the accelerometers are at the highest maximum prior to fully developed cavitation. This is perhaps due to bubble collapse much closer to the accelerometers as fully developed cavitation will have bubble collapse at further distances from the location of bubble growth. This has been confirmed by the flow visualisation provided in the

study. Large eddy cavitating vortices (fully vapour vortex) were observed utilising flow visualisation. The important findings of the study here is the effect of boundary layer tripping which weakened the cavitation. This is in agreement with the study performed by Ran et al. [22] in external flows. Again, cavitation has been detected in the shear layers and viscous separation layers and not the vena contracta.

Liu et al. [32] conducted performance testing on two step throttling valves and compared them with single step. The geometry and design of these valves were very similar to that of an inverted globe valve. To detect cavitation, acoustic pressure transducers were used upstream and downstream of the valves and a statistical function was defined which was based on power spectrum and a given frequency. It was shown that as pressure drop increased, the value of this function decreased indicating inception of cavitation. The authors in this paper pointed out a frequency fluctuation in the low frequency bandwidth of the spectrum due to cavitation inception. Although this could be true, theoretical investigations mentioned in section 2.1.3 do not support such hypothesis. Perhaps these low frequency fluctuations were due to changes in velocity field as explained in the previous section and not the bubble collapse. This study was performed to show that a two stage throttling valve performs better than a single stage.

Fu et al. [33] have studied cavitation inception in spool valves with U and V shaped grooves. Acoustic methods were used for cavitation detection and increase in high frequency pressure level was monitored rather than energy level increase. The experimental technique described in the paper was very unclear as only a diagram with brief explanation was provided. It is not clear whether the acoustic sensors were

hydrophones or acoustic pressure transducers and whether they were in contact with the fluid or not. However, the study of cavitation inception showed no obvious trend for the relationship between opening and cavitation number. The cavitation inception against opening was approached more systematically and a visual study was performed on a Plexiglass model to show the increase in sound pressure level as cavitation increases. They have shown that as cavitation number decreases, the pressure level approaches a peak and a further decrease in cavitation number causes the sound pressure level to drop to choking conditions.

Fu et al. [34] have studied non circular groove valves with oil as the running fluid. They employed both visual and acoustic methods and have shown that for a given set of different valve configurations, the trends of acoustic noise is the same as reported by other authors. As cavitation onset occurs, an increase in sound pressure level is detected. As cavitation number is reduced, the sound pressure level reaches a maximum and any further decrease in cavitation number causes a drop in sound pressure level. They also showed that a major noise of cavitation in the high frequency spectrum is attributed to the vapour shedding. Although their study is in agreement with previous studies, the fact that they have used oil as working fluid without monitoring the air content makes the study questionable. As discussed by Martin et al. [13] oil can dissolve 10 % air by volume and this could have significant effect on the results.

Another study was performed on spool valves with non-circular openings by Zou et al. [35] and it was found that as the opening was made smaller the critical cavitation number decreased. The importance of flow structures and their effects on cavitation inception is

reported here. This study confirmed that when cavitation becomes fully developed, decreasing the cavitation number could decrease the sound pressure level further.

Another interesting study was performed by Osterman et al. [36] on cavitation in axial valves which has a shape of a plug stopping the flow. Low frequency fluctuations were contrasted against the gradients obtained by flow visualisation and good agreement was provided between the two obtained results. There is no mention whether the visualisation was performed with particles injected and the size and other properties. However the methods are successful and provide a good indication for cavitation inception. The authors concluded that the flow visualisation is more accurate which is a questionable argument as many investigators such as Brennen [8] and Martin et al. [13] have stated that acoustic noise can be detected before any bubbles can be seen. Again, not many data points were provided and the onset of cavitation was not fully investigated to obtain a trend for opening against incipient cavitation number.

A series of experiments were conducted on cavitation in an orifice to determine best cavitation sensor. Mizuyama et al. [37] have conducted experiments on detecting cavitation using two accelerometers placed upstream and downstream of an orifice. From their studies for cavitation numbers near inception, considering frequencies less than 30 kHz was more effective. These studies were performed on different pipe materials and it was shown that the frequency ranges are different as material changes. Here using accelerometers for cavitation detection meant measuring the response of the pipe to the bubble collapse and as the pipe material changes, the stiffness of the pipe also changes and the frequency response is different; hence the changes in the frequency range. The

output ratio between the two accelerometers were measured and used as cavitation detection criteria. It was shown that for cavitation onset, the output of the upstream was twice that of the downstream and for developed cavitation the downstream accelerometer had an output 10 times larger. This is indicative of location of cavitation. As bubble collapse moves towards one of the transducers, higher amplitudes of sound and vibration are detected. There is no mention of coherence although two sensors were used as a measurement criterion.

Later on in another study on the same experimental rig, Nagaya et al. [38] have attempted to use acoustic measurements to detect cavitation by using non-directional microphones on the piping surface. Although this method was capable of detecting cavitation, it was less effective compared to using an accelerometer in terms of signal strength. Using output signal ratio between two microphones was successful in detecting cavitation. Also a high pass filter was designed and implemented with a band pass of 8 kHz. Using this filter made the signal ratio greater as less background noise was available and cavitation had stronger signals in this range. In an attempt to improve the detection capability using acoustic techniques, Nagaya et al. [39] have extended their previous work and used directional microphones instead with an accelerometer for comparison. Their results show that for frequencies above 5 kHz coherence between directional microphones and accelerometer were higher than 0.9 and directional microphones were detecting pipe vibrations as pressure fluctuations. However the ratio of the signals from downstream and upstream microphones increased and cavitation could be identified. Although this technique eliminates the requirement to know the background noise and vibration, if

cavitation occurs in a region where the signal is approximately between the two transducers then the ratio of the outputs will be close to 1 and cavitation will not be detected. This means that the user must have a guess of where cavitation will occur in the system and adjust distance between the sensors accordingly.

This review suggests that the use of high frequency energy content is more likely to be successful in cavitation detection. This is also in agreement with the theoretical development of Fitzpatrick et al. [11]. Also in the design of the tests facility, one must pay attention to the location of the sensors. If the sensors are far away from the possible location of cavitation, then attenuation could damp the signal and prevent cavitation detection.

2.5. Ball Valve Characterisation

As previously stated pressure drop occurs in any piping system. In industrial processes different pressures are required at various stages of the process. This is achieved by introducing a valve to the piping network. Pressure drop introduced by valves are commonly referred to as minor losses and are formulated:

$$\Delta P = C_p \frac{\rho v^2}{2} \quad 2.24$$

Later on American National standard Institute (ANSI) has made modifications to this equation and has provided a flow coefficient which is:

$$C_v = Q \sqrt{\frac{\rho/\rho_0}{\Delta P}} \quad 2.25$$

For fully turbulent flows and a given geometry, the flow coefficient is constant. Also since flow coefficient is dependent on flow rate, it eliminates the need to calculate the exact value of velocity in the orifice as calculating the effective area for many geometries is not feasible.

Many investigators prior and after introduction of ANSI 75 standard used C_P for the valve investigations. All these studies show a constant flow coefficient for a given valve at a certain opening when the Reynolds number is greater than 10^4 . When cavitation occurs, flow coefficient is expected to increase and flow coefficient is expected to decrease (refer to appendix C 0for C_P and C_v relationship). However many studies show that the performance of a hydraulic device does not change drastically at cavitation inception and cavitation has to be more rigorous to have significant effects, [8, 13, 32, 35].

One of the comprehensive studies performed on ball valves was performed by Merati et al. [40] to determine Strouhal numbers achieved in ball valves with V sector ball valves. Flow visualisation methods were utilised as well as dynamic pressure measurements. The results showed the existence of large three dimensional vortices which were dominant in the flow after the ball valve. The appropriate length scale for Reynolds number was determined to be pipe diameter the relationship between maximum amplitude Strouhal

number and Reynolds number was found to be a fifth order polynomial. The maximum amplitude Strouhal number had a range between 0.5 and 3.5.

Chern et al. [41] studied performance of ball valves when different apex angles of V-ports were installed after the ball outlet for different opening. They have used visual methods for flow structure and cavitation detection. However the usage of glass particles for visualisation techniques introduces nucleation seeds and therefore cavitation might occur earlier due to these nucleation seeds.

Chern et al. [42] have performed a fundamental study on performance of ball valves. They have employed flow visualisation techniques to study vortices and cavitation in these valves. In this study like the previous one performed by the same group the existence of particles in the flow will affect onset of cavitation. Here a 38 mm (1.496 inch) diameter valve was investigated. It was determined that the length of the recirculation zone behind the valves body will affect the pressure drop as it is an energy dissipative phenomena. This is in agreement with the study performed by Merati et al. [40].

2.6. Numerical Investigations of Pressure Drop and Cavitation

The use of ball valves in the industrial applications such as petroleum, oil refinement and etc. requires valves with large diameters. Practically, it is not viable to test valves this large. However, the pressure drop and cavitation characteristics of these valves are very important to estimate the flow and pressure drop accurately to ensure highest possible

safety and accuracy. Although using valve scaling techniques are a good method for pressure drop performance estimation, using numerical simulations could be potentially more accurate if used correctly and therefore it has been given much attention especially in the recent years as the computational power has increased rapidly.

Davis et al. [43] performed computation fluid dynamics analysis on globe valves and compared the results with experiments. The simulations and experiments were run for three different 1 inch valves with different seat sizes. The CFD model was an axisymmetric model to reduce grid size and the turbulence model chosen was standard k- ϵ and the solver chosen was FLUENT. The results of this study shows good agreement between CFD model and the experimental data for openings smaller than 70% but for larger openings discrepancies existed in the results.

Kim et al. [44] have performed numerical study as well as Particle Image Velocitometry on butterfly valves. The turbulence model used was SST to ensure the separation region is captured and have used hex tetra prism meshing and the solver used was ANSYS CFX 10. The numerical and experimental results show similarity in the flow field but the loss coefficient (flow coefficient) shows some discrepancies in the order of 15%.

Ozdomar et al. [45] performed computational studies on three openings of a standard ball valve of 31.5 mm inlet diameter and have contrasted the results against experimental values of the same geometry. The turbulence model used was standard k- ϵ . The model used was a 2D model with a structured grid. Although the model used was a 2D model, the discrepancy between the experimental and the numerical was within 10%, which

given the differences between the model and the physical valve, is considered excellent results.

Moujaes et al. [46] have numerically studied the flow and discharge coefficient in a turbulent flow through a ball valve. Three openings were chosen and the simulations were run for five different Reynolds numbers for each opening using standard k- ϵ turbulence model. The results of this study show that numerically flow coefficient is Reynolds number dependent. These numerical simulations were contrasted against experimental data of Chern et al. [41] and the difference between the predicted values was associated with difference in the geometry. The geometrical differences aside, the range of Reynolds numbers used in this study was 10^5 to 10^6 where in the study performed by Chern et al. [41] the range of Reynolds numbers were in the order of 10^4 to 10^5 i.e. an order of magnitude smaller. Moujaes et al. [47] does not specify whether the grid was structured or unstructured and from the grid independence study performed it seems that the maximum grid size was 120,000 nodes. However, the trends of discharge coefficient with opening were similar to the study of Chern et al. [41] and this shows that k- ϵ turbulence model shows promise for flow coefficient predictions in valves.

Glenn et al. [48] performed an extensive computational fluid dynamics study on cavitation detection in three types of valves including ball valves using standard k- ϵ turbulence model. They have shown that when cavitation occurs in the separation zone or shear layer, simply calculating the local pressure is not a good criterion for cavitation detection and the criterion must be:

$$P_v = P_{cell} - \frac{1}{2}\rho_{cell}u_{cell}^2$$

However, since standard k- ϵ performs poorly in the adverse pressure gradients, separation zones near boundary layers, this criterion may not be justified and simply choosing another model will provide better results by assuming occurrence of cavitation in a cell when the pressure reaches the vapour pressure.

3. The Experimental Facility

The goal of this thesis is to develop an experimental method for valve characterisation. To achieve this, the test section must be capable of accommodating sensors for cavitation detection and must have pressure tapings to measure the flow coefficient. The procedure for flow coefficient determination is described by American National Standard Institute [49] for valve testing. The schematic of the facility is shown in figure 3-1.

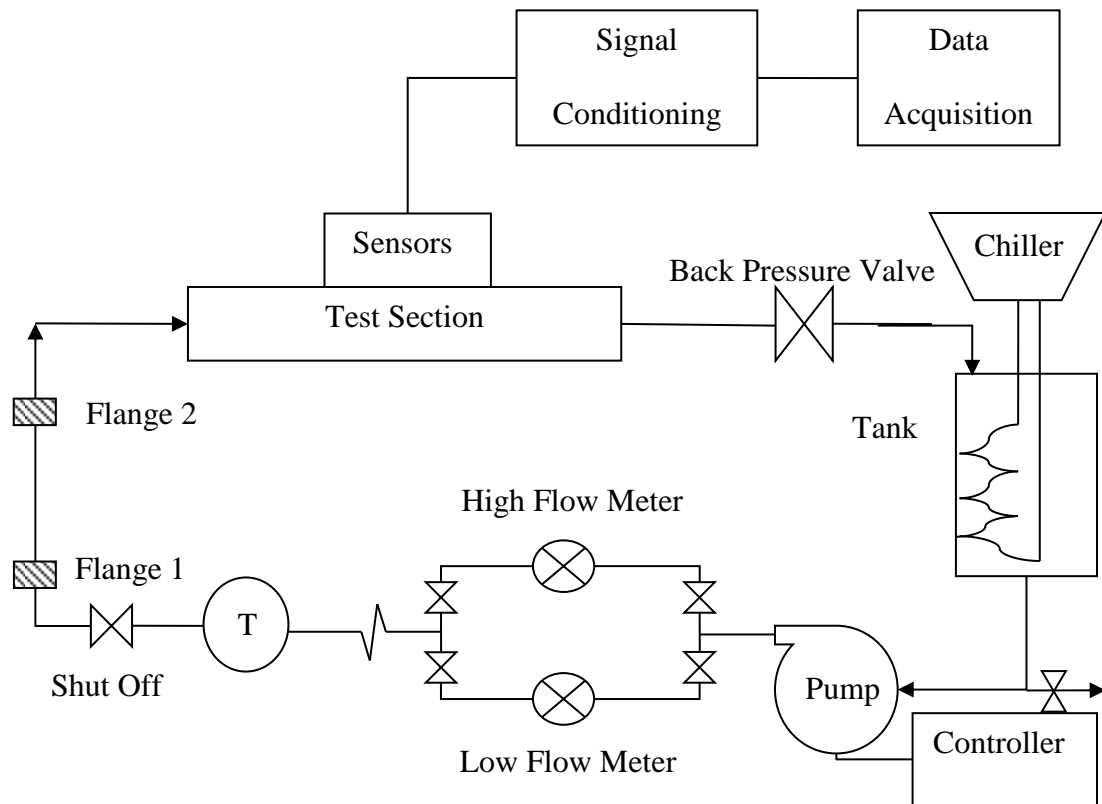


Figure 3-1 Schematic of the test facility

This facility consists of a 5 HP centrifugal pump manufactured by “Viking Pumps” which is controlled by a 10 HP Leeson microseries variable frequency drive. The water was

supplied from a tank into the pump and to control the temperature a Lytron 5.7KW chiller was used which was set to ensure a steady water temperature of 21.0 ± 0.2 °C.

A flow regulator globe valve was installed in the main line after the pump which is fully open position and the pipeline was divided to two branches. One branch was equipped with an Omega turbine flow meter with maximum flow rate at 0.76 l/s (12 gpm) where the other branch was equipped with another Omega FTB-1425 flow meter with maximum flow rate of 3.15 l/s (50 gpm) connected to a display with a pulse to analogue converter to allow accurate data acquisition. Starting with the higher flow meter, if the flow dropped below 0.32 l/s (5 gpm) the flow rate measurements were performed using the low flow rate branch by opening the low flow rate branch shut off valve and fully closing the high flow rate branch shut off valve. After the flow meter and at the end of the intake loop a T junction thermocouple was installed. A FLUKE 52II temperature reader was used to ensure the temperature is within the specified acceptable range.

The valves which are tested have internal diameter of 25.4 mm (1 inch), 38.1 mm (1.5 inch) and 50.8 mm (2 inch). Therefore the line had to be capable of changing size. Three different flange 2 connections were made with 1 inch, 1.5 inch and 2 inch hose barbs welded to them. A hose of appropriate size was used and connected the main line to the test section. The test section also had a hose barb at both ends to allow using clear hoses with maximum pressure of 250 psi to supply water at upstream and return the water to the tank at the downstream. The details of the test section, sensors, signal conditioning and data acquisition is described in details in the next section.

3.1. The Test Section

The valves which are tested have internal diameter of 25.4 mm (1 inch), 38.1 mm (1.5 inch) and 50.8 mm (2 inch). A separate test section was built for each internal diameter size. According to ANSI 75 specifications, two horizontally orientated pressure tappings were used at 2 internal diameters upstream and 6 internal diameters downstream of the valve were installed. This is to ensure that the flow has not undergone pressure drop due to velocity increase prior to inlet and distance downstream is the distance required to ensure the pressure in the flow has recovered from passing through the outlet opening. The pressure taps are 3.175 mm (1/8 inch) in diameter and have a length of 15.875 mm (5/8 inch). As this thesis focuses on industrial applications for cavitation detection, the same ports were used for cavitation detection positioned 6D upstream and downstream of the valve. The reason for using such ports for cavitation detection is due to the possible existence of such ports on site and easier installation at valve testing plants which eliminates the requirement for modifications to the existing test section. The elevation view of the test section is shown in figure 3-2.

The valves opening position was controlled using a pneumatic controller with a 60 psi air input. A 20 mA current input corresponds to 100% opening and a 4 mA input corresponds to 0% opening.

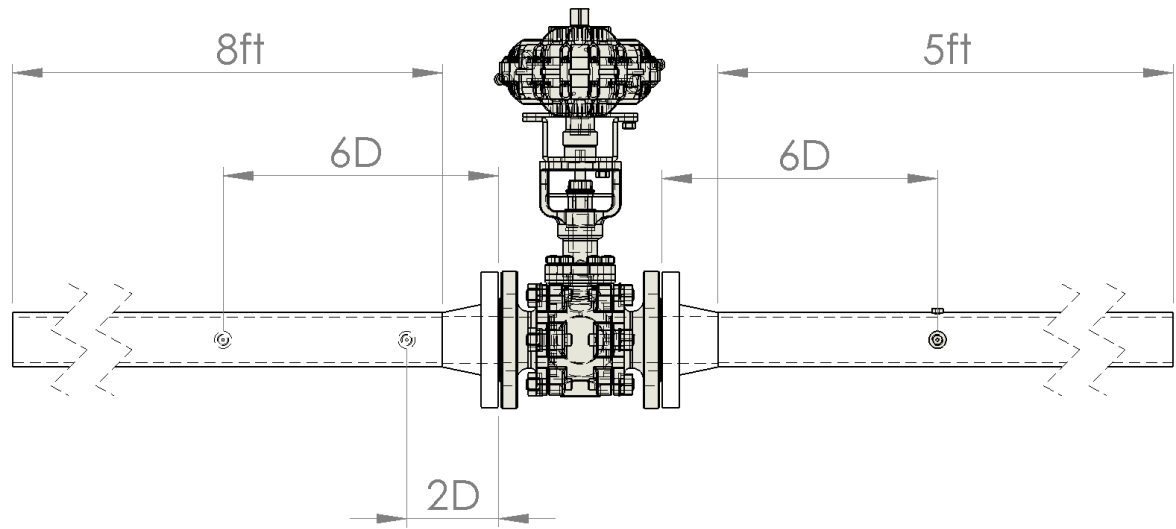


Figure 3-2 Front View of the Test Section

3.1.1 The Ports

To manufacture the ports, a 3.175 mm (1/8 inch) hole was drilled in the centre of a stainless steel rod. A 1/4 NPT coupling of 19.05 mm (3/4 inch) length was welded to these rods to allow for connection of pressure taps and dynamic pressure transducers. The length of the rods were such that when they were welded on the pipe and the pressure taps were drilled through the pipe, the total length of the 3.175 mm (1/8 inch) hole was 15.875 mm (5/8 inch). For instance, in the 25.4 mm (1 inch) pipe, the outer diameter of the pipe was 33.53 mm (1.32) inch which means a wall thickness of 0.406 mm (0.16) inch. In this case the height of the rod was 0.465 ± 0.005 inch and when the drilled rod was welded on the pipe and drilled through the wall of the pipe, the total length of the hole was 15.875 mm (5/8 inch). A drawing of the port assembly is shown in figure 3-3.

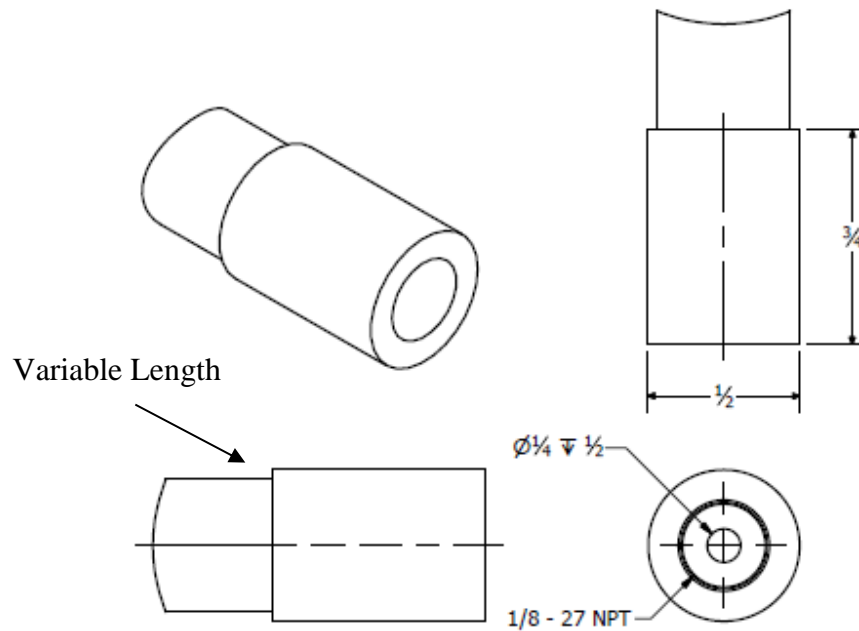


Figure 3-3 Assembly of the pressure transducer port

3.2. The Sensors & Signal Conditioning

The static pressure sensors were used for pressure drop and flow coefficient determination. The static pressure sensors used are Honeywell FP2000 series and the signal conditioner is a Honeywell SC3004 conditioning unit. Also a Valdyne DP-15 differential pressure transducer which was connected to a Valdyne CD-15 signal conditioner, is used which has a diaphragm capable of measuring pressures up to 80 psi to measure high pressure drops. The arrangement of the pressure monitoring system is shown in figure 3-4.

was provided with the flow meter indicating the error between the high flow meter and the display. The error between the pulses to analogue card was calibrated by inputting square wave pulses to the display using a signal generator. The reading on the display and the average value of the voltage obtained were plotted on a graph and the final maximum error was obtained. All calibration data can be found in appendix D.

For cavitation detection experiments, the dynamic pressure transducers used are Dytran V2005 and are installed at 6D upstream and 6D downstream of the valve. They were connected to a Dytran 4114B1 Current Source/Signal Conditioner unit and then they were connected to an NI 4431 USB DAQ. A Labview program was used to obtain the data and perform frequency spectrum analysis and coherence analysis instantaneously while data was being recorded. Also a PCB 352C33 accelerometer with maximum acceleration range of 25g was mounted on the surface of the pipe 6D downstream of the valve using adhesive mounting. The reason behind using temporary adhesive mounting was to mimic industrial processes better when creating a permanent mounting is not feasible. The centre of the accelerometer was in line with centreline axis of the downstream dynamic pressure transducer. The accelerometer was also powered using the signal conditioner as the dynamic pressure transducers and the data was obtained using the same Labview Virtual Instruments (VI) program. Two Desktop computers are used for data acquisition. The USB DAQ is installed on one and the PCI E6034 DAQ is installed on another computer to ensure smooth data acquisition process as this reduces the possibility of memory overflow.

3.3. Experimental Procedure:

To conduct the experiments, the following was performed:

1. The test valve controller was turned on and it is fully opened.
2. The pump was then turned on, the valve was opened fully and the controller was initially set to 2500 RPM for 5 minutes to flush all the air in the system out. This also ensures the flow fluctuations to reach a steady state.
3. The lines for the static pressure transducers are opened and the 2.5 psi pressure transducer was closed and the air was flushed.
4. The dynamic pressure transducers were untightened and left until water starts to drop from the ports. Then they were tightened.
5. The pump speed is set to 1000 RPM and if the Reynolds number achieved was beyond 10,000 then the next steps are performed. Otherwise the pump speed was increased in increments of 100 RPM until a flow rate corresponding to Reynolds number greater than 10,000 was achieved.
6. Once the system reached a steady temperature of 21.0 ± 0.2 °C, upstream pressure, downstream pressure, flow rate and temperature were recorded. Also data was acquired for the dynamic pressure transducers and the accelerometer for 150 s in intervals of 5 s and the obtained frequency spectrum was averaged between thirty 5 s samples.

7. If the system was operating without any indication of cavitation, the pump speed was increased by 500 RPM until cavitation occurred or the maximum pump speed was achieved.
8. If indications of cavitation were shown on the monitor, then the pump speed was reduced in 25 or 50 RPM increments until cavitation was no longer occurring.
9. Data were recorded by changing the RPM in increments of 50 RPM until cavitation became audible or maximum pump speed was reached.

The data acquired were analysed using a combination of Microsoft Excel and Matlab. The test procedure for background noise was the same as stated here except the RPM increase increments were 300.

3.4. Data Acquisition and Analysis Program:

To obtain and analyse the data from the static pressure transducers and the flow meter reader, an NI Labview program was designed. This program ran continuously and showed the results on the monitor. After changing the opening or changing the flow rate and a wait period of 20 seconds, the virtual save button was clicked and the results were saved in an “.lvm” file. The signals were sampled at a rate of 2 kHz for each channel. The number of samples recorded from each device is 90,000.

These raw data are then fed into a Matlab program which was already tested manually for accuracy and the flow coefficient (C_v), cavitation number (σ), pressure coefficient (C_p) and their corresponding errors were calculated for each test using equations below.

$$C_v = Q \sqrt{\frac{\rho/\rho_0}{\Delta P}} \quad 3.1$$

$$\sigma = \frac{P_{abs} - P_v}{\Delta P} \quad 3.2$$

$$C_P = \frac{2 \Delta P}{\rho v^2} \quad 3.3$$

Equation 3.2 was derived from equation 2.15. An order of magnitude analysis was performed to determine the significance of the dynamic head. It was found that this term usually is two or three orders of magnitude smaller than the pressure differential between upstream pressure and the vapour pressure and therefore it could be neglected. However, in very few cases, the dynamic head was only one order of magnitude smaller but since these cases occurred rarely, this term was neglected everywhere. The uncertainty was also obtained using the same program. The experimental uncertainty is explained in detail in appendix D. A summary of the error of each device and each parameter calculated can be found in tables Table 3-1 and 3-2.

Device	Measurement (Unit)	Max. Uncertainty
Honeywell 50 psi Pressure Gauge	Pressure (psi)	± 0.25 (psi)
Honeywell 25 psi Pressure Gauge	Pressure (psi)	± 0.13 (psi)
Honeywell 2.5 psi Pressure Gauge	Pressure (psi)	± 0.013 (psi)
Validyne DP-15 80 psi Differential Pressure	Pressure (psi)	± 0.40 (psi)
Omega FTB-1425 Flow Meter	Flow Rate (gpm)	1.0 % (of reading)
Omega DPF 700	Flow Rate (gpm)	2.2 % (of reading)
T-Type Thermocouple	Temperature ($^{\circ}\text{C}$)	± 0.5 $^{\circ}\text{C}$

Table 3-1 Uncertainty table of devices used conducting the experiments

Device	Measurement (Unit)	Nom. Uncertainty	Max. Uncertainty
Flow Coefficient	$\text{gpm}/\text{psi}^{1/2}$	$<5\%$	21.5 %
Cavitation Number	N/A	$<4\%$	16.1%
Pressure Coefficient	N/A	$<5\%$	20.8%

Table 3-2 Maximum uncertainty of tabulated parameters

The cavitation detection method was based on acoustic noise increase and therefore dynamic pressure transducers were used. Also an accelerometer was used to investigate the possibility of using single accelerometer for cavitation detection in situ in industrial installations. To analyse the data obtained from the dynamic pressure transducers and the accelerometer, another Labview program was designed using Labview VI to perform a discrete Fourier transform on signals of duration of 5 seconds. This operation was

performed 30 times and the average frequency spectrum of each sensor, the coherence function between the two dynamic pressure transducers and the coherence function between the accelerometer and the downstream pressure transducer were obtained. The sampling frequency was set to 90 kHz and the samples to be read were set to 450K samples. The USB DAQ has a digital filter which automatically sets the digital sampling rate much higher (128 times) than the analogue sampling rate specified. The output of the Discrete Fourier Transform (DFT) algorithm was set to power spectrum density in the NI Labview virtual instrument program. The window type chosen for this specific application is the Han window since this window has smaller stopband attenuation compared to Hamming window which allows peak detection in a Fourier transformed signal [50, 13]. This procedure provided power spectrum density in V^2/Hz for a frequency range of 0 to 45 kHz.

The cavitation detection technique was based on energy increase from reference energy levels. The energy levels were determined using equation 2.22 which is repeated below.

$$E = \int_{f_1}^{f_2} PSD(f) df \quad 3.4$$

The unit of the integral here is V^2 . Using the raw data from the sensors in volts eliminated the requirement for a voltage to pressure conversion and avoided any calibration error that could arise. The data was then input into a Matlab program which performed the energy integration for frequency bands of 2-5 kHz, 5-10 kHz and 10-45 kHz.

Also the coherence function, the ratio of cross-spectral density to auto spectral density of a signal at a specific frequency, is defined as:

$$Coh_{xy} = \frac{|G_{xy}|^2}{G_{xx}G_{yy}} \quad 3.5$$

The data was then analysed separately and the critical cavitation number was obtained for each opening and a plot of critical cavitation number versus opening was obtained for each valve. This is discussed in detail in the next chapter.

4. Results and Discussion

In this chapter, the experimental data is discussed and analysed. The motivation of this analysis was to provide flow coefficient and cavitation characteristics of ball valves. Also a discussion of pressure coefficient scaling and cavitation scaling is provided.

4.1. Pressure Drop Performance

The following section provides a summary of the analysis performed to characterise pressure drop of full port and standard port vari-V ball valves. Flow coefficient and scalability of pressure drop in valves is the focus of this study here and is discussed in detail.

4.1.1 Effects of Reynolds Number on Flow Coefficient

Figures 4-1 and 4-2 show the change of flow coefficient with Reynolds number. For Reynolds numbers greater than 2×10^4 , the flow and pressure coefficients did not change significantly and by considering the error bars, flow coefficient was constant for a given valve opening at a given size. In some cases for lower Reynolds number the upstream and downstream pressures were not high enough to be within the measurement accuracy of the static pressure transducers and therefore these results were not included in the analysis.

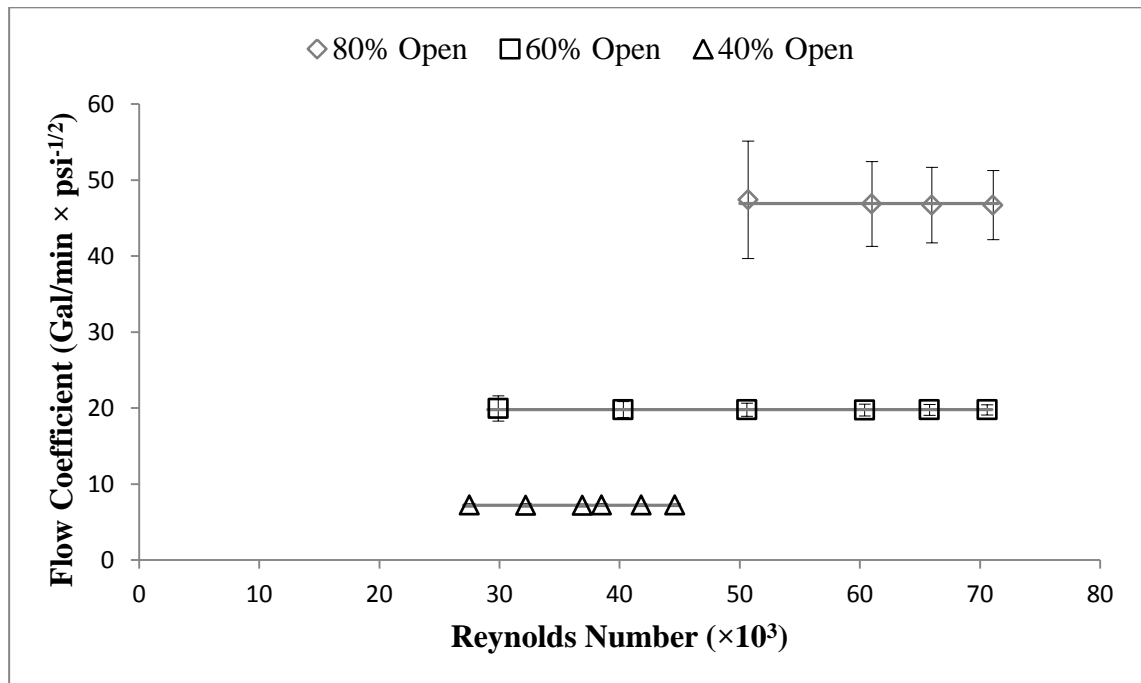


Figure 4-1 Variations of flow coefficient with Reynolds number for 2 inch 60V full port valve

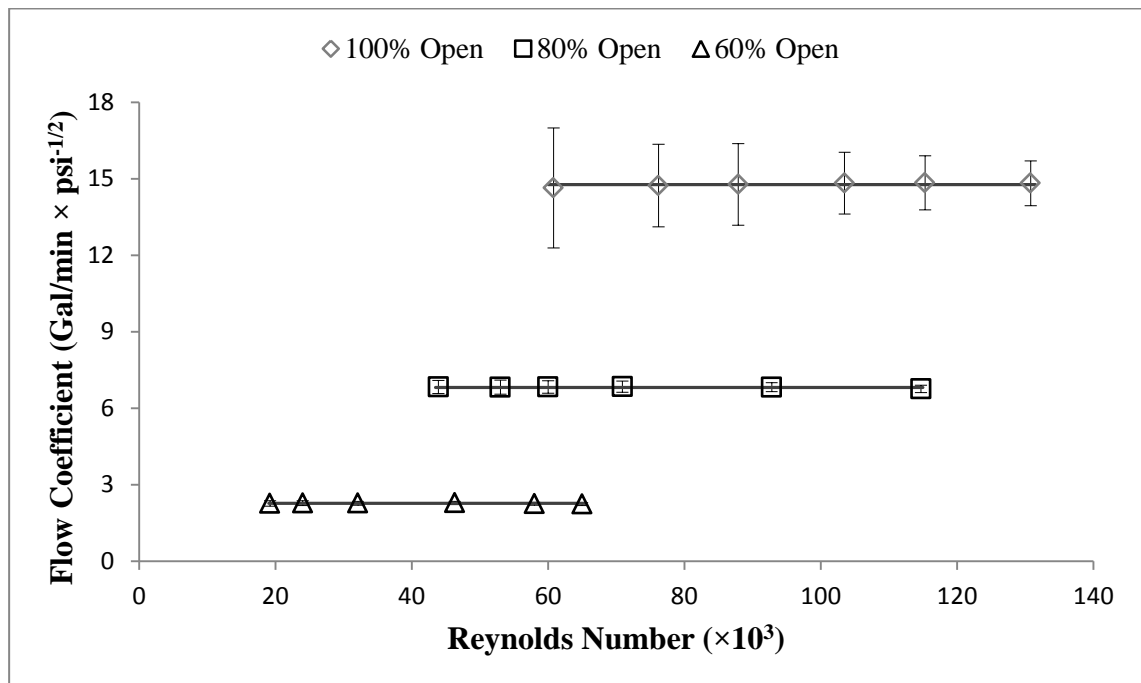


Figure 4-2 Variations of flow coefficient with Reynolds number for 1 inch 60V standard port valve

This trend was the same for almost all cases except 1 inch 30V standard port valve at 100% opening where the flow coefficient decreased with increasing Reynolds number for $Re > 83000$ due to cavitation. Figure 4-3 shows the flow coefficient for different Reynolds numbers for three different openings. It has been observed by other literature [8, 13, 15] that cavitation inception does not affect the performance at the initial stages of cavitation. This can also be seen from figure 4-3 where flow coefficient has not changed when cavitation inception occurs and it is intermittent. Cavitation becomes a problem when it is no longer intermittent and the cavitation regime is fully established.

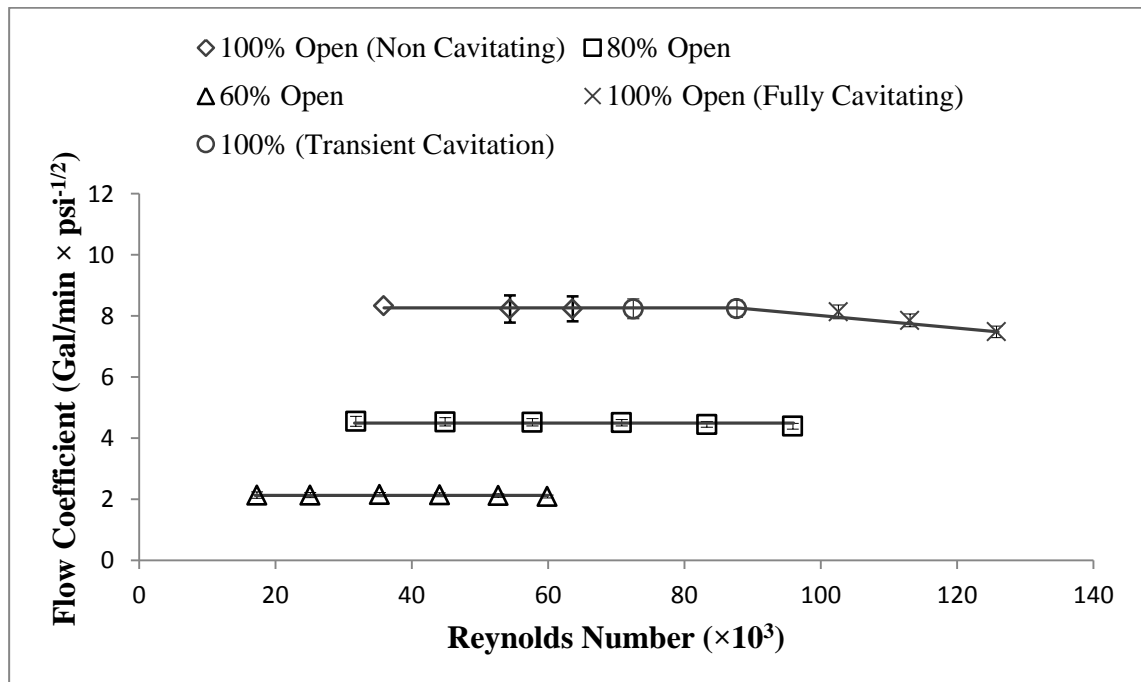


Figure 4-3 Variations of flow coefficient with Reynolds number for 1 inch 30V standard port valve at various openings

The cavitation regime will be discussed in the section 4.2 in detail. In the next part, the effects of valve opening on pressure drop and flow coefficient will be discussed.

4.1.2 Effects of Valve Opening on Pressure Drop Performance

By performing analysis on all valves, flow and pressure coefficients were obtained and compared for a given size of a given V-ball geometry. Figures 4-4 to 4-6 show the variations in flow coefficient with increasing apex angle for three different sizes of different openings. As the apex angle increases, the decrease in flow coefficient with respect to decreasing opening occurs at a higher rate. This allows the engineer to improve the performance of the plant by choosing the suitable ball valve. If fine control is required, a 10V ball valve is the suitable option and when a wide range of flow rates or pressure drops are to be achieved during operation, then larger apex angles should be used.

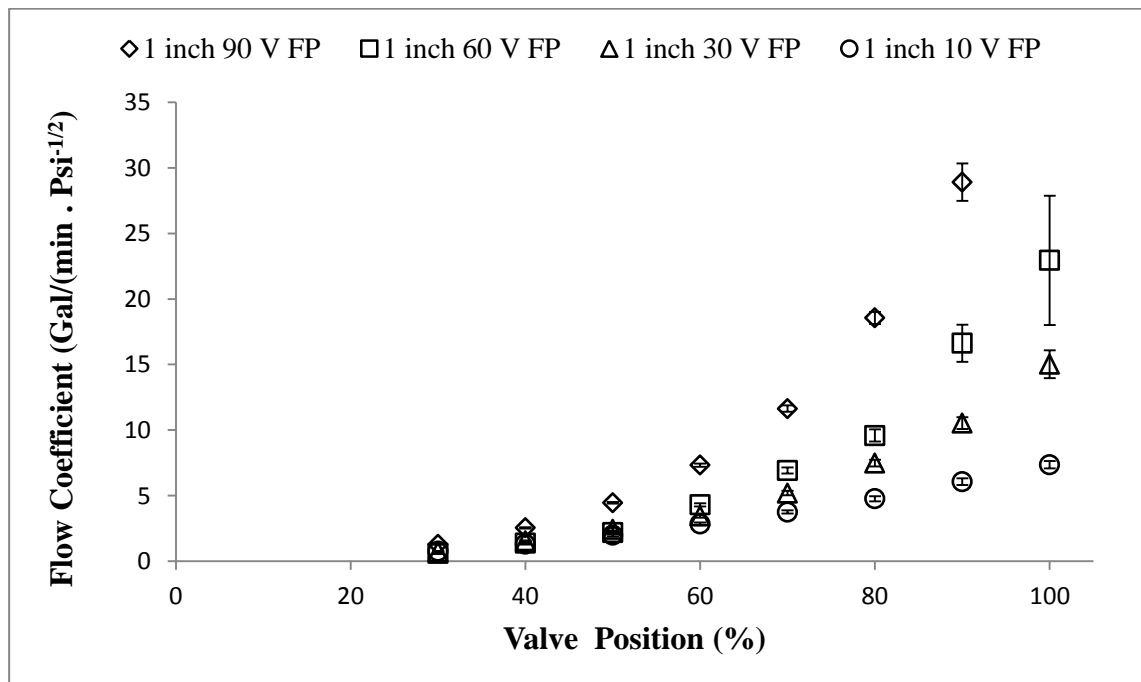


Figure 4-4 Variations of flow coefficient with opening for 1 inch full port valves with different inlet V apex angles

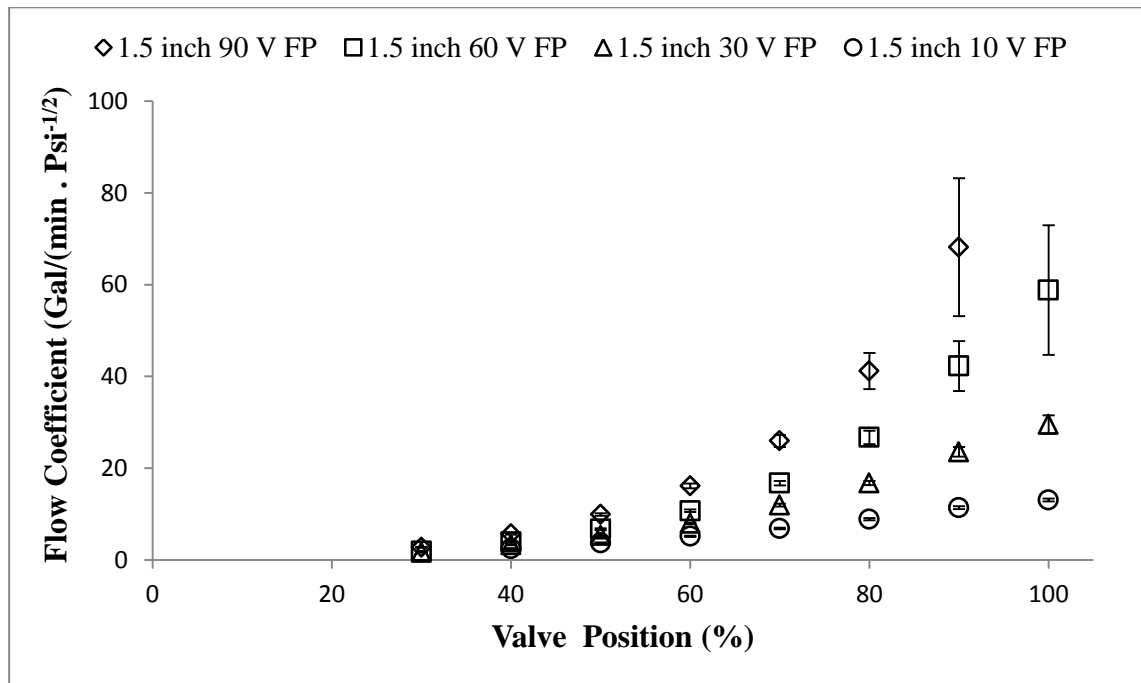


Figure 4-5 Variations of flow coefficient with opening for 1.5 inch full port valves with different inlet V apex angles

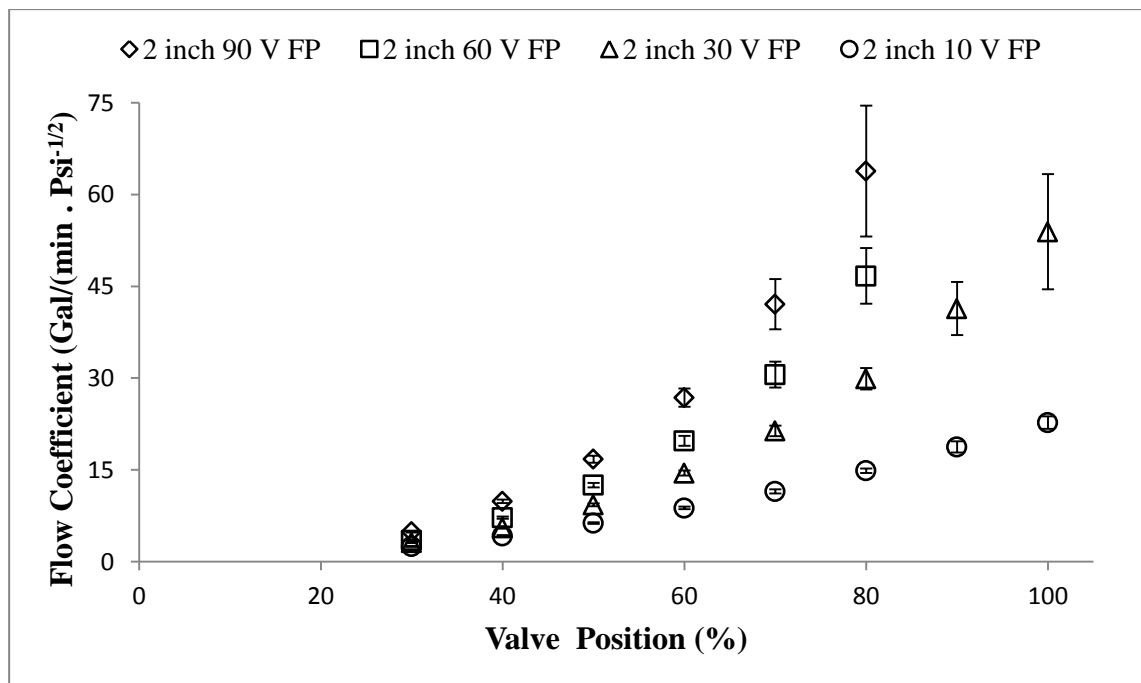


Figure 4-6 Variations of flow coefficient with opening for 2 inch full port valves with different inlet V apex angles

Figure 4-7 shows the trend for different ball valve geometries for a constant pressure drop of approximately 68.95 kPa (10 psi). From this figure, one can observe that as the angle of the apex decreases, a change in opening causes a smaller change in the flow rate achieved.

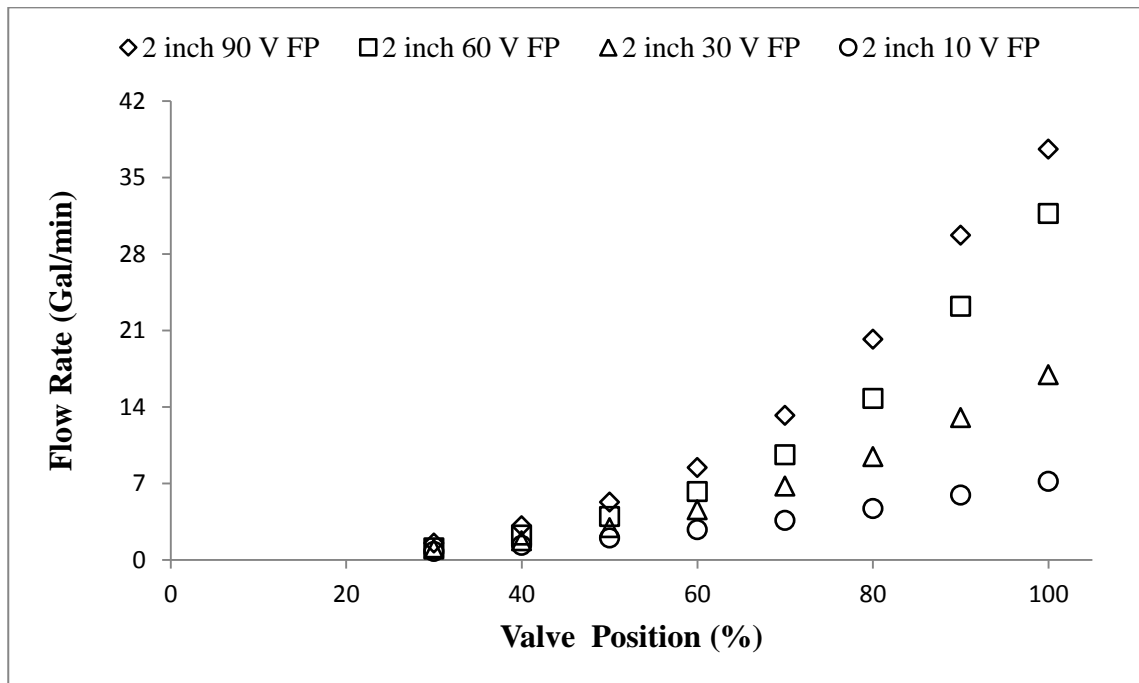


Figure 4-7 Variations of flow rate with change in valve opening for 2 inch full port valves with different V apex angles. (Arbitrary constant pressure drop, 10 psi)

The study of flow coefficient is not sufficient for valve scaling. From Buckingham PI theorem, a non-dimensional variable should be used for scaling. Pressure coefficient is the non-dimensional parameter widely used in scaling of pressure in hydraulic systems. Pressure coefficients of the valves are studied in detail next.

4.1.3 Pressure Coefficient and Scalability of Valves

The non-dimensional pressure coefficient is a more useful tool to compare the performance of the same valve geometry at different sizes. The pressure coefficients were obtained for all valves and were compared against other valves of the same geometry but different sizes. Figures 4-8 to 4-11 show the variations of pressure coefficient with opening for a given geometry at different sizes. As the change in the pressure coefficient span several decades, linear scale is not suitable and the results are thus presented on a semi log scale. The general trend is that for valve sizes larger than 1.5 inch, the pressure coefficient becomes nearly constant with an increase in size. Also as the apex angle increases, the pressure coefficients of 1 inch valves have values closer to that of 1.5 inch and 2 inch. For smaller apex angles, the pressure coefficient of 1 inch valves do not compare well with the larger sizes given they are plotted on a semi log plot. As the apex angle becomes larger, the 1 inch pressure coefficients become closer to that of 1.5 inch and 2 inch. The effect of apex angle on scalability in 1 inch valves suggests that cross sectional area plays a role in scalability. However the underlying reason for such behaviour is unknown at this time.

To ensure that the correlations developed are as accurate as possible, the results of 1 inch pressure coefficients are not included. Since the objective here is to estimate pressure drop in valves larger than 2 inch, this is justified. Using the pressure coefficients obtained, a correlation was developed by fitting a power law curve to the data of 1.5 inch and 2 inch valves for each apex angle as shown in Figure 4-8 figures 4-8 to 4-11.

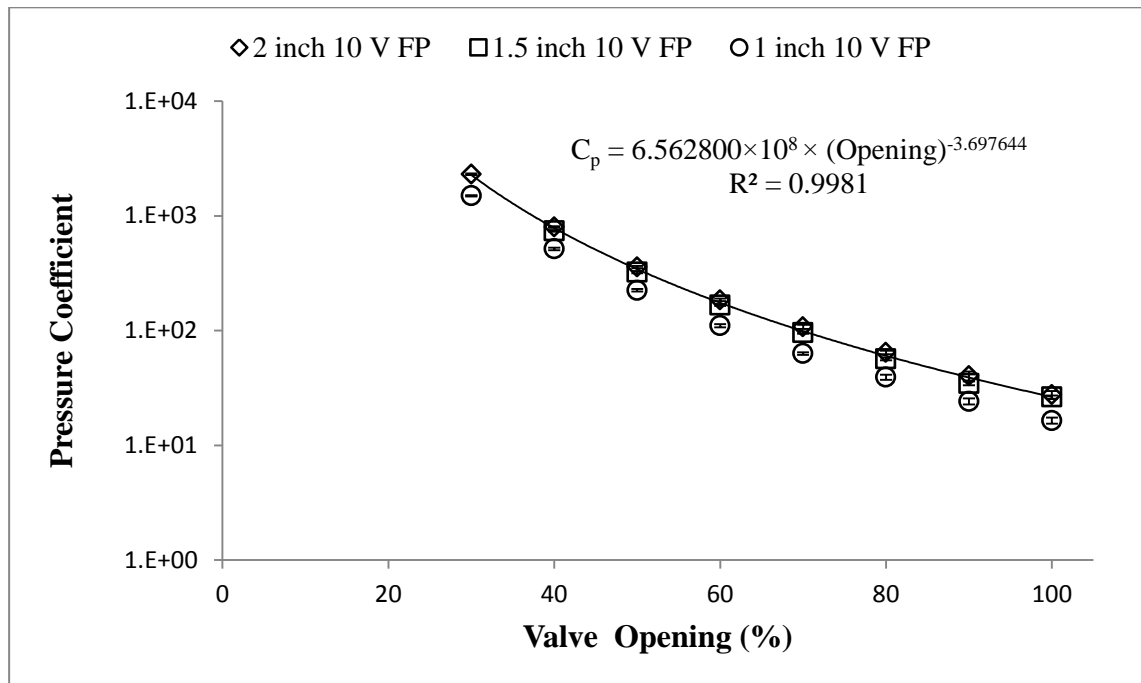


Figure 4-8 Pressure coefficient vs. valve opening for different sizes of 10V full port valves

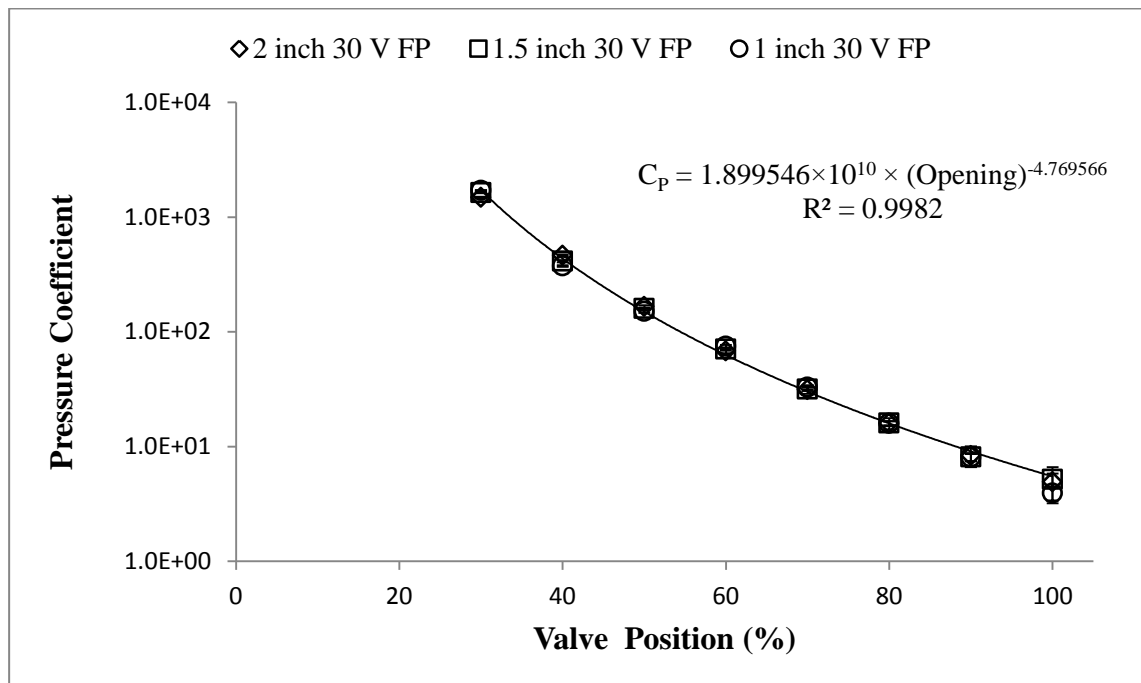


Figure 4-9 Pressure coefficient vs. valve opening for different sizes of 30V full port valves

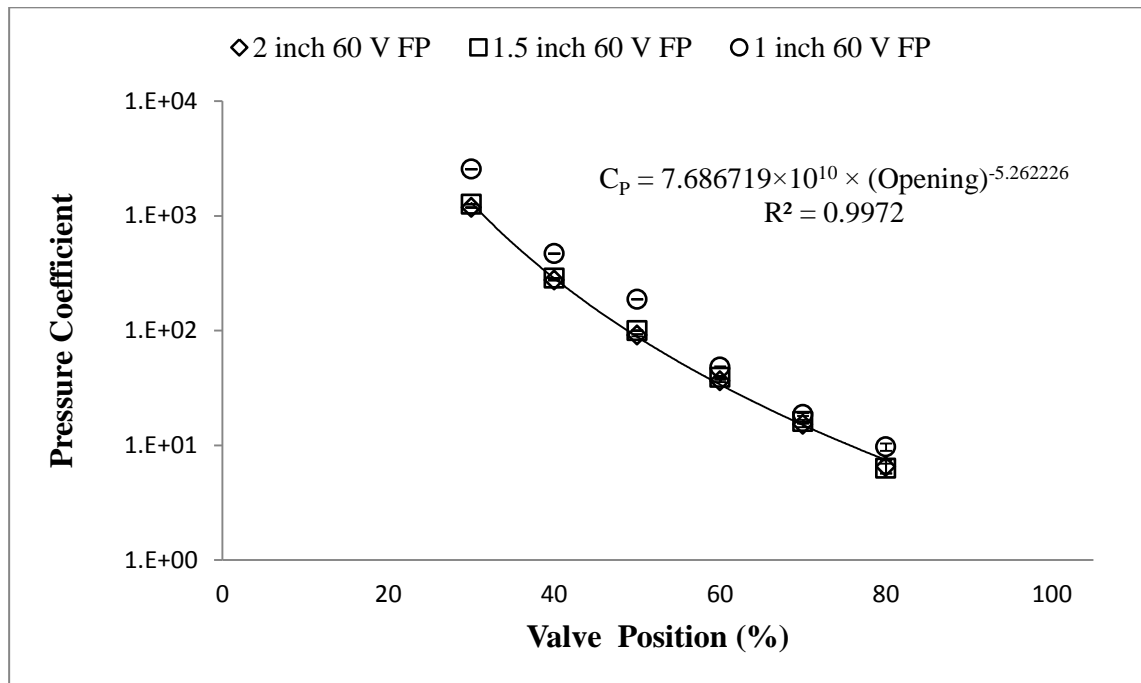


Figure 4-10 Pressure coefficient vs. valve opening for different sizes of 60V full port valves

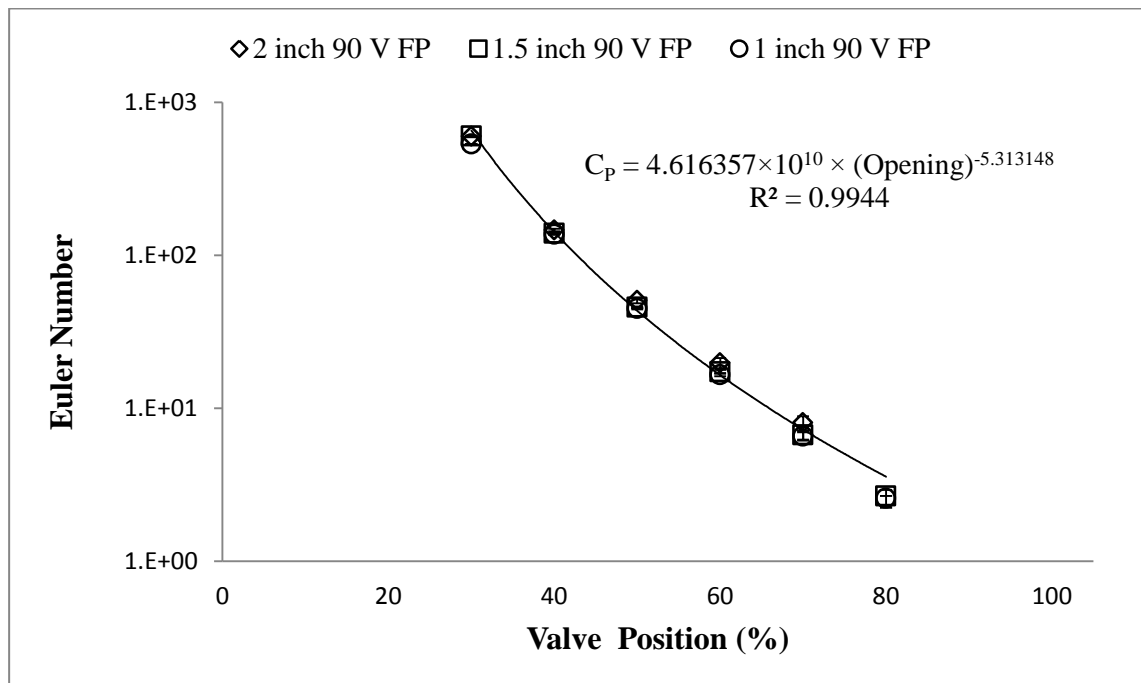


Figure 4-11 Pressure coefficient vs. valve opening for different sizes of 90V full port valves

To ensure that the correlations developed are as accurate as possible, the results of 1 inch pressure coefficients are not included. Since the objective here is to estimate pressure drop in valves larger than 2 inch, this is justified. Using the pressure coefficients obtained, a correlation was developed by fitting a power law curve to the data of 1.5 inch and 2 inch valves for each apex angle as shown in figures 4-8 to 4-11.

Table 4-1 shows the correlation between pressure coefficient and opening of a valve of a given apex angle where the opening is in percentage (e.g. at fully open the opening is 100). Most correlations have a range of applicability and this is also the case here. For all geometries, pressure coefficients were obtained for openings as low as 30% and therefore the lowest range of applicability of these equations is 30%. However for 10V, 30V and 60V ball valves, high enough pressure drops were obtained and the pressure coefficient could be measured within an acceptable accuracy for all openings greater than 30% in these valves. The pressure drops obtained using 90 V ball valves at 100% and 90% openings were not high enough to be within the acceptable error range of the pressure transducers. Therefore no accurate data was obtained for these openings and the correlation for 90V is only applicable for openings as high as 80%. The error associated with using pressure coefficients is also shown in table 4-1. If the error of the correlation were high for higher openings, two error ranges were reported. Otherwise the maximum error is reported as the error of using the correlation.

Valve Geometry	Correlation	Opening Range	Max. Difference
10V	$C_P = 6.563 \times 10^8 (\text{Opening})^{-3.698}$	$30 \leq \text{Opening}$	12.7 %
30 V	$C_P = 1.899 \times 10^{10} (\text{Opening})^{-4.770}$	$30 \leq \text{Opening}$	15.7 %
60V	$C_P = 7.687 \times 10^{10} (\text{Opening})^{-5.262}$	$30 \leq \text{Opening} < 80$	17.0 %
90V	$C_P = 4.616 \times 10^{10} (\text{Opening})^{-5.313}$	$30 \leq \text{Opening} < 70$	17.5 %

Table 4-1 Pressure coefficient vs. opening correlation for different apex angles

The large errors for larger openings are due to the method employed for developing the correlation. Larger openings have smaller pressure coefficient and as the opening reduces, the pressure coefficient increases. As the value of pressure coefficient differs up to three orders of magnitude between the minimum and maximum opening, using least squared errors to obtain a curve fit causes larger errors in the smaller values as their squared error is smaller.

The scalability of the valves is only valid for full port valves and was not observed in standard port valves. This lack of scalability in standard port valves is because of differences in the geometry as the size is increased, as the standard port valves have reducing flanges attached. As Chern et al. [42] have shown the pressure drop is due to the vortices formed which dissipate energy and if the geometry is changing as well as being scaled up, these vortices will perhaps change in size and produce different pressure drop characteristics which in turn makes scalability a function of accelerated velocity and the flow patterns. The standard port results are attached in appendix B. Also an example of flow coefficient scaling using pressure coefficient correlation is discussed in appendix F.

4.1.4 Summary

From the flow coefficient (C_v) results, it can be observed that the 10V 1 inch valves have smaller rate of increase of flow coefficient as opening increases. As the apex angle of the V or the size of the ball increases, change in opening of the valve results in a larger change in flow coefficient. It can be concluded that ball valves with smaller apex angles should be used for fine control applications where large apex angles should be used when a single ball valve is to provide a wide range of flow control. However, a 10V inlet means a high pressure drop and cavitation is more likely to onset in these valves compared to larger apex angles. The same trends were also observed in the standard port valves. The results are attached in the appendix B.

Because of the direct proportionality between flow coefficient and pressure coefficient (shown in appendix C), it is possible to calculate the flow coefficient from pressure coefficient; a useful tool when the flow coefficient of larger valve sizes is to be obtained. Using the correlations, the pressure coefficient for a certain opening of a given apex angle can be obtained and the flow coefficient can be determined from the pressure coefficient and the given pipe average velocity. From the pressure coefficient correlations, it can be observed that scalability of a valve can only be obtained for a given geometry and it is only capable of scaling for different sizes of the same geometry.

4.2. Cavitation Detection

The detection method here is based on cavitation noise at high frequencies. However the first step to detection of cavitation was to obtain the energy of the background noise.

Therefore the valve was taken out and the two pipes were connected using flanges and the system was run for different Reynolds numbers. Reference level (base level) energy was obtained which could be used for comparison against the data recorded when the valve was installed and the loop was run for different flow rates and pressure drops.

4.2.1 Frequency Range Establishment

From the literature review, it was established that the use of energy increase in the kHz range has been tested and proven effective for detection of cavitation inception in valves [13]. This was also supported by the studies of Fitzpatrick et al. [11]. Many researchers have specified frequency ranges greater than 3 kHz to be a suitable lower frequency limit for investigation [13, 29]. However, to ensure that the range specified is applicable to this study, an investigation was carried out using coherence function. If the coherence function has a value greater than 0.6, it indicates that the cross correlation to auto correlation between two signals in a certain frequency is 60% correlated which in turn is a good indicator that the two measurements at that specific frequency were caused by the same source. However, low coherence between two transducers suggests that the source of the energy increase in that frequency is due to different sources, because of lack of correlation between the signals. Initially tests were run without the test valve in the system. The coherence function was obtained for various Reynolds numbers. This indicates acoustic components which are inherent in the system regardless of the test valve and are caused by other devices in the system such as the pump, upstream regulatory valves and turbine flow meter.

Figures 4-12 and 4-13 show the coherence between the two dynamic pressure transducers and the coherence between accelerometer and downstream pressure transducer. From these figures, the existence of coherent vibrations in frequencies less than 2 kHz caused by other components such as the pump and the turbine flow meter is evident. Therefore, the lower limit of the energy integral is set to be at 2 kHz. There are coherent components at 12.5 kHz and its harmonics. This is due to vibrations of the electrical motor of the pump as the carrier frequency of the pump controller is set to 12.5 kHz. This noise was not filtered to attempt detection of cavitation despite the existence of background noise to mimic industrial conditions where background noise cannot be identified and eliminated.

Power spectrum density of each sensor is shown on Figure 4-14 to 4-16. The coherence function and the power spectrum density of the two dynamic pressure transducers have peaks at the same frequencies and hence the high coherence in the 0.1 kHz to 1 kHz frequency range.

Given the fact that there is no valve in the loop, one would expect the two to be almost identical. This is not the case as one sensor may be closer to a source of background noise compared to the other one. An example of this is the noise induced by the carrier frequency of the pump controller. In the case of this carrier frequency, the downstream sensor is closer to the pump and detects the pump noise at 12.5 kHz compared to the upstream sensor which does not detect any signal at 12.5 kHz because it is further away from the pump. As the downstream pressure transducer is closer to the pump and the controller, the hypothesis of noise affecting the power spectrum in pressure transducers seems to be legitimate.

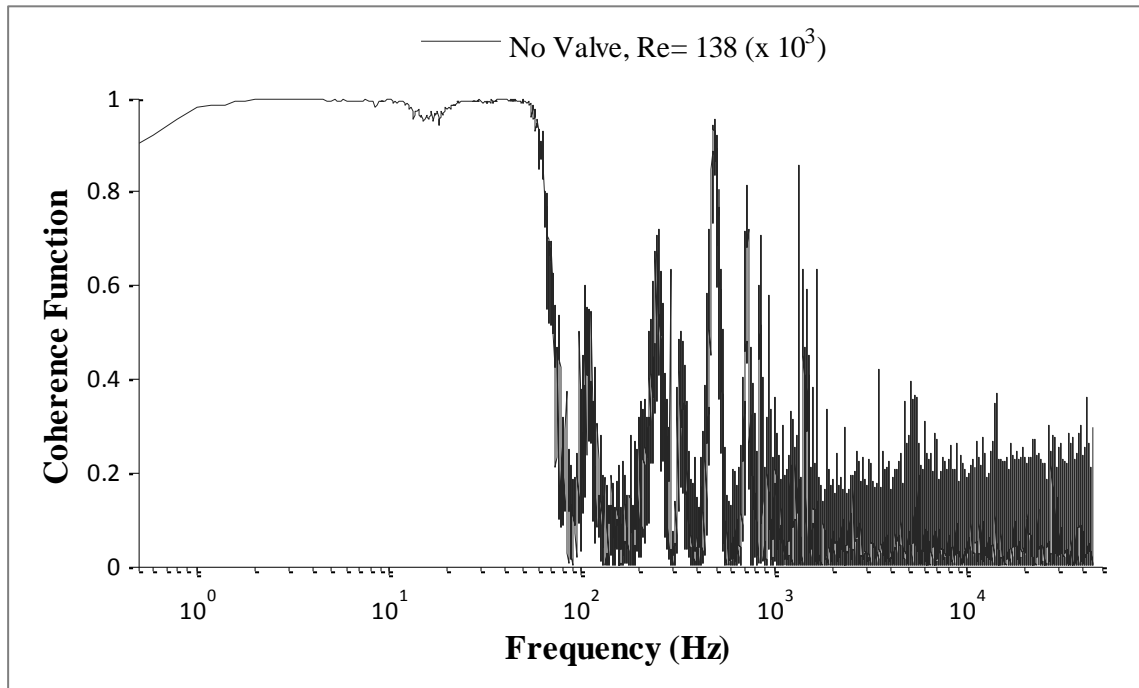


Figure 4-12 Coherence function between upstream and downstream pressure transducers

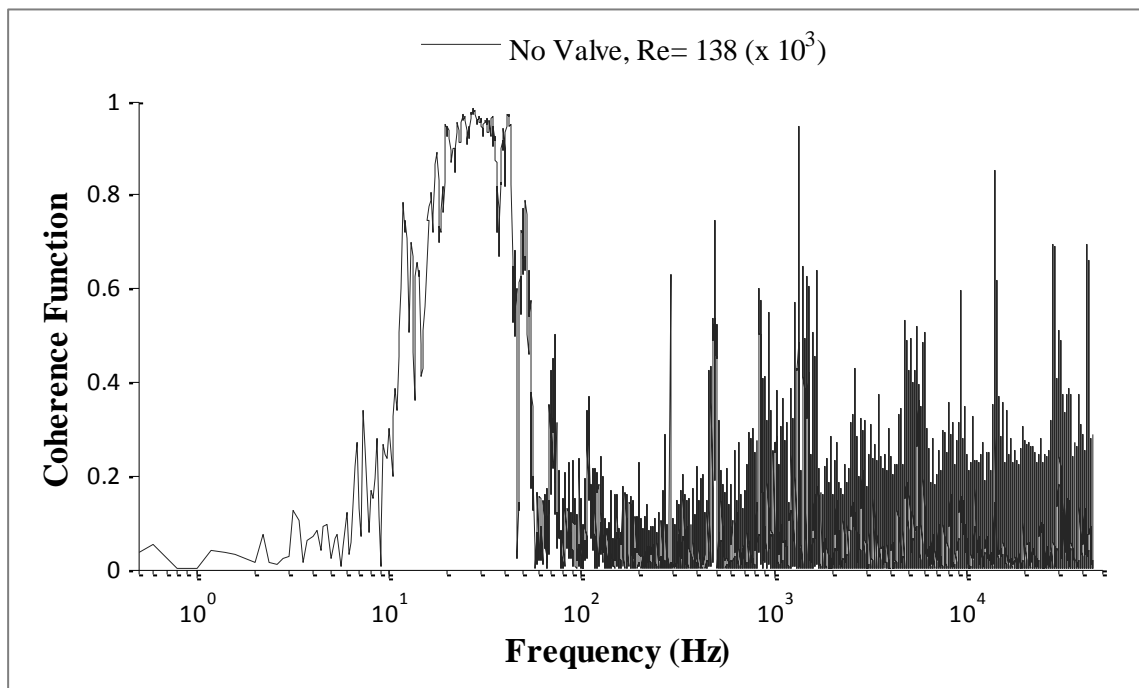


Figure 4-13 Coherence function between downstream accelerometer and downstream pressure transducers

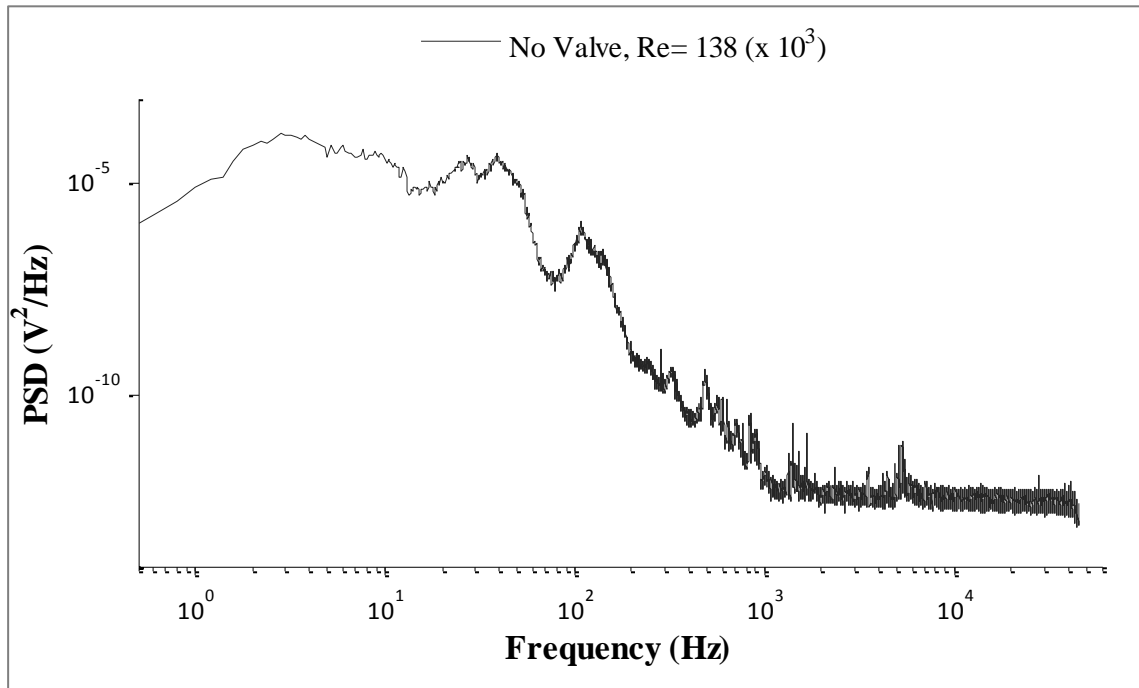


Figure 4-14 Power spectrum density of the upstream dynamic pressure transducer (No Valve)

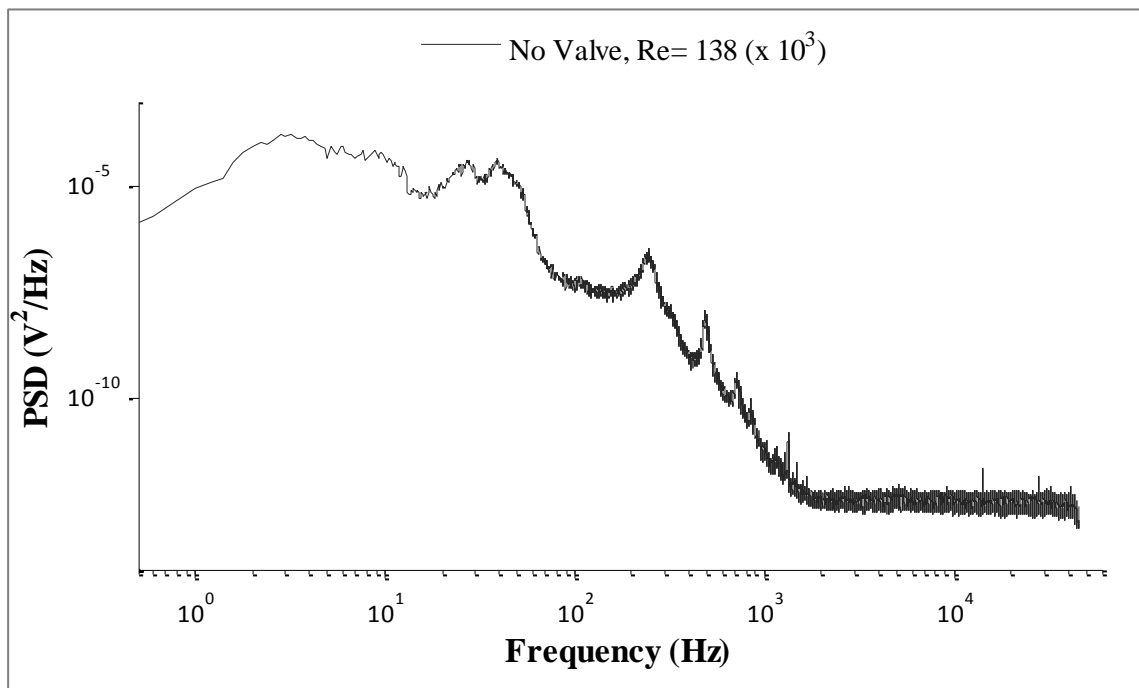


Figure 4-15 Power spectrum density of the downstream dynamic pressure transducer (No Valve)

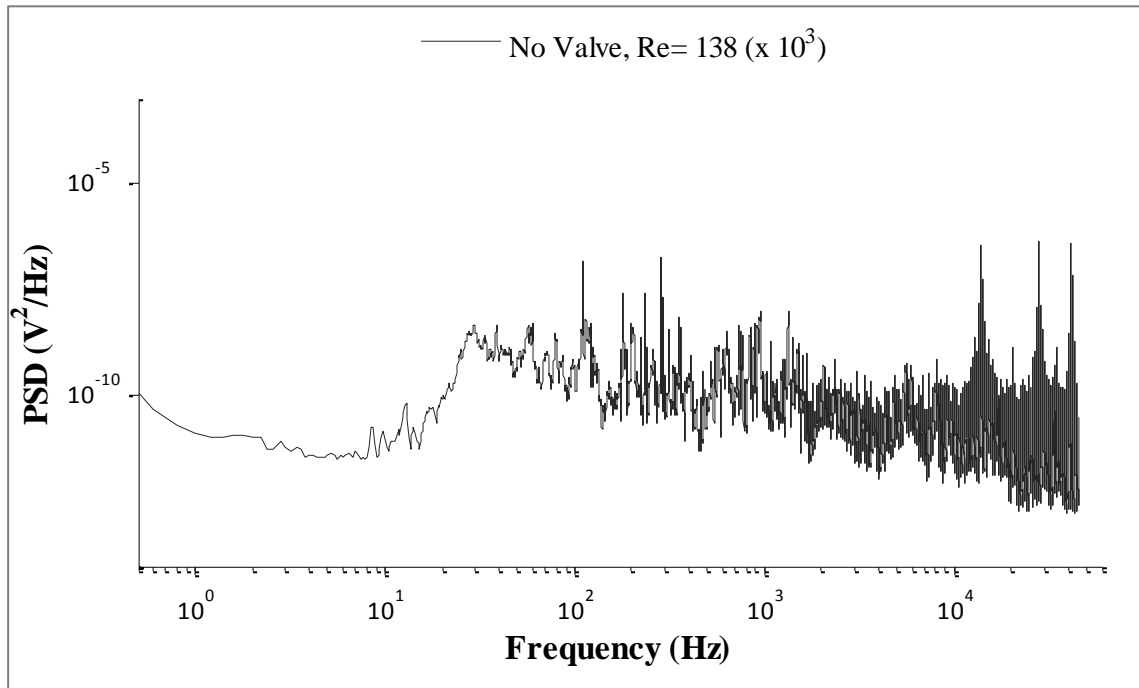


Figure 4-16 Power spectrum density of the accelerometer (No Valve)

4.2.2 Cavitation Detection Using Dynamic Pressure

In the next, step the power spectrum density was numerically integrated to obtain the energy level at different Reynolds numbers when there was no valve installed in the system. Three different frequency ranges were defined. The first frequency range is 2-5 kHz, the second is 5-10 kHz and the third is 10 to 45 kHz range.

Figures 4-17 and 4-18 show the base energy when no valve is installed for the frequency range of 2 to 5 kHz, Figures 4-19 and 4-20 represent the energy in the 5 to 10 kHz frequency band and figures 4-21 and 4-22 represent the energy in the 10 to 45 kHz frequency band when no valve is installed.

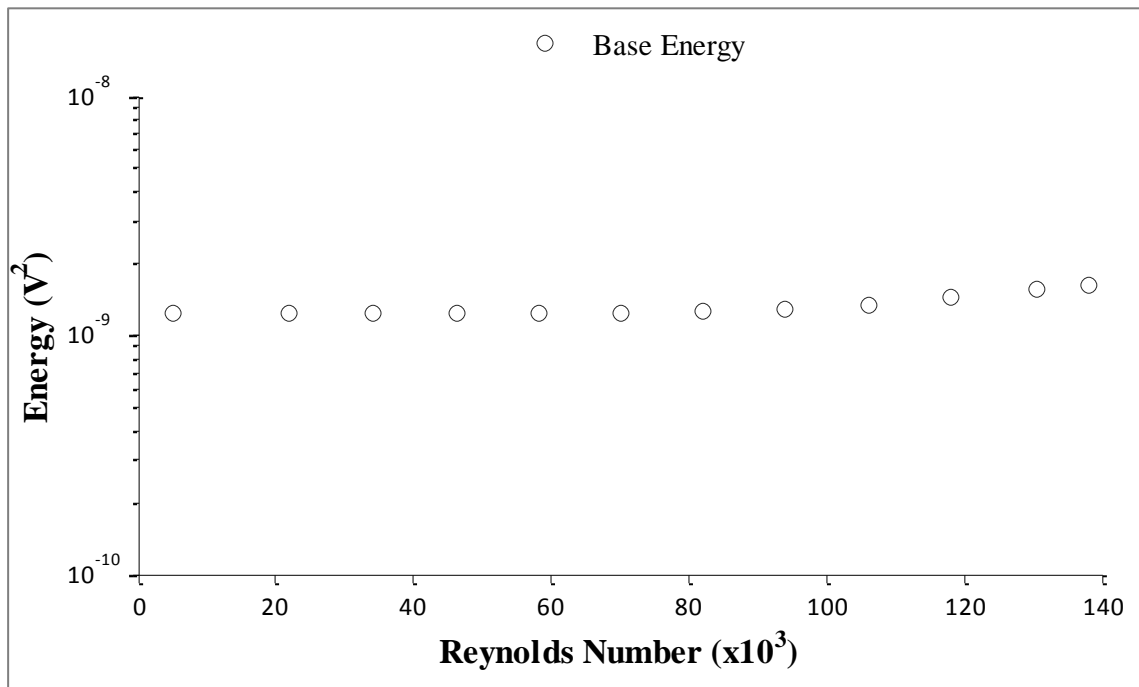


Figure 4-17 Energy of upstream pressure transducer in the 2 to 5 kHz frequency range (No Valve)

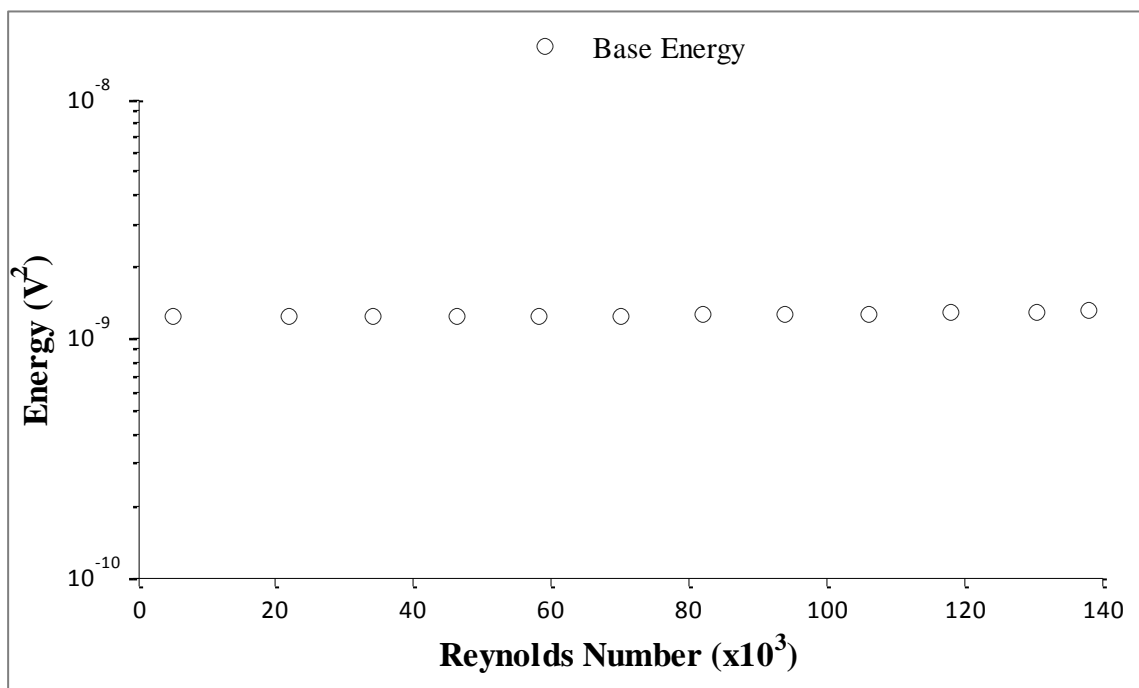


Figure 4-18 Energy of downstream pressure transducer in the 2 to 5 kHz frequency range (No Valve)

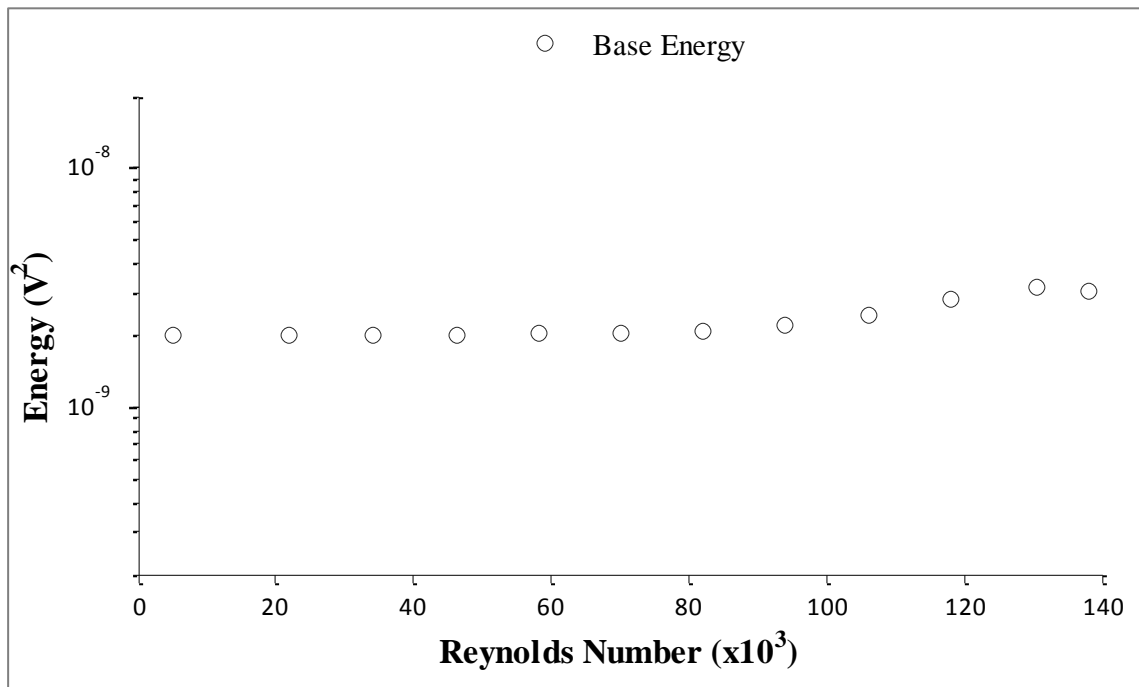


Figure 4-19 Energy of upstream pressure transducer in the 5 to 10 kHz frequency range (No Valve)

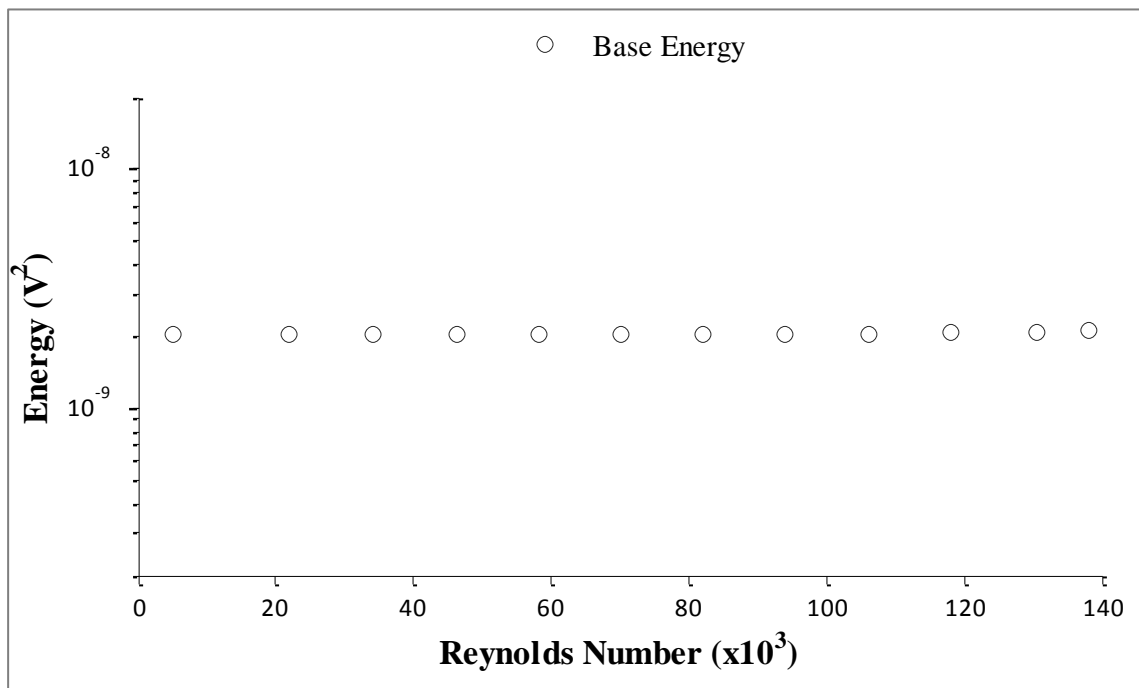


Figure 4-20 Energy of downstream pressure transducer in the 5 to 10 kHz frequency range (No Valve)

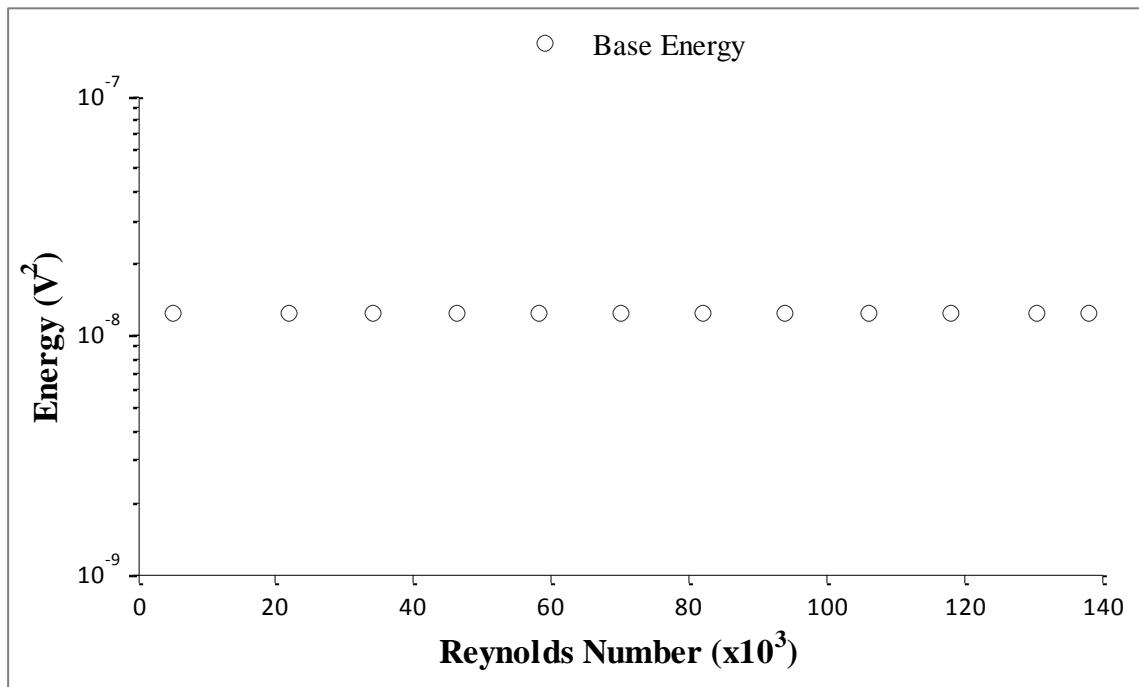


Figure 4-21 Energy of the upstream pressure fluctuations in the 10 to 45 kHz frequency range (No Valve)

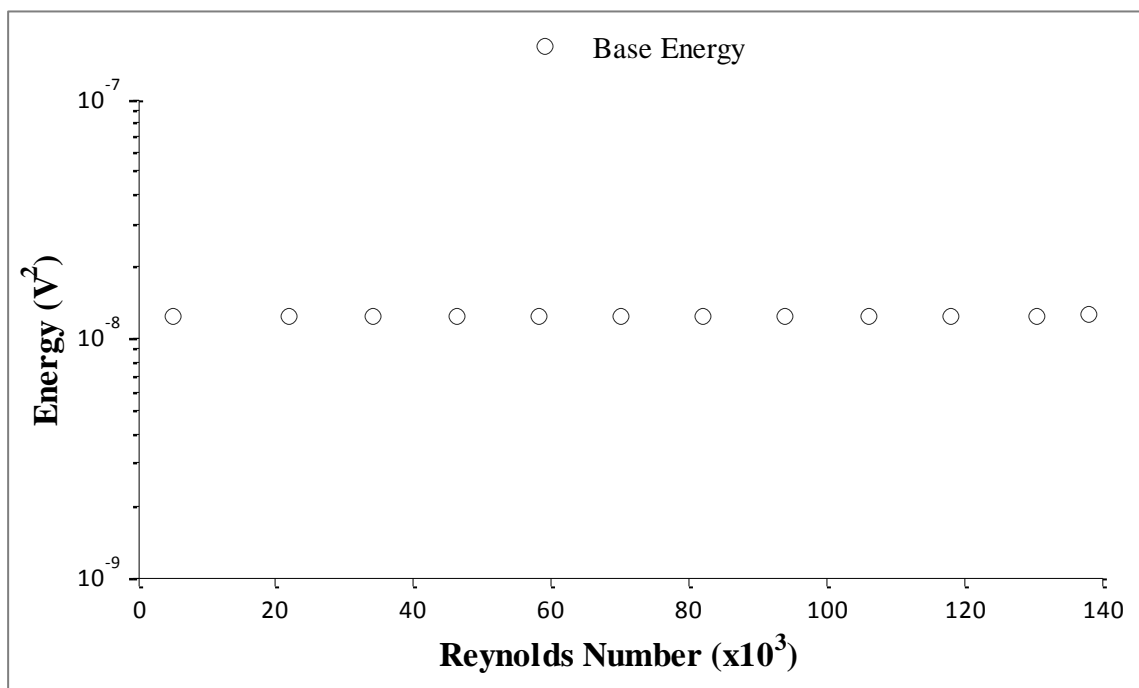


Figure 4-22 Energy of downstream pressure fluctuations in the 10 to 45 kHz frequency range (No Valve)

From figures 4-17 to 4-22, it can be seen that an increase in Reynolds number does not cause an increase in the energy level beyond 2 kHz. This is perhaps due to the design of the port, the small cross-section of the neck and the vortices formed within the neck which acts as a damper to high frequency pressure fluctuations. It is worthy to note that in the frequency range of 2 to 5 kHz and 5 to 10 kHz, there are fewer frequency components and therefore the overall energy is less than the 10 to 45 kHz range.

After obtaining the energy levels without a valve in the line, the test valve was installed and the flow was run for different pipe Reynolds numbers. The data was recorded and analysed and the energy plots were obtained against a base energy level when no valve was installed in the loop. Figures 4-23 and Figure 4-24 show the change in 2 to 5 kHz frequency range with Reynolds number for dynamic pressure transducers. The data starts to depart from the reference with an exponential trend (which is seen as a line on a semilog plot) until it reaches a certain value, then the rate of energy increase becomes smaller although it still has an exponential increase. This exponential increase in the energy on a log scale was observed by other investigators such as Martin et al. [13] and Fu et al. [34]. The start of the exponential energy increase region is noted as the cavitation inception. The initial rate of increase is perhaps caused by intermittent cavitation; Ran et al. [22] have shown that at cavitation inception, occurrence of cavitation is a probability and therefore it is not occurring 100% of the time continuously when there are significant numbers of air bubbles.

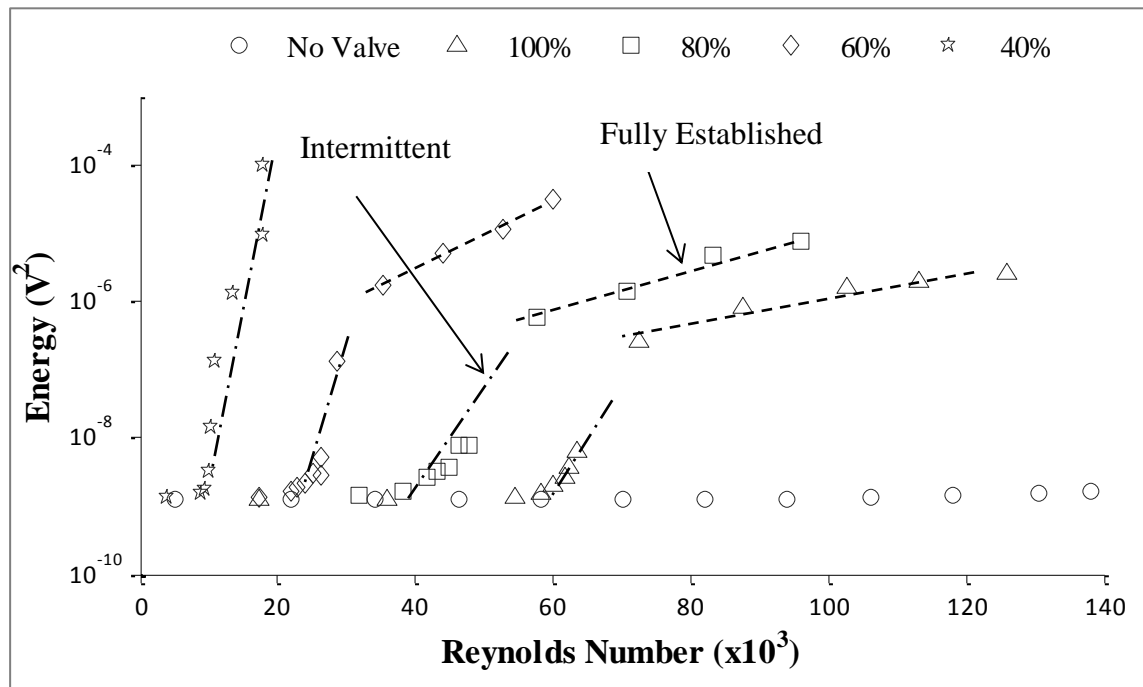


Figure 4-23 Upstream 2 to 5 kHz frequency range energy level for 1 inch 30V Standard Port valve vs. no valve installed for some openings

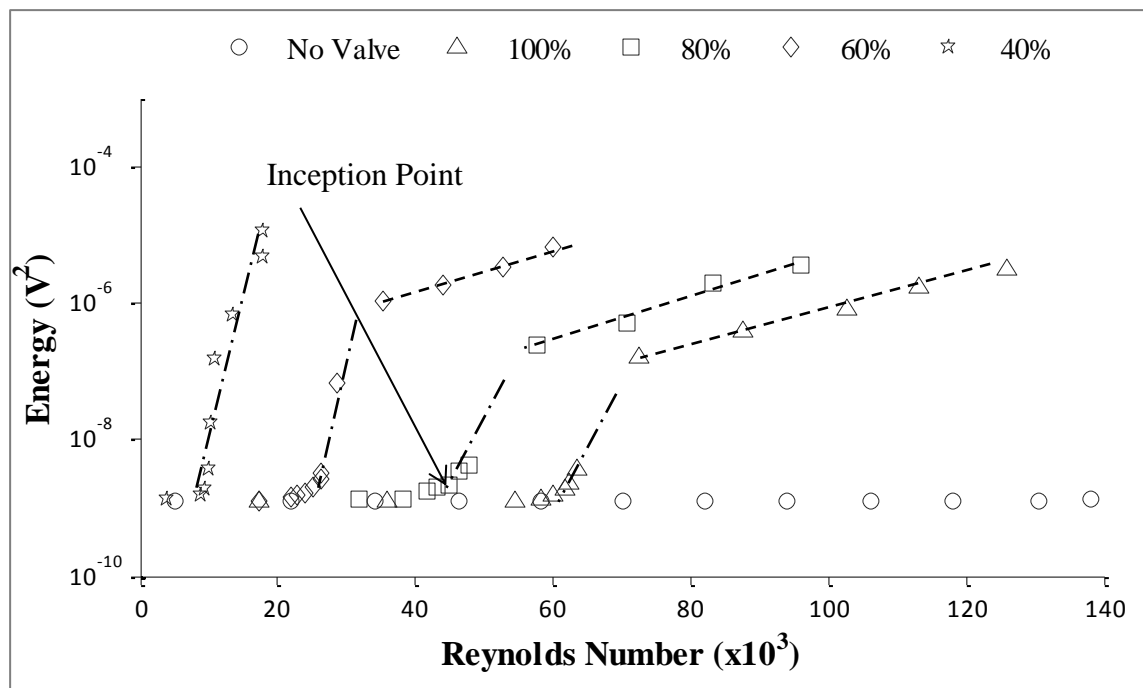


Figure 4-24 Downstream 2 to 5 kHz energy level for 1 inch 30V standard port valve vs. no valve installed for some openings

The initial steep rate of increase is because of the intermittent cavitation. This is due to the effect of permanent gas (air) nuclei on cavitation inception. At inception only large nuclei cause a cavitation bubble to be formed and as Reynolds number increases and cavitation number decreases, smaller nuclei are capable of causing cavitation, hence an increase in cavitation events in number in the same period of time. This results in a steep exponential rate of energy increase from inception point until a point at which cavitation occurs continuously. From this point on, the second rate of increase in the energy can be observed which is referred to as fully developed cavitation which has a smaller exponential rate of increase.

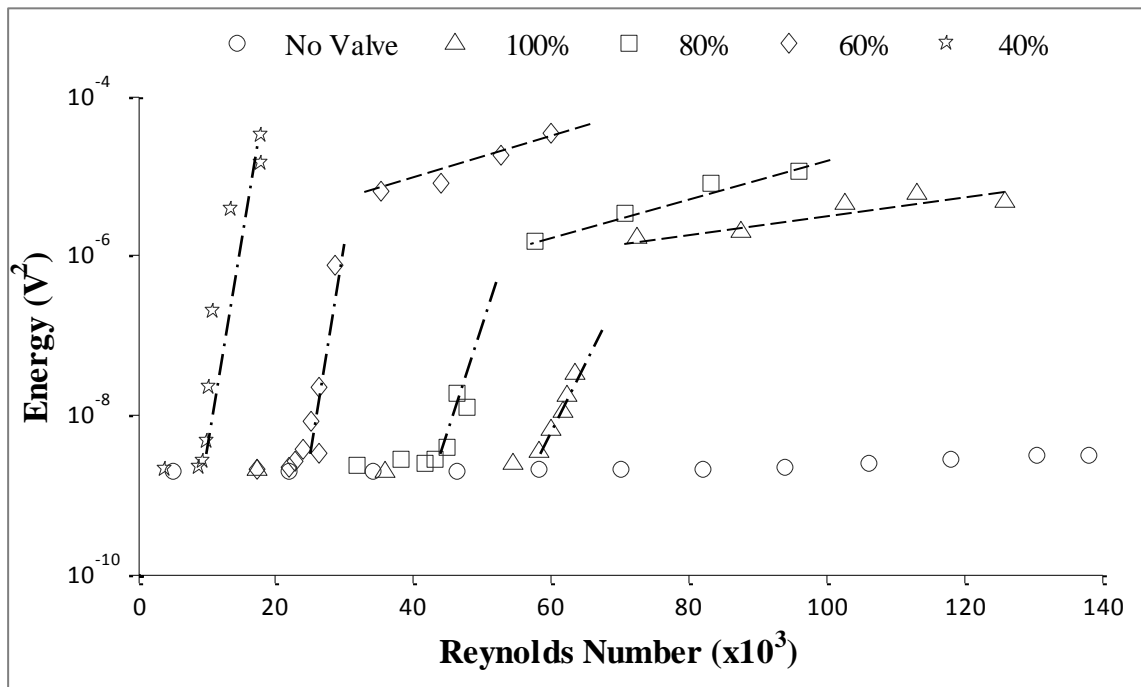


Figure 4-25 Upstream 5 to 10 kHz frequency range energy level for 1 inch 30V Standard Port valve vs. no valve installed for various openings

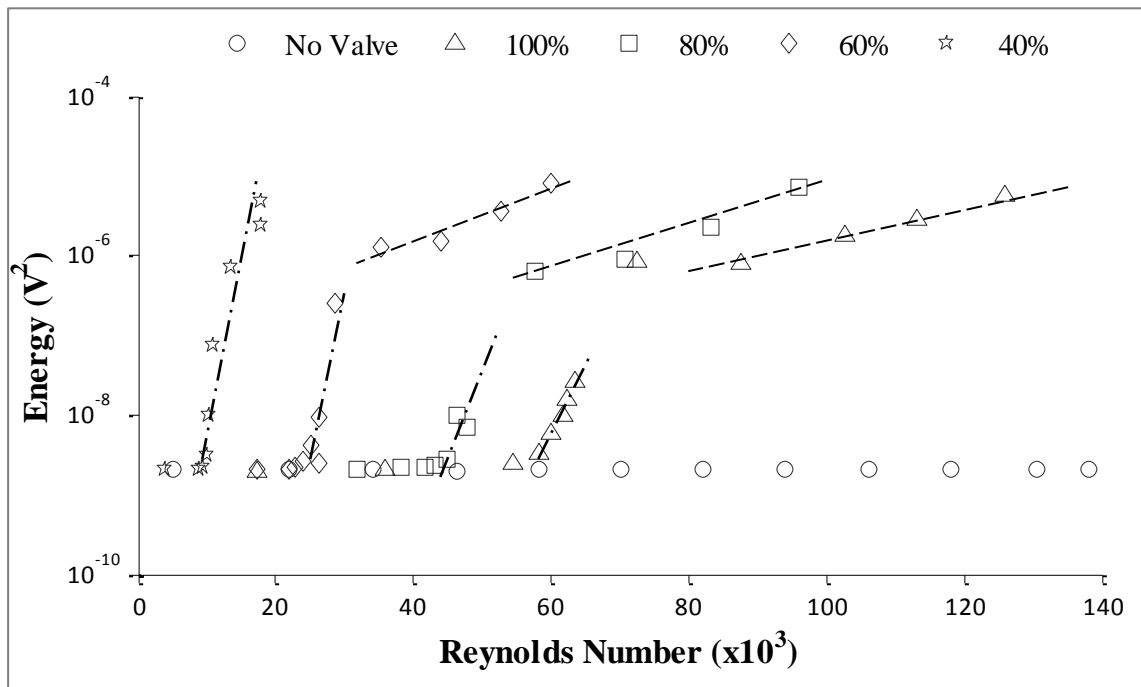


Figure 4-26 Downstream 5 to 10 kHz frequency range energy level for 1 inch 30V Standard Port valve vs. no valve installed for various openings

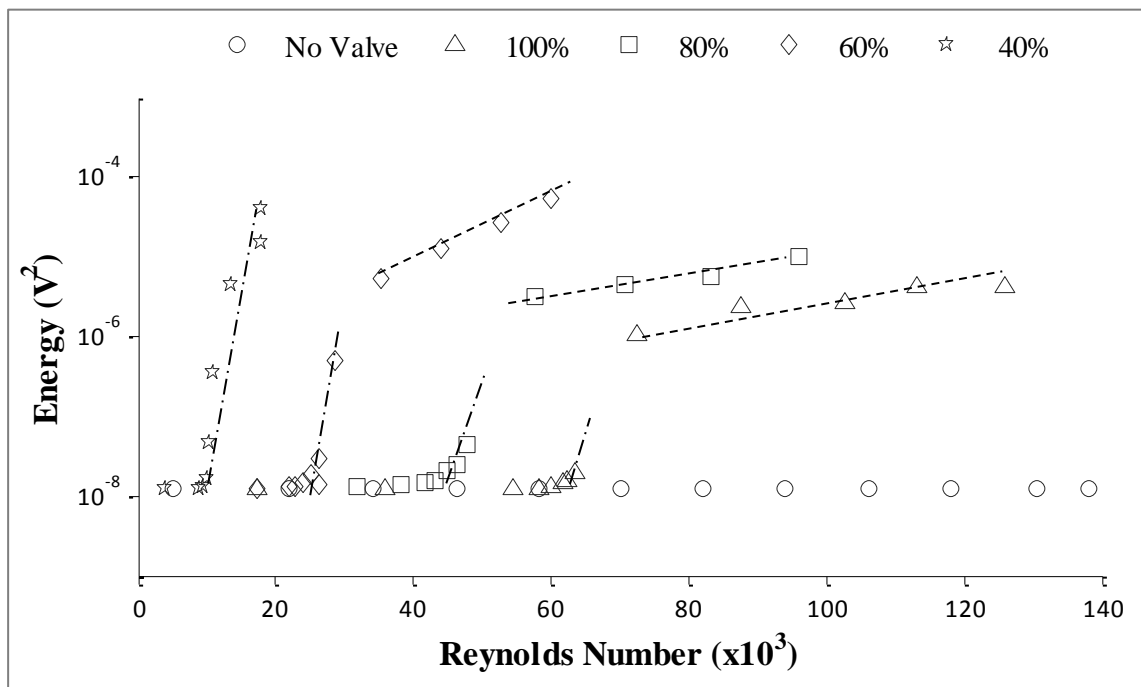


Figure 4-27 Upstream 10 to 45 kHz frequency range energy level when for 1 inch 30V Standard Port valve vs. no valve installed for various openings

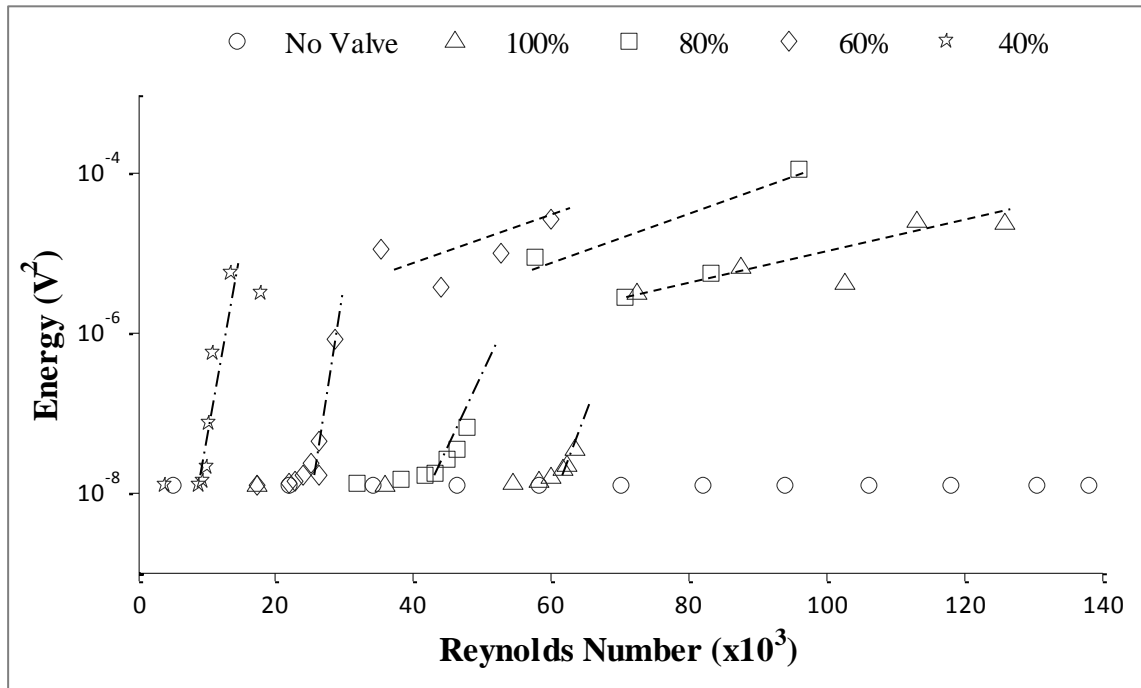


Figure 4-28 Downstream 10 to 45 kHz frequency range energy level when for 1 inch 30V Standard Port valve vs. no valve installed for various openings

In the 40% open case only the first steep exponential increase in energy (intermittent cavitation) was observed because high Reynolds numbers were not tested at this opening and it is likely that fully developed cavitation was not reached. Figures 4-25 and 4-26 show the increase in energy compared to the base case in the frequency range of 5 to 10 kHz when the 1 inch standard port valve was installed and a 30V ball was used.

Figures 4-27 and 4-28 show the change in energy of the dynamic pressure for frequency range of 10 to 45 kHz. The same trends are observed as the previous frequency bands for the dynamic pressure transducers. To obtain the exact point of cavitation inception, the inception Reynolds number is obtained for each opening and the corresponding cavitation number is chosen as inception cavitation number. However in most cases as cavitation inception occurs, the energy increase is observed initially in one of the frequency bands

defined. In such cases, all frequency band plots are compared and the one that outlines an energy increase at the smaller Reynolds number is taken to be the point of cavitation inception to be conservative. This procedure ensures that cavitation inception is recorded exactly at the first sight of cavitation onset. In the next section cavitation detection using cost effective accelerometers is attempted.

4.2.3 Cavitation Detection Using Accelerometer

An attempt was made here to use a low cost accelerometer for robust cavitation detection in industrial plants. The analysis procedure is the same as the one used for dynamic transducers. The base energy levels are obtained for different pipe Reynolds numbers for two frequency bands of 2 to 5 kHz and 5 to 10 kHz. Since the linear range of the accelerometer is between 0.3 to 10 kHz the frequency range of 10 to 45 kHz is disregarded. Figures 4-29 and 4-30 show the base energy of vibrations for different pipe Reynolds numbers.

The energy increases in the accelerometer have an exponential rate like that of dynamic pressure transducers. The energy level decreases initially, as flow rates for Reynolds numbers less than 40,000 are measured using low flowmeter and switching the flowmeters changes the vibrations in the system. Since the flowmeters used are turbine flowmeters, each have unique vibrational noise characteristics associated with that family of flowmeters and switching from one to the other changes the vibrations characteristics of the system. For pipe Reynolds numbers above 40,000 however the high flowmeter was used and an increase in flow rate causes an increase in the vibrational energy.

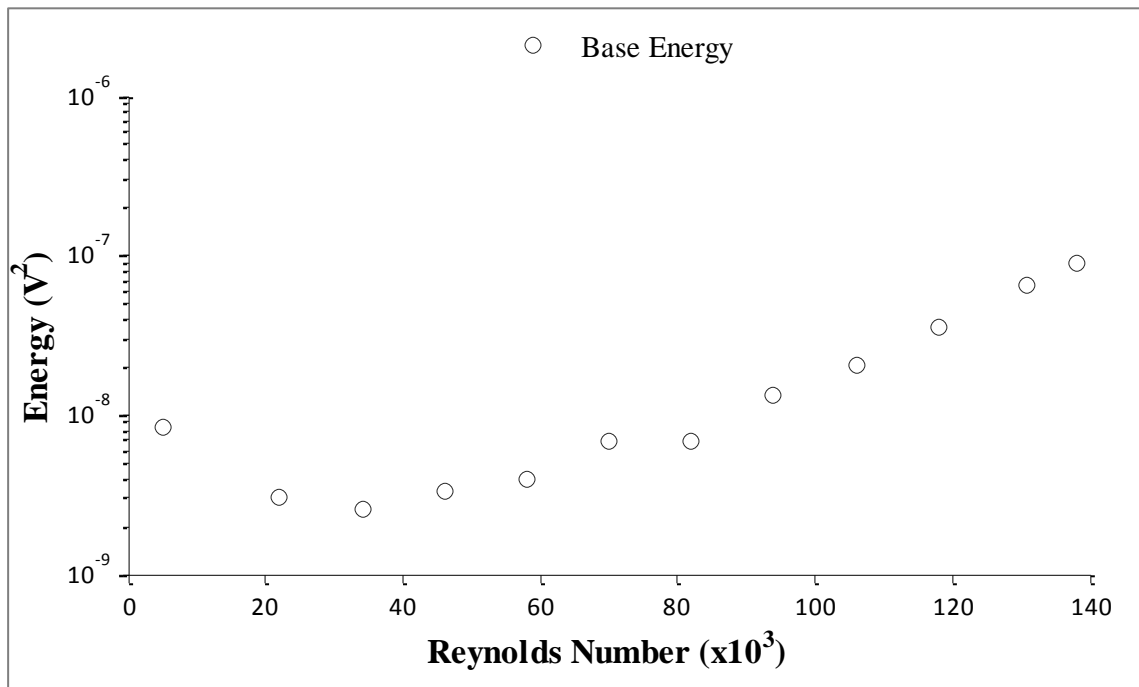


Figure 4-29 Energy of accelerometer in the 2 to 5 kHz frequency range (No Valve)

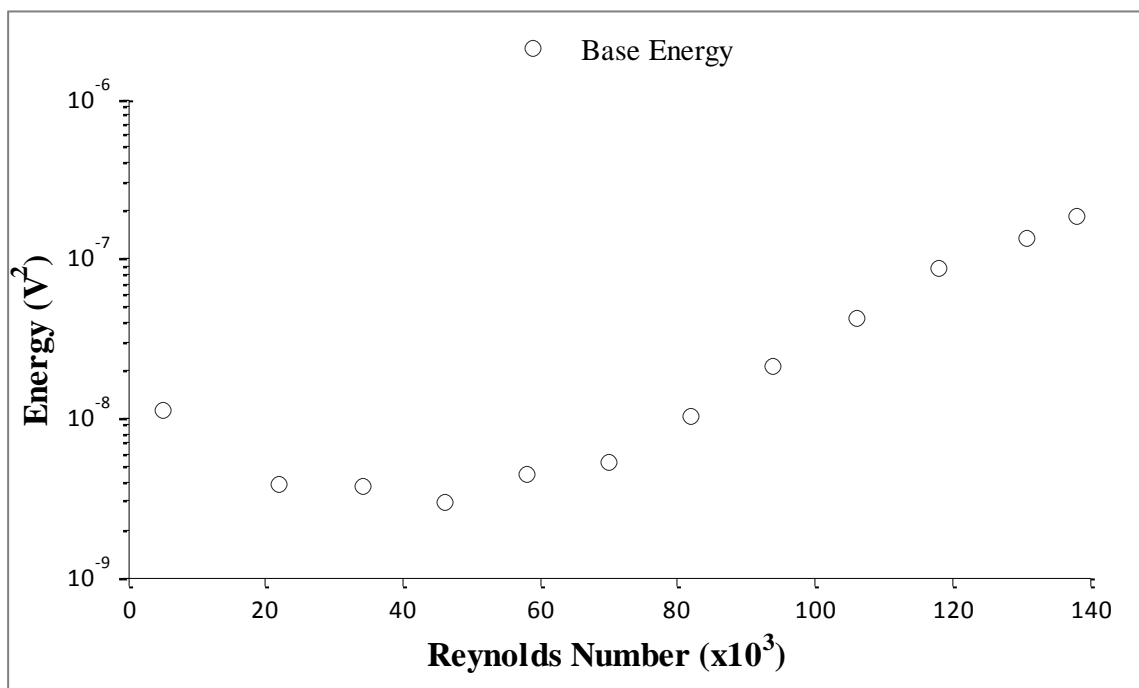


Figure 4-30 Energy of accelerometer in the 5 to 10 kHz frequency range (No Valve)

Figures 4-31 and 4-32 show the changes in energy of accelerometers in 2 to 5 kHz and 5 to 10 kHz frequency bands respectively. From these figures, the changes in energy of accelerometers with a maximum frequency up to 10 kHz results in different cavitation inception numbers compared to that of a dynamic pressure transducer depending on the frequency range chosen. Tables 4-2 and 4-3 show the inception cavitation number predicted using accelerometer. From these two tables, it can be observed that using data obtained from 5 to 10 kHz frequency range energies is in better agreement with acoustic measurements compared to that obtained using 2 to 5 kHz frequency range energies. Therefore, the suggested frequency range to be used with accelerometers is 5 to 10 kHz.

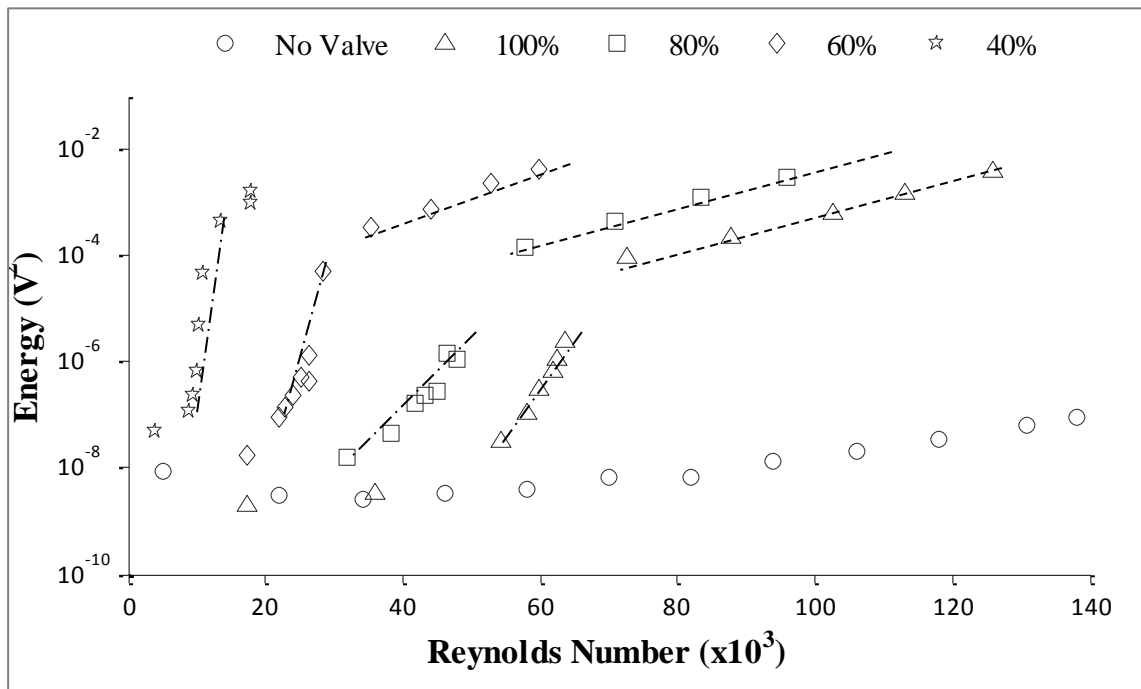


Figure 4-31 Accelerometer 2 to 5 kHz energy level for 1 inch 30V Standard Port valve vs. no valve installed for various openings

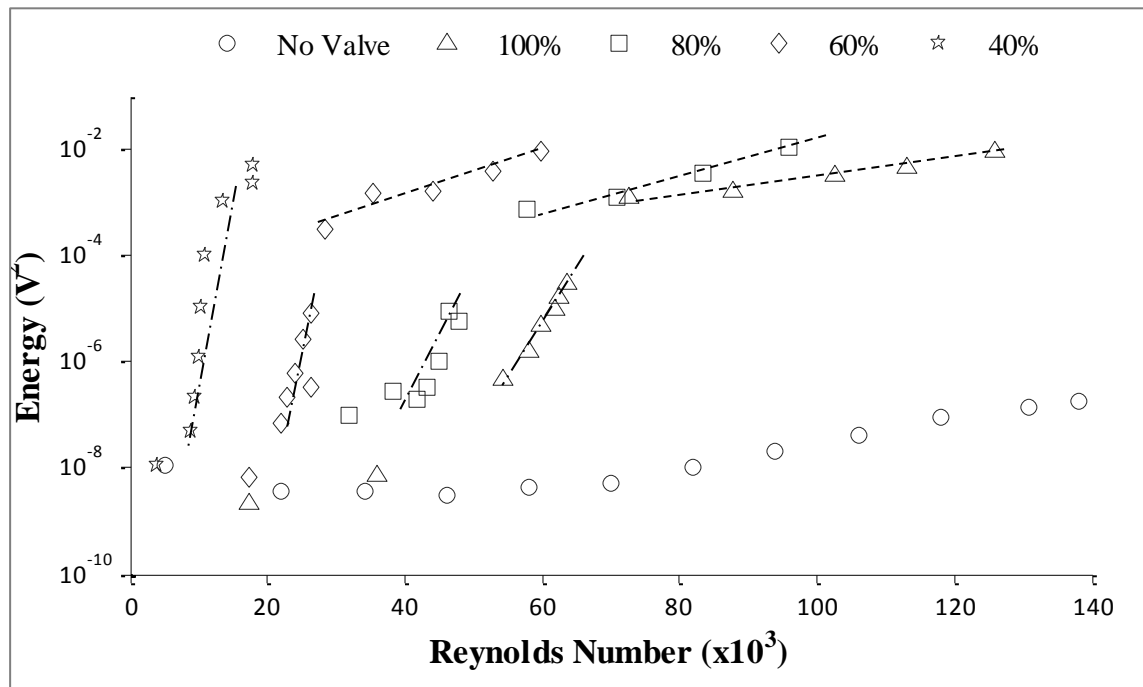


Figure 4-32 Accelerometer 5 to 10 kHz frequency range energy level for 1 inch 30V Standard Port valve vs. no valve installed for various openings

Opening (%)	Inception Cavitation Number (Accelerometer)	Inception Cavitation Number (dynamic pressure transducer)
100	5.0	5.0
80	3.47	3.36
60	3.43	2.55
40	2.45	1.96

Table 4-2 Comparison of cavitation inception number predicted by accelerometer vs. dynamic pressure transducer using 2 to 5 kHz frequency band energies

Opening (%)	Inception Cavitation Number (Accelerometer)	Inception Cavitation Number (dynamic pressure transducer)
100	5.0	5.0
80	3.47	3.36
60	2.55	2.55
40	2.16	1.96

Table 4-3 Comparison of cavitation inception number predicted by accelerometer vs. dynamic pressure transducer using 5 to 10 kHz frequency band energies

Unfortunately as valves are installed, the vibrational characteristics of the piping are changed due to substantial mass of the valve and damping of the gasket installed, which causes a different frequency response in the system and perhaps changes the reference obtained energies. These small deviations indicate that using accelerometers may not be the better method for pinpointing the cavitation inception. However it can indicate occurrence of cavitation and whether it is intermittent or fully developed.

To establish the regime of cavitation, the time domain information of the accelerometer is valuable as cavitation causes the accelerometer to have an impulse response to the collapse of a bubble. The studies performed by Plesset et al. [9] and validated by Lauterborn [10] show that cavitation causes high velocity jets which could cause an impulse excitation in the pipe. Therefore to determine the regime of cavitation, time domain data should be observed as well.

Figure 4-33 shows the operation of the pipeline when no valve is installed at the highest achieved Reynolds number. The output is nearly flat. This is the same in Figure 4-34

where the valve is installed but from the energy plots, cavitation is not expected. Figure 4-35 shows the operation of the valve under intermittent cavitation regime according to the energy plots provided by dynamic pressure transducers. Small peaks can be seen in this figure, which occur at different times that indicate intermittent cavitation is occurring and therefore causing an impulse response. Figure 4-36 shows the changes in output of the accelerometer as Reynolds number increases and cavitation becomes fully developed. As Reynolds number increases, cavitation number decreases and the number of impulse responses increase and more peaks are observed. When the fully developed cavitation regime is reached, peaks become the dominant signal which indicate continuous occurrence of cavitation.

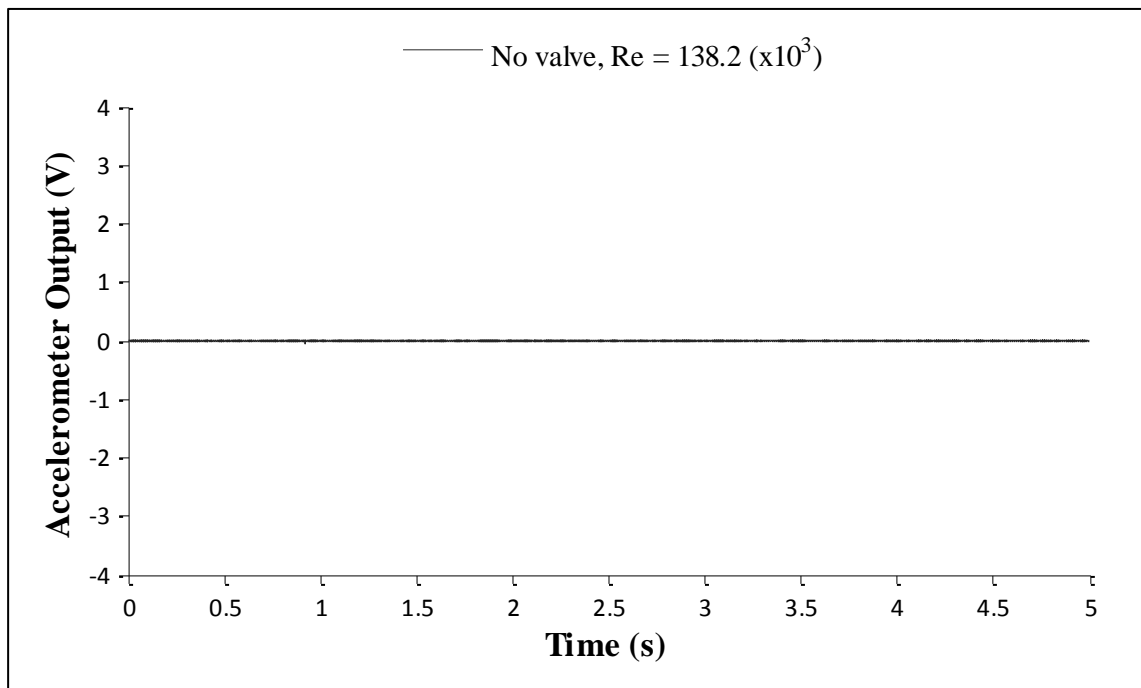


Figure 4-33 Accelerometer output in time domain, Pipe Reynolds number = 138,200

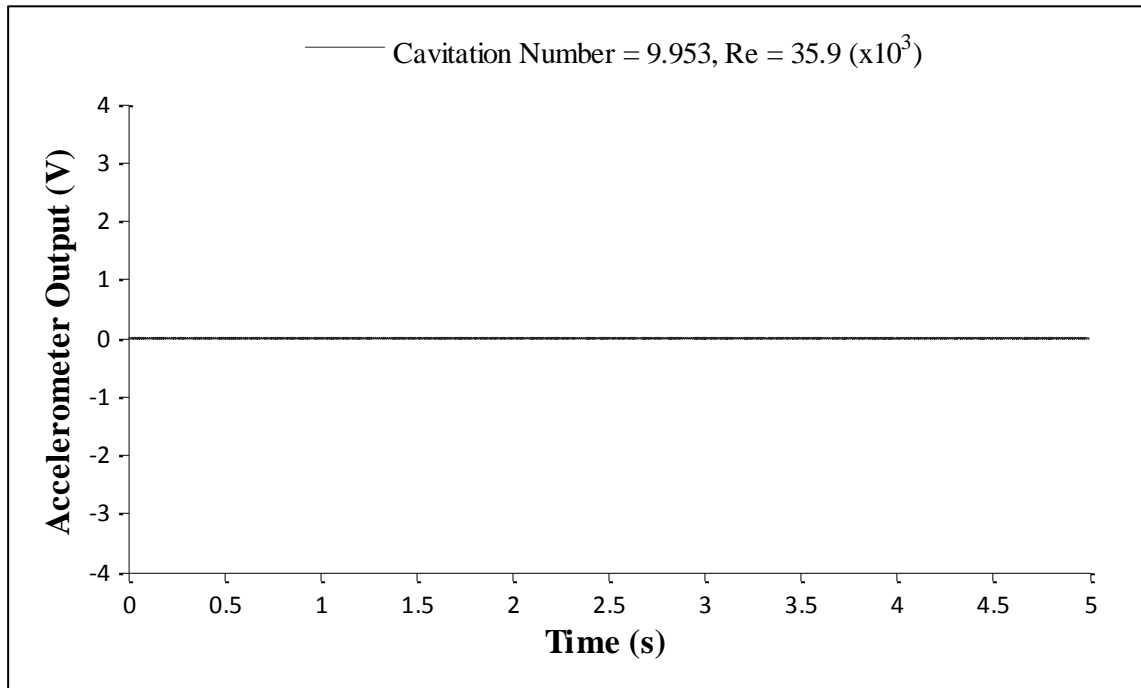


Figure 4-34 Accelerometer under non cavitating operation for 1 inch 30V standard port valve 100% open

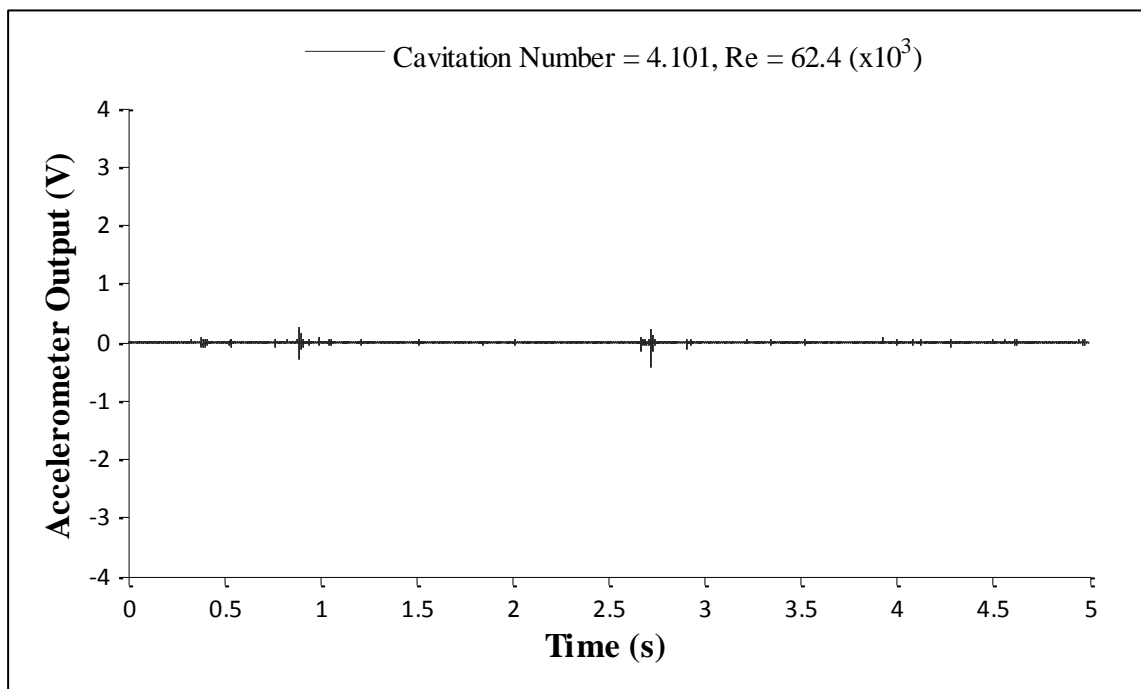


Figure 4-35 Accelerometer under intermittent cavitation inception operation for 1 inch 30V standard port valve 100% open

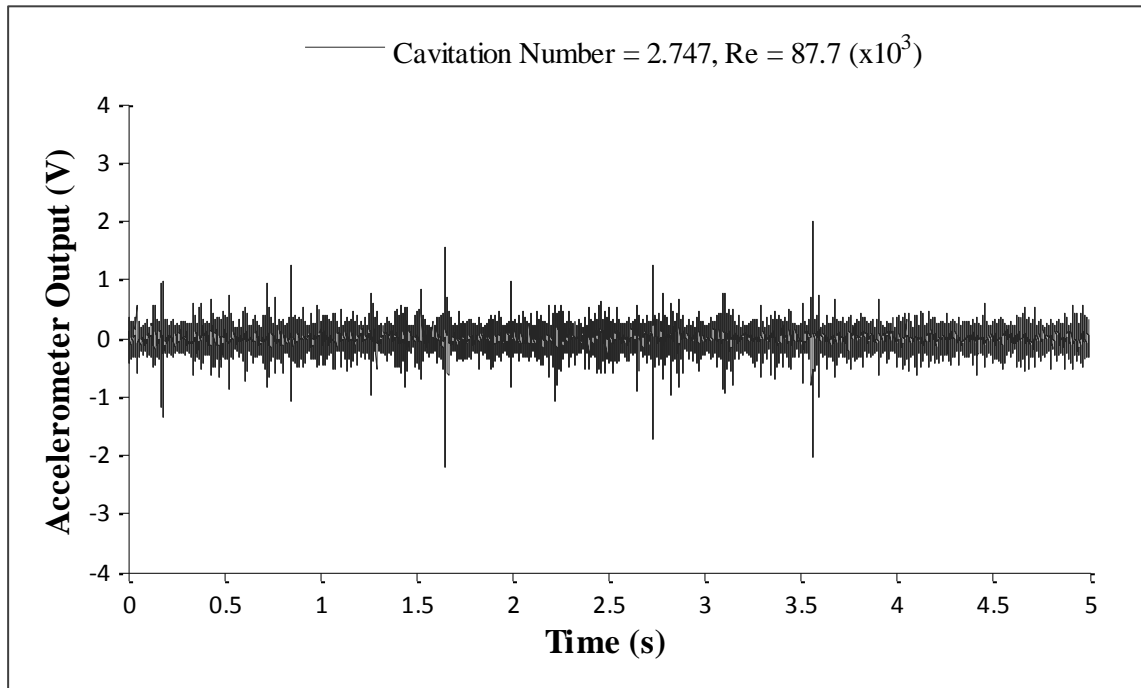


Figure 4-36 Accelerometer under onset of fully developed cavitation operation for 1 inch 30V standard port valve 100% open

However the signal in figure 4-36 shows continuous cavitation which agrees with the data of figure 4-23 as the point of reduced rate of increase and starting point of fully developed cavitation inception.

These two arguments both suggest that cavitation inception is indeed an intermittent cavitation phenomenon where the point at which energy increase starts to occur at a much lower rate corresponds to fully developed cavitation regime where bubbles are formed and collapsed continuously.

To detect inception of cavitation, inception cavitation numbers of both acoustic measurements and accelerometer are investigated and when both sensors indicate cavitation inception, the corresponding cavitation number is chosen as the inception

cavitation number. Using the time domain data of accelerometers, the regime of cavitation occurrence can be determined.

By revisiting performance drop observed in 1 inch 30V standard port valve (Figure 4-3), the link between cavitation inception and increased pressure drop can be observed. The energy increase in the case of the 100% open valve explains the reduction in performance of the valve shown in figure 4-3. By comparing the two figures, it is possible to see that the performance drop does not occur until fully developed cavitation is reached. This reduction of performance and increase in pressure drop means energy is being dissipated as a result of cavitation. Three mechanisms could cause this energy loss. First mechanism is the increased drag within the flow as a result of existence of bubbles in the flow. The second energy dissipative mechanism is the collapse of the bubble and local high velocity jets and the third mechanism is noise generation which perhaps dissipates energy and causes further pressure drop.

4.2.4 Discussion of Frequency Spectral Behaviour

Another issue that must be addressed here is the reason behind the behaviour observed in the energy plots. At inception it was observed that cavitation is intermittent and as pressure drop or velocity increase is continued, the cavitation regime becomes established. This is due to the mechanism at which cavitation occurs. In a pure liquid, it is expected that as cavitation occurs, the bubbles are very small and therefore have collapse frequencies in the higher kHz range. As these bubbles grow larger as a result of further pressure reduction, the collapse acoustic frequency should decrease. However, this was

not the observed trend here. By having a glance at Figure 4-23 Upstream 2 to 5 kHz frequency range energy level for 1 inch 30V Standard Port valve vs. no valve installed for some openings figures 4-23 to 4-28, it is possible to see that the steep exponential rate occurs in 2 to 5 KHz and 5 to 10 KHz range bands earlier compared to the 10 to 45 KHz frequency band. This suggests that cavitation first occurs within 2 to 10 KHz range which corresponds to larger bubbles and as further pressure drop occurs, smaller bubbles are formed as well as the previous larger bubbles.

The inception of cavitation in the lower frequency bands can be explained by considering air bubbles as cavitation nucleation seeds. Since water used here is not degassed, it is very likely that the air bubbles cause the cavitation inception. Since inception occurs in 2 to 10 KHz range, then using the theory developed by Fitzpatrick et al. [11], it is possible to estimate the air bubble sizes which cause cavitation onset. Using the same argument as used in chapter 2.1.3 the range of time constants can be estimated using the frequency range as:

$$\tau_c = \frac{SPL_{High}}{f_{High}} = \frac{0.6}{10,000} = 6 \times 10^{-5} S$$

$$\tau_c = \frac{SPL_{Low}}{f_{Low}} = \frac{0.2}{2000} = 1 \times 10^{-4} S$$

Using the equation derived by Rayleigh [4]:

$$R_i = \frac{\tau_c}{0.915 \sqrt{\rho_l / (P_l - P_v)}}$$

For the highest possible time constant and assuming the bubble to collapse at 120,000 kPa absolute, we have:

$$R_i = \frac{1 \times 10^{-4}}{0.915 \sqrt{999.8/(120,000 - 2400)}} = 1.2 \text{ mm}$$

and for the lowest possible time constant and assuming the same pressure as above the smallest possible diameter at collapse is estimated as:

$$R_i = \frac{6 \times 10^{-5}}{0.915 \sqrt{999.8/(50,000 - 2400)}} = 0.7 \text{ mm}$$

These estimate values seem realistic as Brennen [8] shows that a nucleation bubble could grow to 100 times of the nucleation seed which caused the bubble growth.

The analysis performed here shows why the intermittent behaviour occurs. It also shows why the frequency of the bubbles at inception is not high as they have nucleated from an air bubble which allows them to grow into rather large sizes. For cavitation to occur, an air bubble of the “right size” must be convected into the low pressure regions. At cavitation inception, this convection of suitable nucleation seed is a probability and therefore at cavitation onset, the process is intermittent as it relies on the “right bubble size” in the low pressure region. This is in agreement with the work performed by Ran et al [22] who have shown that at cavitation inception, occurrence of cavitation is a probability and as cavitation number decreases, the probability increases until it reaches a threshold where no nucleation seed is required for cavitation to occur as the region of low pressure is sufficiently large to cause bubble formation without nucleation seeds.

4.2.5 Cavitation Inception Characteristics

To investigate cavitation inception characteristics of V-ball valves, cavitation inception must be quantified. Modified Thoma cavitation number [18] discussed in chapter 2.2 was used as the quantification criterion. As the Reynolds number increases, the cavitation number decreases until cavitation inception is reached. All the valves were studied and a table of inception cavitation number against opening was obtained for each valve.

Table 4-4 shows the inception cavitation number for different openings of a 1 inch 30V standard port valve.

Opening	Inception $Re_D (\times 10^3)$	σ_i	Error	Error (%)
100	54	5.00	0.436	8.72
90	49	4.09	0.160	3.92
80	38	3.35	0.0914	2.72
70	26	2.94	0.072	2.45
60	22	2.56	0.079	3.10
50	15	2.26	0.062	2.73
40	10	1.96	0.038	1.92

Table 4-4 Inception cavitation number for 1 in. 30V standard port valve for various openings

From table above, there seems to be a trend in decreasing cavitation number as valve opening decreases meaning that higher pressure drops can be achieved with no cavitation in smaller openings. Also as the Reynolds number is calculated using the diameter of the pipe, it directly corresponds to the flow rate. In the second column of table 4-4, Reynolds

number at inception is shown. As the inception pipe Reynolds number decreases with decreasing opening, it is concluded that less flow rate can pass through smaller opening without cavitation. This is probably due to higher local Reynolds numbers at smaller openings.

Figure 4-37 to 4-39 show the changes in inception cavitation number vs. opening for different apex angle valves of a given size. There is an overall trend of reducing cavitation number with reduction in opening for a given geometry. Inception cavitation number is generally lower for smaller V apex angles, however some deviations from these trends are observed.

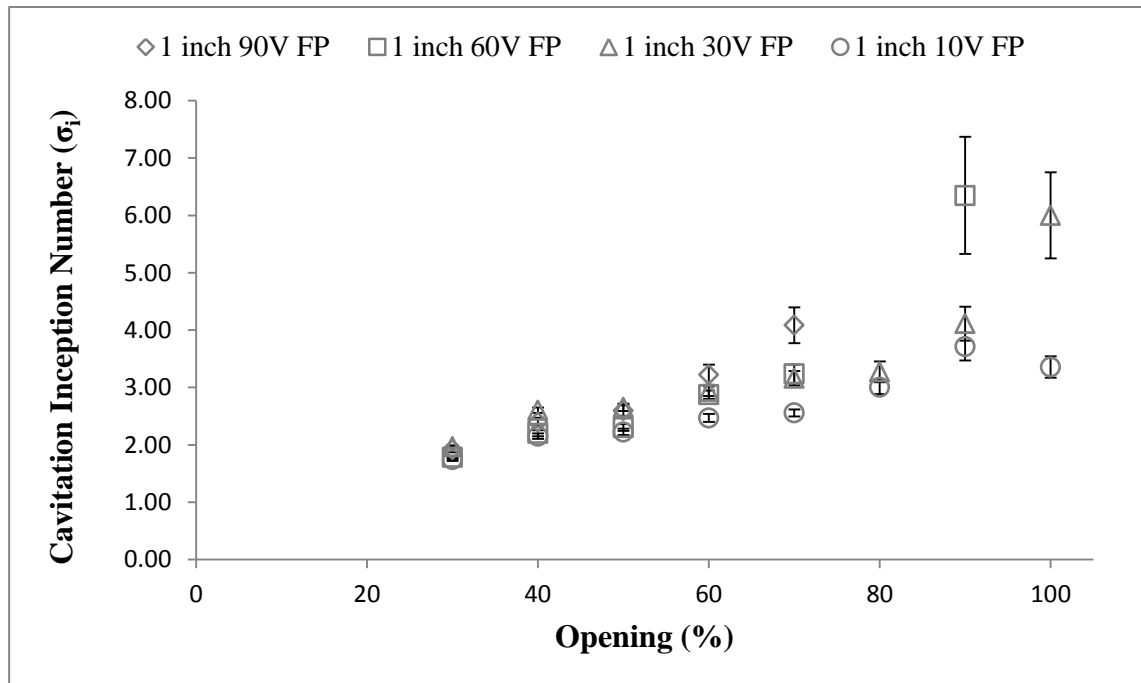


Figure 4-37 Inception cavitation number vs. opening for 1 inch full port valves

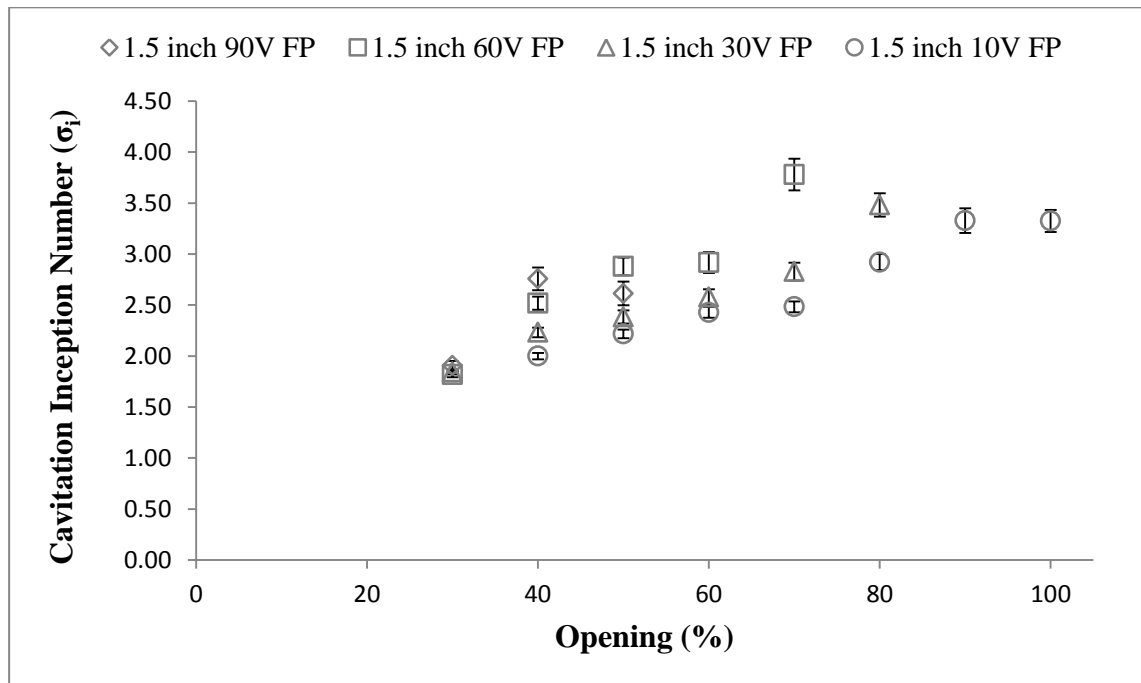


Figure 4-38 Inception cavitation number vs. opening for 1.5 inch full port valves

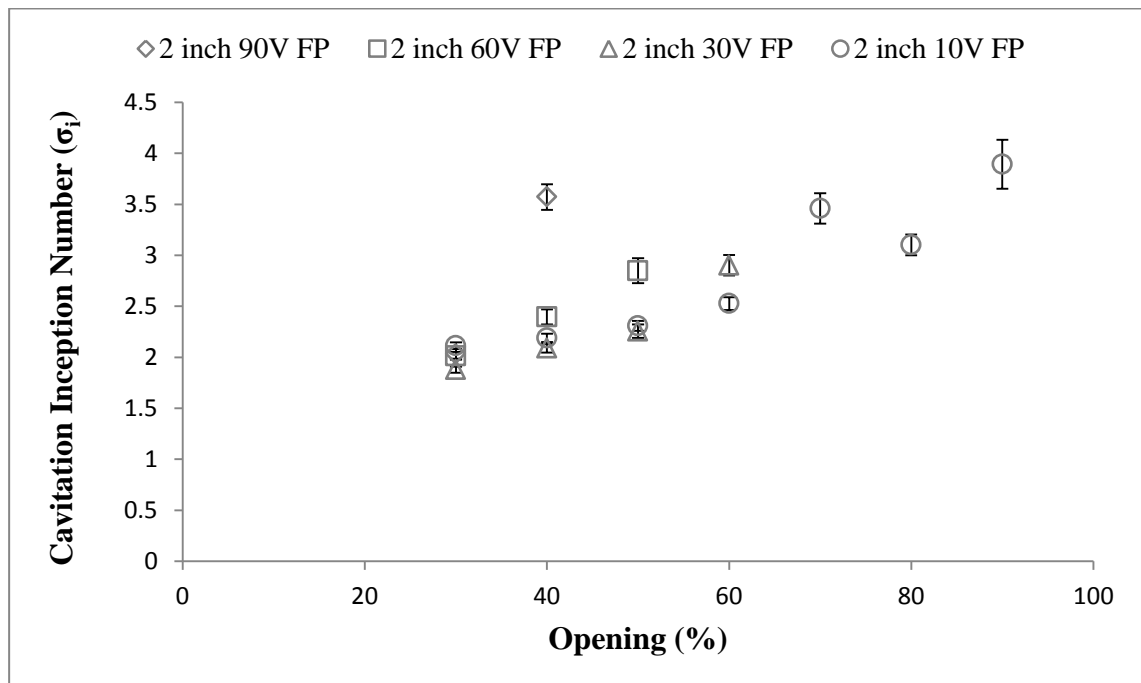


Figure 4-39 Inception cavitation number vs. opening for 2 inch full port valves

Here no specific correlation can be obtained between cavitation inception numbers of different apex angles at a certain opening. However, the general trend is reduction in inception cavitation number as opening decreases.

Figures 4-40 to 4-43 show the comparison of inception cavitation number with opening for a given apex angle for different sizes. Using these data, it is possible to investigate scalability of cavitation inception in V-ball valves. Full port valves of different sizes of a given geometry (apex angle) are linearly scaled up unlike standard port valves which have different flanges attached which causes the geometry to differ from one size to the other. Therefore the presentation of results is only limited to full port valves.

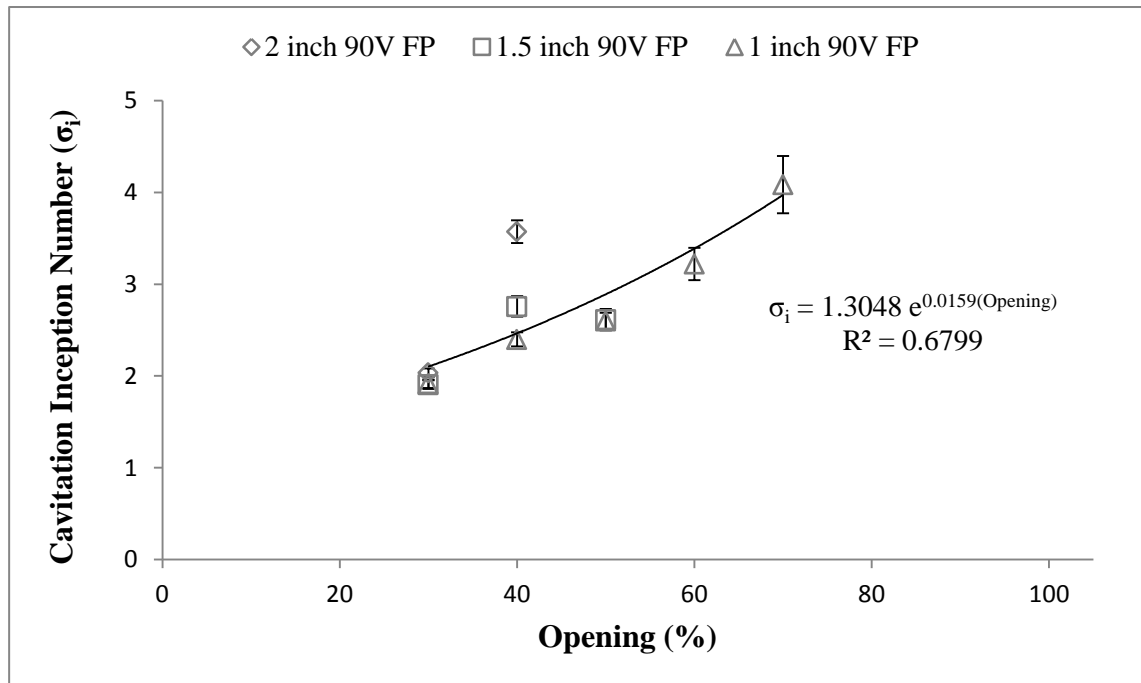


Figure 4-40 Comparison of inception cavitation number vs. opening for three different sizes of full port 90V valves

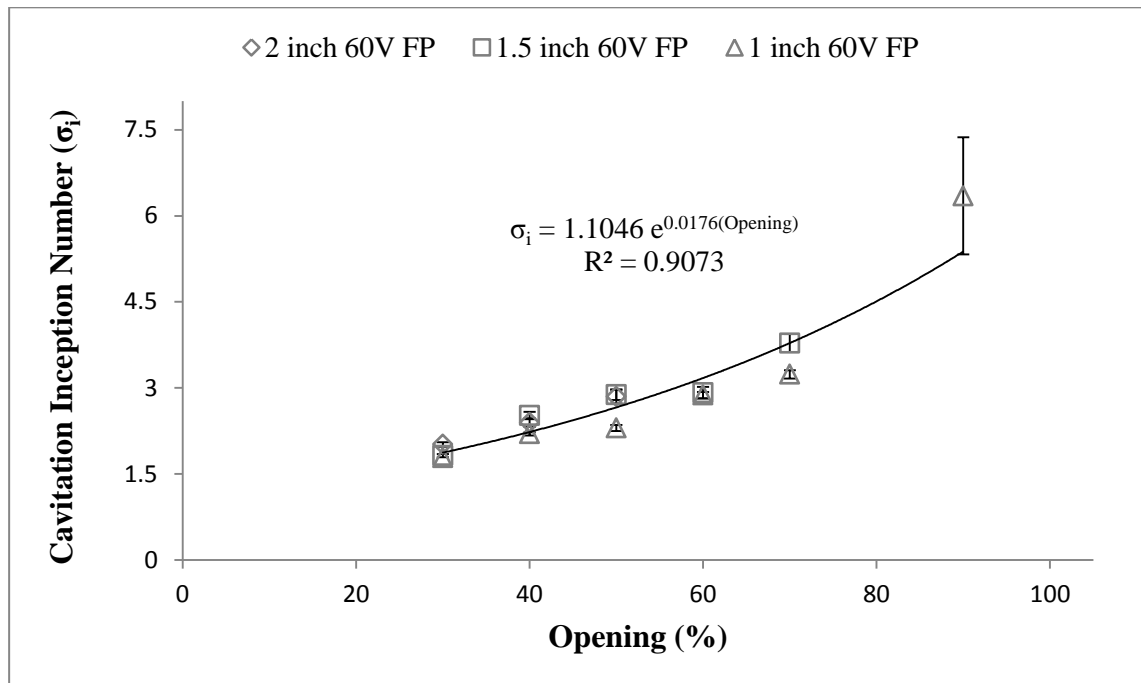


Figure 4-41 Comparison of inception cavitation number vs. opening for three different sizes of full port 60V valves

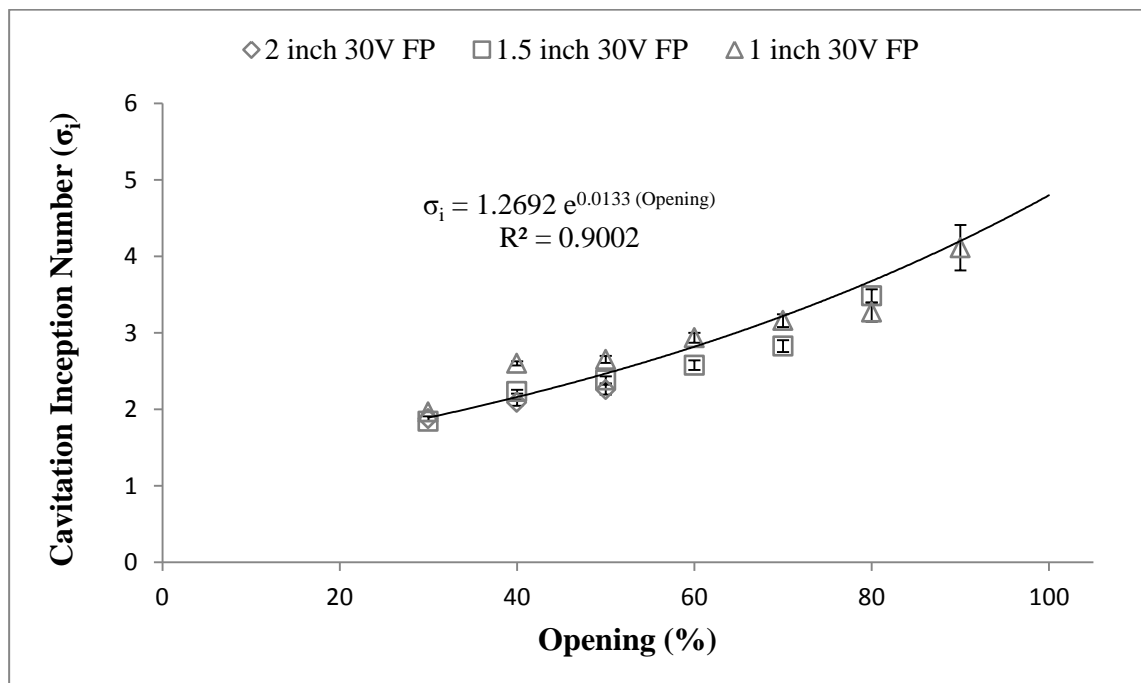


Figure 4-42 Comparison of inception cavitation number vs. opening for three different sizes of full port 30V valves

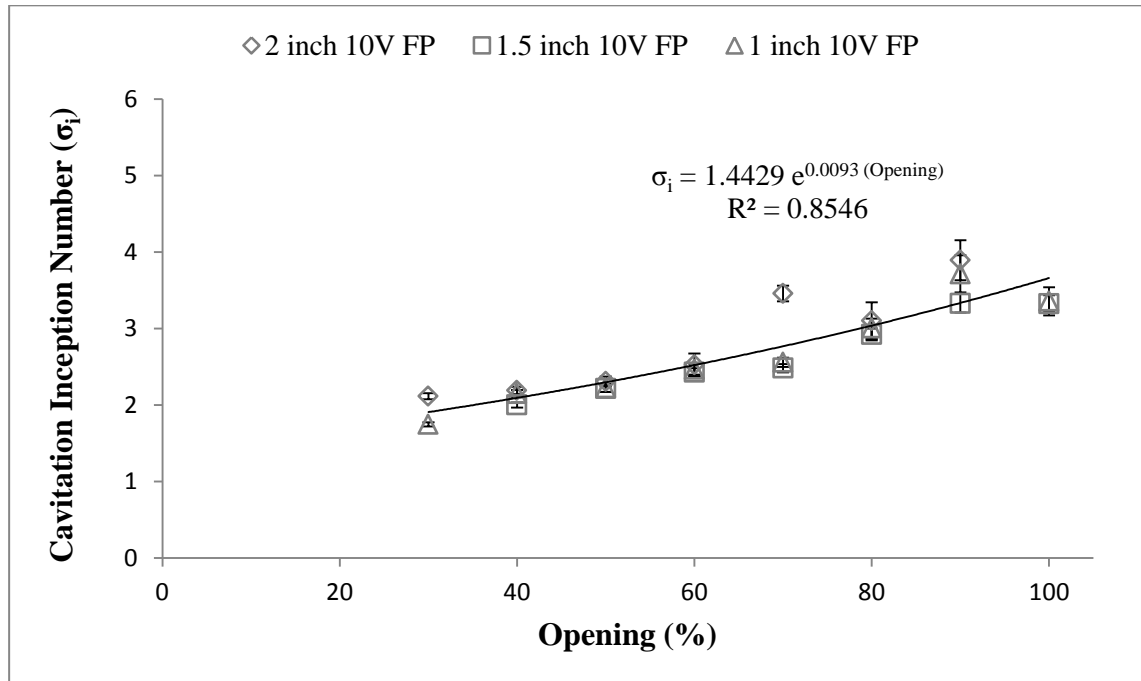


Figure 4-43 Comparison of inception cavitation number vs. opening for three different sizes of full port 10V valves

From Figures 4-40 to 4-43, a trend can be observed where inception cavitation number decreases as valve opening decreases for a given apex angle. Also in most cases, the cavitation inception number for each opening is approximately the same for a given geometry or deviates slightly. However, some deviations from this trend can be observed such as 2 inch 10V FP valves at 70% opening or 90V FP valves at 40%.

Table 4-5 shows the correlations for predicting inception cavitation number for different geometries (apex angles). The opening in these correlations are in percentage (e.g. for fully open valve the opening is 100). The opening range was obtained by considering the positions at which cavitation inception was detected. If cavitation did not occur in any of the sizes of a given geometry at a certain opening, then that certain position is considered out of the range of the correlation.

Valve Geometry	Correlation	Opening Range	Max. Difference
10V	$\sigma_i = 1.4429 \times e^{0.0093 \times \text{Opening}}$	$30 \leq \text{Opening}$	14.4 %
30 V	$\sigma_i = 1.2692 \times e^{0.0133 \times \text{Opening}}$	$30 \leq \text{Opening} \leq 90$	13.9 %
60V	$\sigma_i = 1.1046 \times e^{0.0176 \times \text{Opening}}$	$30 \leq \text{Opening} \leq 90$	17.0 %
90V	$\sigma_i = 1.3048 \times e^{0.0159 \times \text{Opening}}$	$30 \leq \text{Opening} \leq 70$	31.0 %

Table 4-5 Cavitation inception number vs. opening correlation for different apex angles

Although the maximum errors of these correlations is relatively high, they provide an engineering tool for designing and estimating whether the valve will undergo cavitation or not. Also 90V seems to have a high maximum difference. This is due to the data obtained at 40% open positions which do not follow the trend very well. The same was observed for 2 inch 10V FP valve at 70% opening.

To investigate the points which deviate from the trends, the upstream static pressure fluctuations were obtained and the standard deviation was compared for different range of Reynolds numbers. Figure 4-44 shows the standard deviation of upstream pressure fluctuations of a 10V FP valve operating at 70% open. To investigate the increase in standard deviation of pressure fluctuations in 2 inch valves, average of standard deviations of pressure fluctuations at different Reynolds numbers were plotted for different openings of different sizes in figure 4-45.

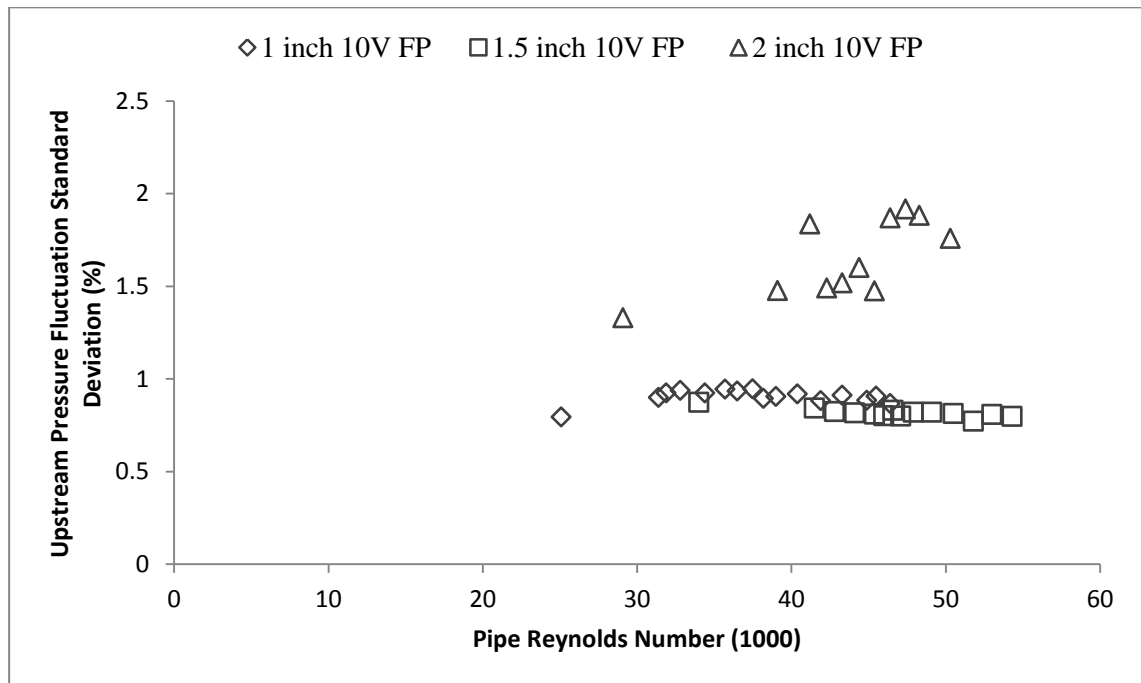


Figure 4-44 Standard deviation of pressure fluctuations for different 10V FP valves

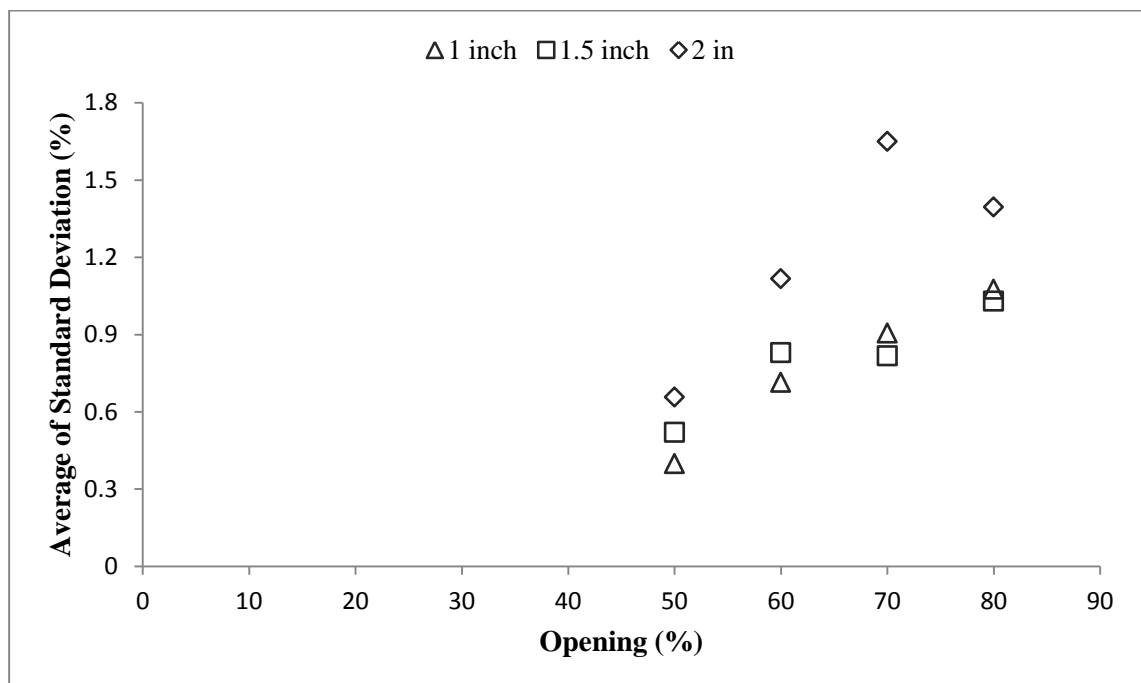


Figure 4-45 Variation of average of standard deviations for different openings

Figure 4-45 suggests that the 2 inch valve has a higher pressure fluctuation in general. However, there is a trend in pressure fluctuations and opening of each size. It can be observed in this figure that 2 inch 10V FP has the highest pressure fluctuations and does not follow the trend and therefore undergoes cavitation inception at an earlier stage. This indicates that a flow pattern change is causing increased pressure fluctuations. The reason behind these higher fluctuations is not known. It is very likely that in this specific geometry, an unsteady flow phenomena occurs, although to establish this, flow visualisation studies must be performed which are out of the scope of this thesis here. A further discussion on pressure fluctuation caused by the valves is presented in appendix E.

Two explanations can be given for this earlier cavitation inception in 10V FP valve at 70% opening. If the pressure fluctuations are caused in the jet at the outlet, then according to the studies of Ooi [20], pressure fluctuations are the cause of earlier cavitation onset. However if pressure fluctuations are caused by a change in flow pattern and introduction of unsteady flow phenomena, the earlier inception is perhaps due to a change in vortices. If the pressure fluctuations become greater compared to the average pressure, the existence of stronger unsteady flow phenomena can be speculated as a result of change in the geometry. These pressure fluctuations can cause earlier cavitation onset in a system. The existence of the vortices in the flow field itself is a cause of cavitation as studied by O'Hern [21]. If these vortices are becoming larger or are having stronger circulation then cavitation inception could occur earlier.

The scalability of cavitation in full port valves shows that Reynolds number has no or small effect on cavitation inception. Results obtained by Ooi [20] shows that for jet sizes

of 3.17 mm (0.125 inch) and 4.76 mm (0.1875 inch) diameter, the cavitation inception number does not change significantly between the two sizes. This is in good agreement with the results obtained in cavitation inception in valves here.

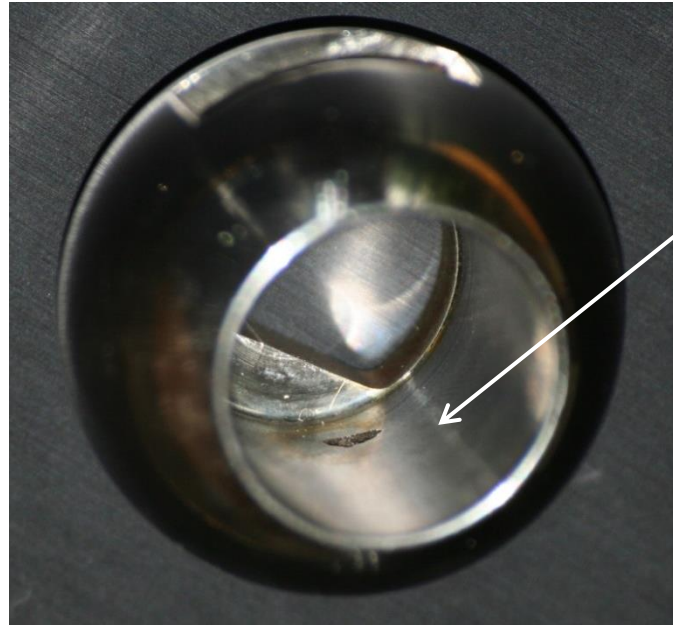
In conclusion, it is outlined that using cavitation number for cavitation inception scalability is an acceptable engineering tool. In a few cases the flow pattern effects become more dominant and cause deviations from the trend. Different correlations were investigated and it was observed that an exponential trend best describes the trend between cavitation number and opening for all sizes. This correlation provides a useful design tool for the industry.

4.3. Cavitation Damage

It is well known that cavitation causes damage to the hydraulic equipment. One of the accepted and validated reasons given for this damage is high velocity jets formed as a result of sudden bubble collapse [9, 10]. Although this study is not concerned with modelling or predicting damage caused by cavitation but due to the damage to one of the ball valves, it is still being reported here.

The 1 inch 60V standard port valve was used for obtaining preliminary data and validation of the experimental techniques and operated under cavitating conditions. Although this valve was not used under cavitating conditions with audible noise at all times, but occasionally high pressure drops (50 to 80 psi) were applied. Apparently this was just enough to cause pitting and damage the 30V ball. This did not occur with the other valves which were tested only for a day.

From Figure 4-46, the location of the pitting damage is very close to the V shape inlet of the ball valve. It can be speculated that bubble formation occurred at the inlet and it collapsed after the step of the V.



Pitting caused by cavitation, the location is on the bottom side of the ball and right after the step of the V opening

Figure 4-46 Pitting damage caused by cavitation inside of a 1 inch standard port 60V valve (Diameter of the bore = 0.75 in)

4.4. Summary

In this section, the method of cavitation detection was described and cavitation inception number was found for different apex angles and sizes of V-balls. Also, correlations were developed for cavitation inception vs. opening for different apex angles of full port valves. Using these correlations, application engineers can compare their plant cavitation numbers vs. desired valves cavitation number and select the valve which does not cavitate by referring to the plots. This will ensure that the valves will be operational longer and reduce the costs by increasing the life span of a valve.

5. Numerical Investigations

5.1. Numerical Study Methodology

Here a numerical approach is used to develop a prediction methodology for flow coefficient and onset of cavitation using commercial CFD software. The procedures are described and the results are discussed.

5.1.1 The Model

The model consists of a 1 inch 60V ball valve and 5 diameters of piping upstream and 8 diameters of piping downstream. Three openings of 100%, 70% and 50% open were modelled and meshed. The model was originally developed in SolidWorks and was imported into ANSYS ICEM CFD 14.0. The geometry was simplified without losing details of the ball valve and blocking technique was used to provide a structured grid. The model was divided into three sections; inlet pipe, outlet pipe and the V ball. Each part was meshed separately and then the 3 regions were merged and a conformal grid was obtained. The number of the nodes was dependent on the opening and the geometry. The 100%, 70% and 50% opening models had 0.5, 1.6 and 1.8 million nodes respectively. Grid independence was performed on the 50% open and 100% open by reducing the grid size by 33% (1.2 M nodes) and increasing the nodes from 0.5 million to 1.4 million respectively, to ensure the results were grid independence. Figure 5-1 to Figure 5-4 show the geometrical representation of 1 inch full port valve at 70% opening. The mesh details are provided in appendix F.

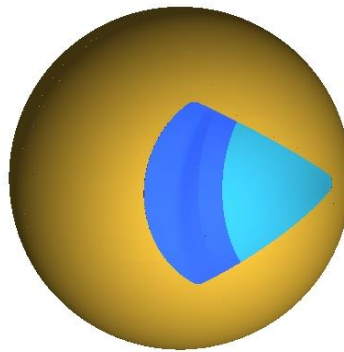


Figure 5-1 Graphical representation of 1 inch 60V full port valve at 70% Opening, The light blue is the effective opening

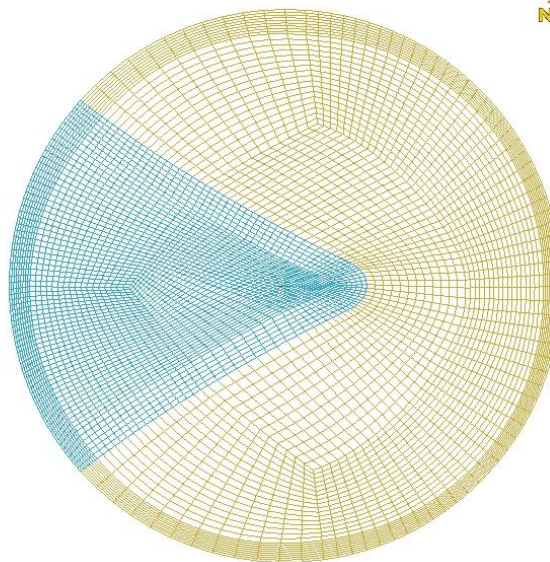


Figure 5-2 Inlet grid geometry, the yellow grid indicates wall and the blue mesh is inlet of the ball valve

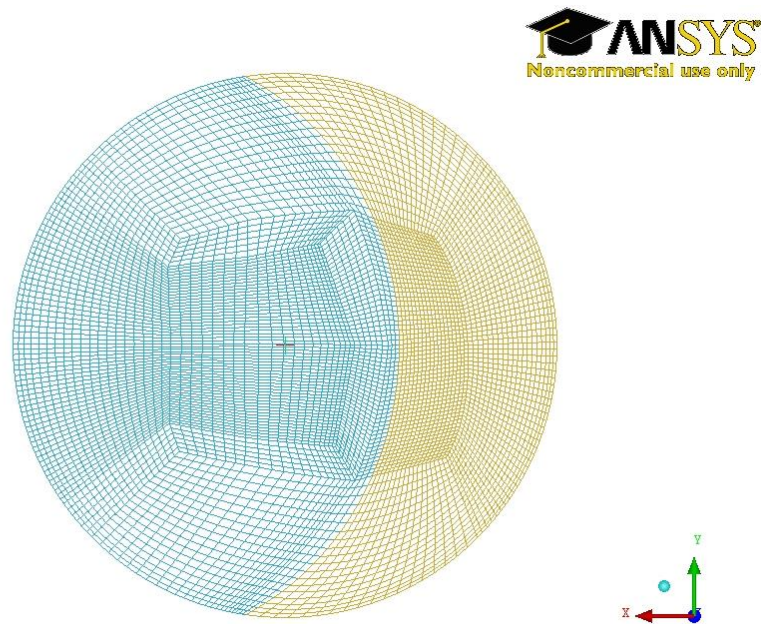


Figure 5-3 Outlet grid geometry, the yellow grid indicates wall and the blue mesh is outlet of the ball valve

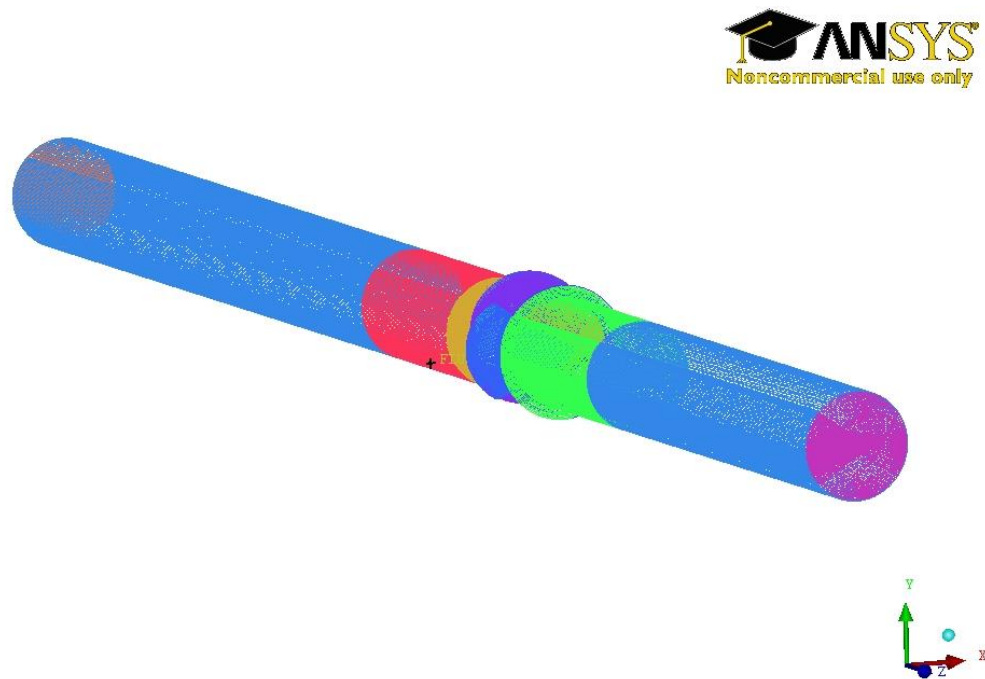


Figure 5-4 Computational domain of 1 inch 60V full port

5.1.2 Solution Method

The grid was imported into ANSYS Fluent. The boundary conditions were set. The solid walls had boundary condition of no slip walls with stainless steel as the material. The inlet velocity was specified as uniform and was set depending on the opening. However, since a velocity higher than 5 m/s were not achieved in the experiments, 5 m/s was the maximum value used in the simulations. Output gauge pressure was set to 1.015 psi (7 kPa) and the atmospheric pressure was set to 14.96 psi (1 atm). The interior nodes were set as fluid and liquid water at 20° C was chosen as the working fluid. To specify the turbulence input parameters the turbulent length scale and turbulence intensity was chosen. The turbulence length scale was calculated as [51]:

$$L_t = 0.07 D_h$$

where L_t is the turbulent length scale and D_h is the hydraulic diameter. The turbulent length scale is based on the maximum turbulent mixing length for a fully developed turbulent flow was determined to be as above. The turbulence intensity was calculated using [51]:

$$I_t = 0.16 \times Re^{-\frac{1}{8}}$$

Since the inlet velocity and the pipe diameter are known, the Reynolds number can be found and the two parameters can be determined.

The domain was initialised using inlet boundary conditions. Since the problem is a pressure-velocity coupling, the numerical scheme chosen for the solution was SIMPLEC

as it has better convergence in such flows. First, all simulations were run using standard discretization for pressure and first order “upwinding” for momentum and turbulent kinetic energy for SST k- ω and in the case of standard k- ϵ model the dissipation rate was also set to first order “upwinding”. The relaxation constants were 0.3 for pressure and 0.7 for momentum, turbulent kinetic energy and dissipation rate. After the residuals dropped to a value less than 1×10^{-4} , the momentum and turbulent kinetic energy and dissipation rate were then switched to second order “upwinding” and if the momentum residuals converged to a value less than 1×10^{-3} and the velocities and turbulent parameters converged to values less than 1×10^{-4} , the solution was considered converged and the results were imported into Microsoft Excel and Tecplot 360 for postprocessing.

5.1.3 Inlet Boundary Condition Justification

The inlet boundary condition used was uniform flow inlet. From the experimental methodology, it is assumed that the flow enters the valve having a fully developed profile. To justify using this inlet boundary condition, the 1 inch 60V full port valve at 100% opening with inlet velocity of 5 m/s was remodelled to have 35 diameters development length and the results for flow coefficient were compared. The results showed that in this case, the resulting flow coefficients were only 2.9% different. This shows that using uniform flow inlet boundary condition does not affect the results substantially as the effects of the valve are much here. This was the worst case scenario as pressure drop in the pipe was playing a role in determining a value for flow coefficient.

To investigate the effects of flow development further, the velocity profile at 2 pipe diameters prior to the ball was plotted against the fully developed velocity profile as shown on figure 5-5. The fully developed profile was obtained by analysing the results of the same case when the upstream pipe was 35 diameters long. Although the velocity profiles are different close to the wall, they are quite similar in the bulk flow. Since the results are only affected by 3 % using uniform flow inlet to simulate the experimental results is justified.

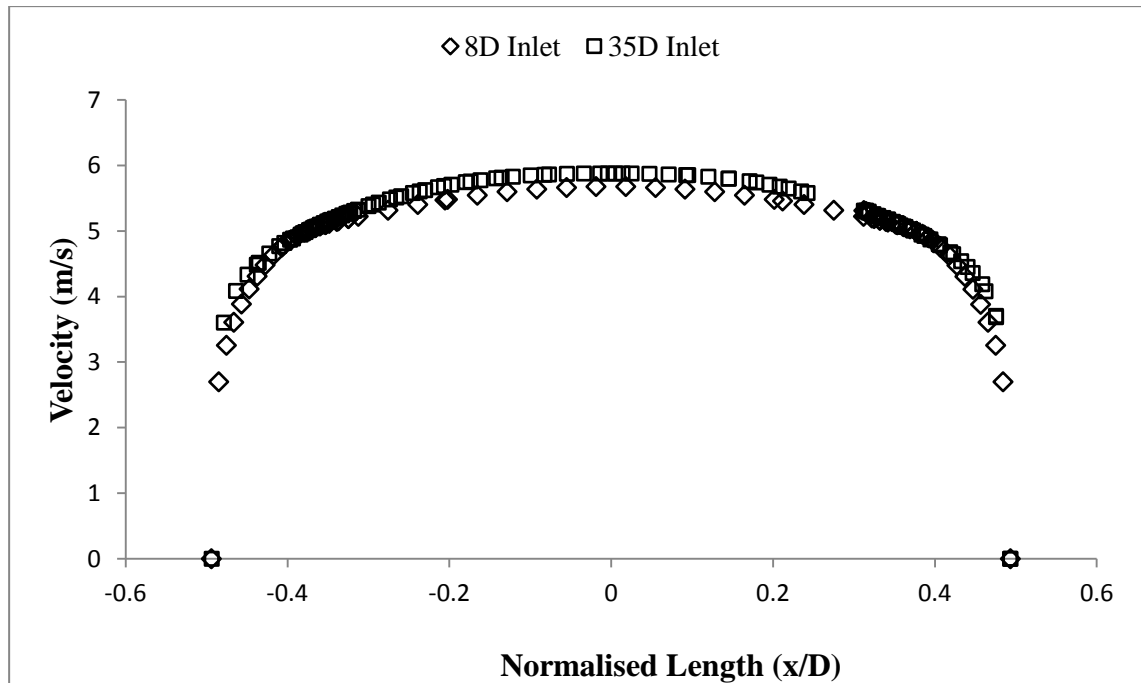


Figure 5-5 Comparison of velocity profile of 8D upstream pipe model at 2 diameters upstream of the valve vs. fully developed velocity profile (35D velocity profile)

5.1.4 The Turbulence Models

Since the flows are turbulent, choosing the most appropriate model is the most important aspect of the numerical investigations. Also the models used must be cost effective in

terms of computational time and resources for the industry, widely used and numerically stable. Two equation turbulence models are therefore the best turbulence models to be evaluated. Menter et al [52] have provided a comprehensive review of two equation eddy viscosity turbulence models and has successfully shown that standard $k-\epsilon$ model, which is the most robust and widely used in the industry, is successful in capturing turbulence details in free shear flows and the wakes where $k-\omega$ is more successful in capturing adverse pressure gradients and flow separation and has therefore combined the two models to introduce SST $k-\omega$ which was shown to be superior to the original $k-\omega$ developed by Wilcox [53]. Consequently standard $k-\epsilon$ and SST $k-\omega$ were the chosen models for cavitation and flow coefficient numerical studies.

5.1.5 Grid Independence Study

The grid dependence was investigated in 50% and 100% open models. In the 50% open case; the grid was coarsened in streamwise and spanwise direction to reduce the number of nodes from 1.8M to 1.2 M. In the case of 100% opening, the grid was refined in spanwise and streamwise directions to increase the number of nodes from 0.5 M to 1.4 M nodes. Figure 5-6 shows the pressure drop predicted by standard $k-\epsilon$ using two different grids with different mesh densities.

The difference between the predicted flow coefficients calculated for 50% opening was less than 1% and for the 100% opening case the difference between the obtained flow coefficients was 1.6%. This is an acceptable grid dependency and therefore the original grid sizes used were sufficient. However, the local minimum pressures were predicted

with 5% difference in the two simulations. As local minimum pressures occur within small regions, the mesh density becomes important in capturing these small regions.

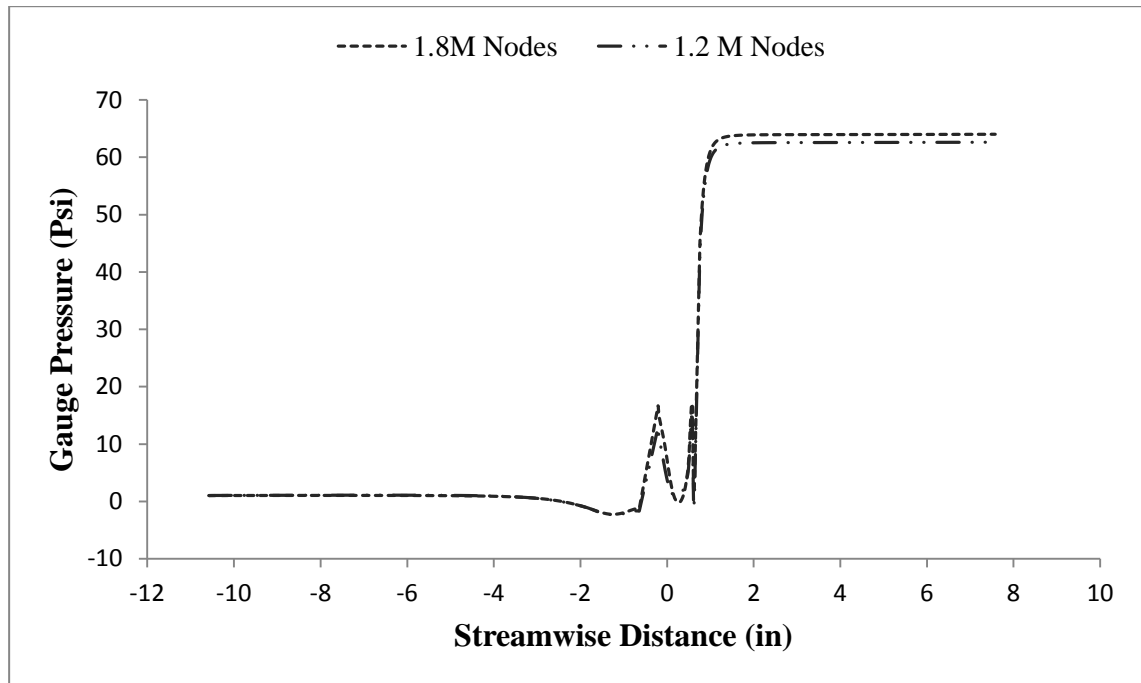


Figure 5-6 Comparison of pressure drop prediction of different grid size for 50% open valve at $Re = 63000$ using standard $k-\epsilon$

5.2. Numerical Results

5.2.1 Flow Coefficient Determination

To obtain a value for flow coefficient, the static pressure at 2D upstream and 6D downstream at the wall was found using Microsoft Excel for each case for different Reynolds numbers. At least four different inlet velocities corresponding to four different Reynolds number were simulated and plotted. Figures 5-7 and 5-8 show the predicted pressure drop for different Reynolds number for a valve at 50% opening.

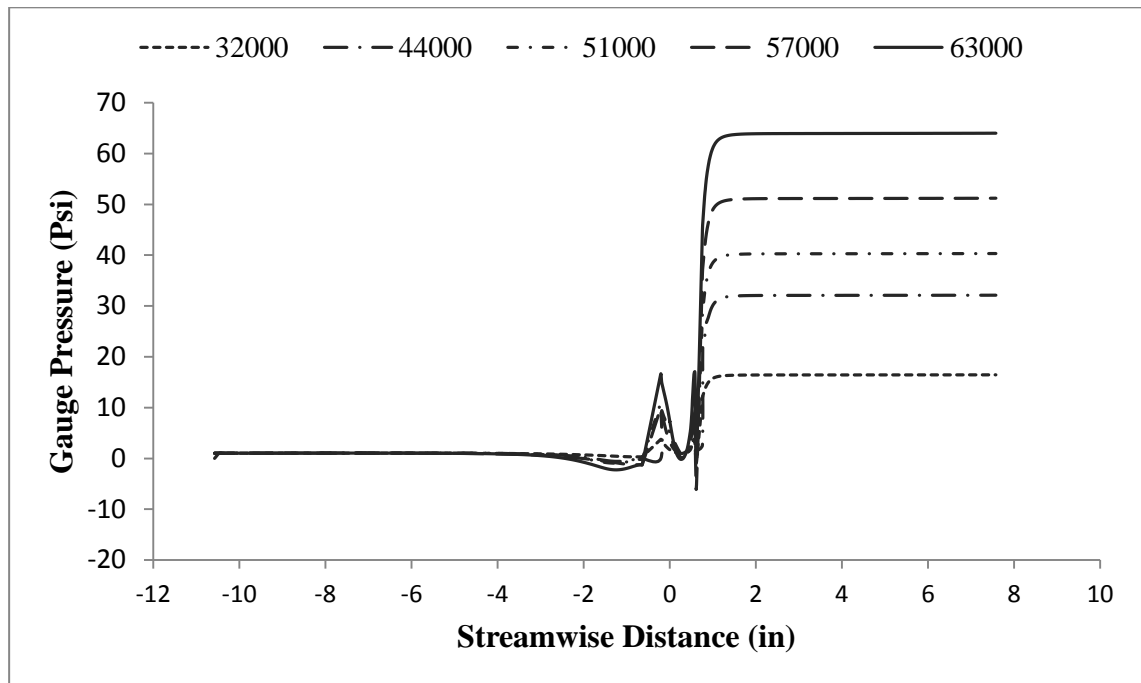


Figure 5-7 Comparison of pressure drop predicted by standard $k-\epsilon$ for various pipe Reynolds numbers for 1 inch 60V Full port at 50% opening

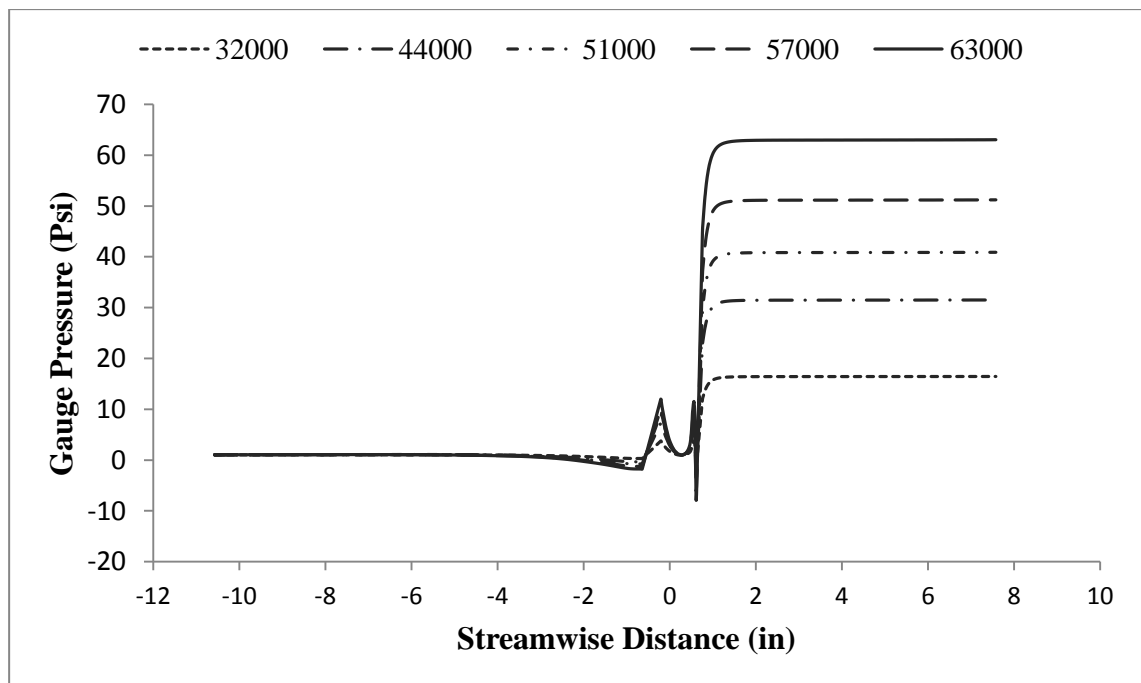


Figure 5-8 Comparison of pressure drop predicted by SST $k-\omega$ for various pipe Reynolds numbers for 1 inch 60V Full port at 50% opening

Figures 5-9 to 5-11 show the predicted pressure drop of SST k- ω and standard k- ϵ against the experimental data. The predictions of the two models are nearly the same. From these figures it can be observed that pressure drop is predicted best in 100% and 70% opening cases.

The flow coefficient and cavitation number were calculated using:

$$C_v = Q \sqrt{\frac{\rho / \rho_0}{\Delta P}}$$

$$\sigma_i = \frac{P_1 - P_v}{0.5 \rho u^2}$$

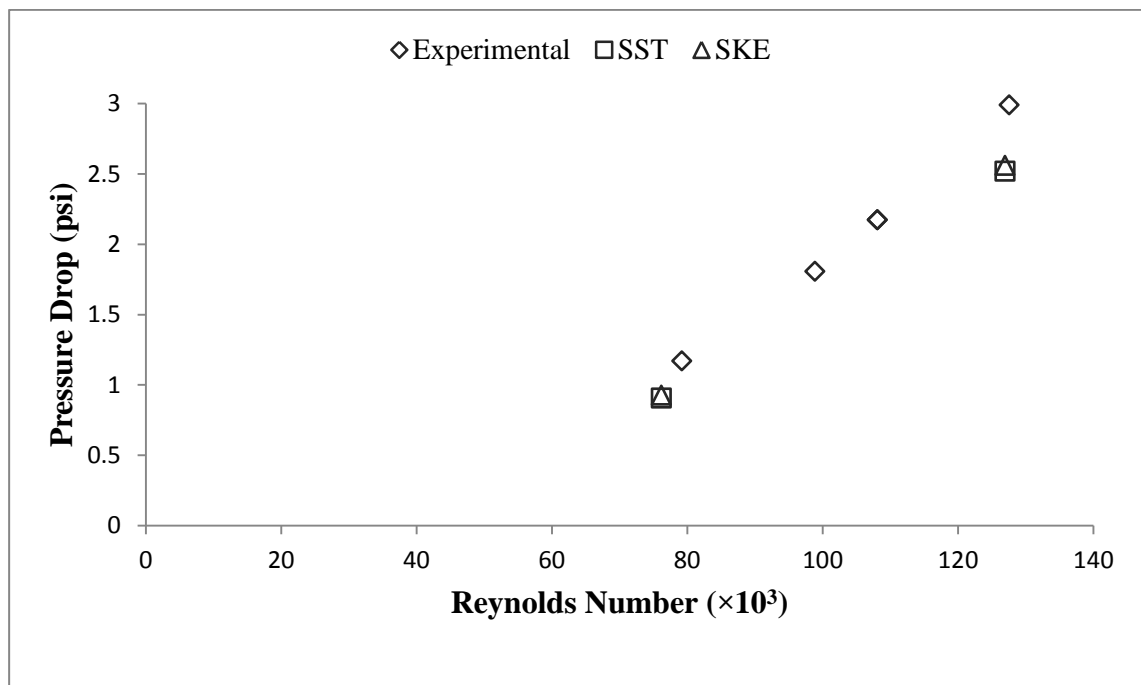


Figure 5-9 Comparison of numerical predictions of pressure drop vs. experimental results for 1inch 60V Full port valve at 100% opening

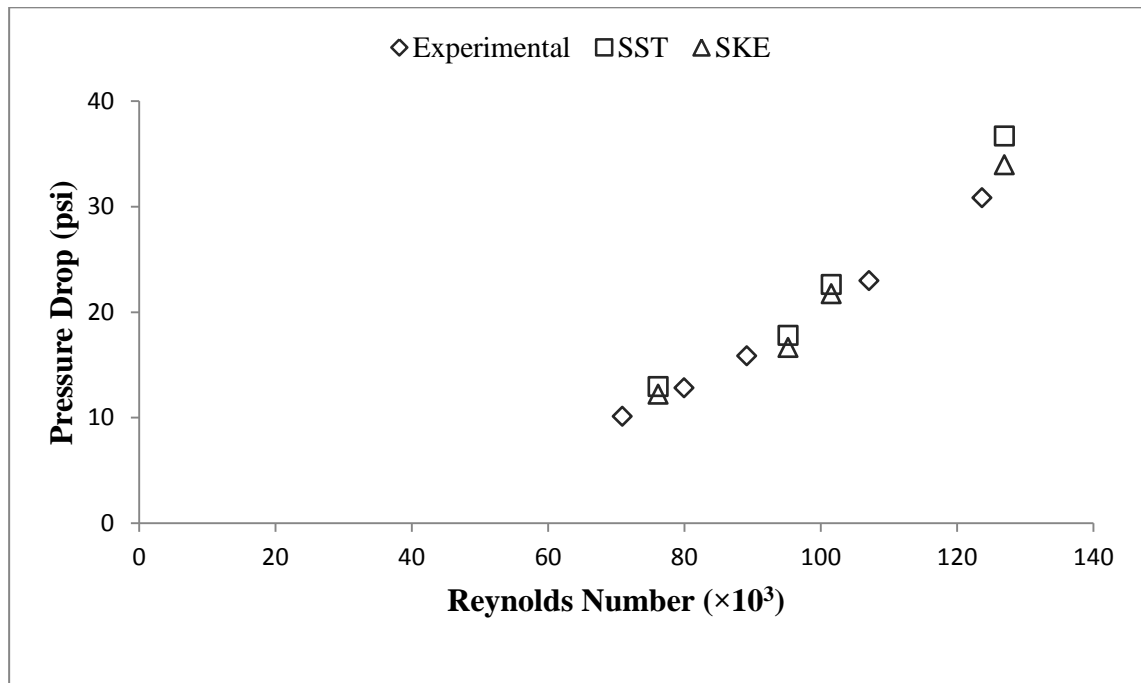


Figure 5-10 Comparison of numerical predictions of pressure drop vs. experimental results for 1inch 60V Full port valve at 70% opening

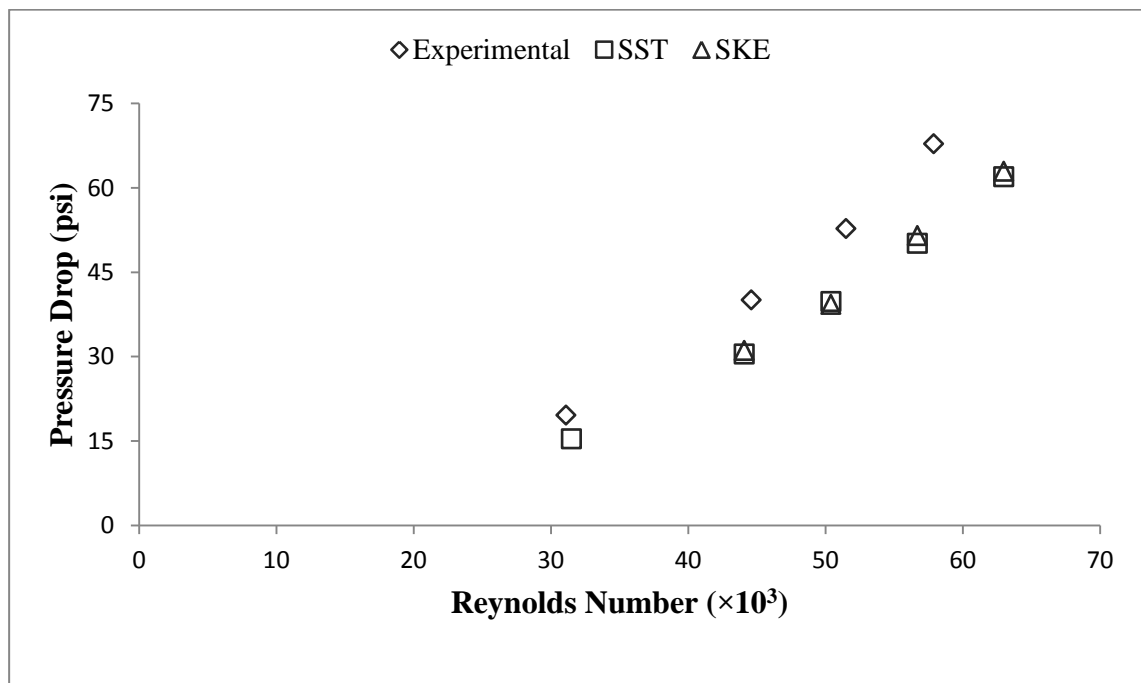


Figure 5-11 Comparison of numerical predictions of pressure drop vs. experimental results for 1inch 60V Full port valve at 50% opening

The flow coefficient values were then averaged and plotted against the experimental data as shown in figure 5-12. An improvement in CFD predictions is observed when ANSYS FLUENT is used. The values obtained from SST k- ω and standard k- ϵ are very close and differ by less than 3%. The discrepancy between SST k- ω and standard k- ϵ CFD predictions and experimental data is also less 20% and therefore both models are suitable for pressure drop modelling in ball valves.

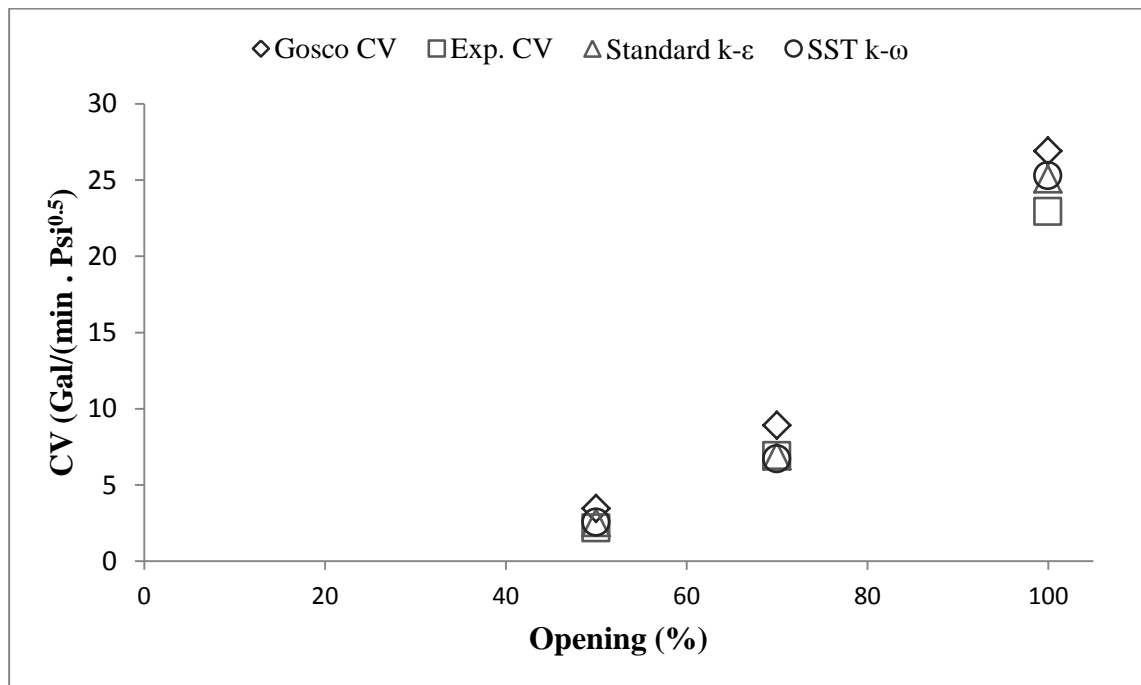


Figure 5-12 Comparison of CFD predictions of SST k- ω , standard k- ϵ and Gosco CFD and the experimental data for three different openings

The CFD performed by Gosco however was conducted using Solid Works Flow Simulator. This software provides automated cut cell meshing and uses only one turbulence model which is based on standard k- ϵ with modified constants. Table 5-1 shows the constants of k- ϵ turbulence model. Table 5-2 shows the different values used

for constants in the standard k- ϵ model and the Lam-Bremhorst k- ϵ [54] used by SolidWorks.

$C_{1\epsilon}$	$C_{2\epsilon}$	C_μ	σ_k	σ_ϵ
$1.44f_1$	$1.92 f_1$	$0.09 f_\mu$	1.0	1.3

Table 5-1 Constants of k- ϵ turbulence model

CFD Software	k- ϵ constants used		
	f_μ	f_1	f_2
ANSYS FLUENT	1.0	1.0	1.0
SolidWorks	$[1 - \exp(-0.0165Re_y)]^2 \left(1 + \frac{20.5}{Re_t}\right)$	$1 + \left(\frac{0.05}{f_\mu}\right)^3$	$1 - \exp(-Re_t^2)$

Table 5-2 Comparison of ANSYS FLUENT standard k- ϵ constant with SolidWorks k- ϵ constants

Lam-Bremhorst k- ϵ model has some additional terms which are defined as:

$$Re_y = \frac{k^2}{\nu \epsilon}$$

$$Re_t = \frac{k^{\frac{1}{2}} y_{min}}{\nu}$$

where k is turbulent kinetic energy, ϵ is the dissipation rate, ν is the velocity and y_{min} is the shortest distance to the nearest wall. Since Lam-Bremhorst developed these constants

for low Reynolds number applications, it can be concluded that the meshing technique and the CFD solution method has caused the simulations of Gosco Valves to deviate from the experimental results more than standard $k-\epsilon$.

5.2.2 Cavitation Detection Determination

The cavitation detection technique was based on the experimental work performed by Belahadji et al. [24]. They observed that at cavitation inception, the turbulent structures do not change compared to the single phase flow. As a result, performing single phase flow numerical simulations and defining cavitation onset at the point where the local minimum pressures reach vapour pressure is justified as the turbulent structures at these low negative pressures do not change significantly. To identify cavitation inception, local minimum pressures for different velocities at two different openings were compared against cavitation number calculated using:

$$\frac{P_{abs} - P_v}{\Delta P}$$

Figure 5-13 and Figure 5-14 show the predictions of local minimum pressure by each turbulence model for 70% and 50% open valves. A second order correlation between the local minimum pressure and cavitation number is developed and the critical cavitation number where local minimum pressure is zero was developed as shown on the figures and these results were then plotted against experimental results (Figure 5-15).

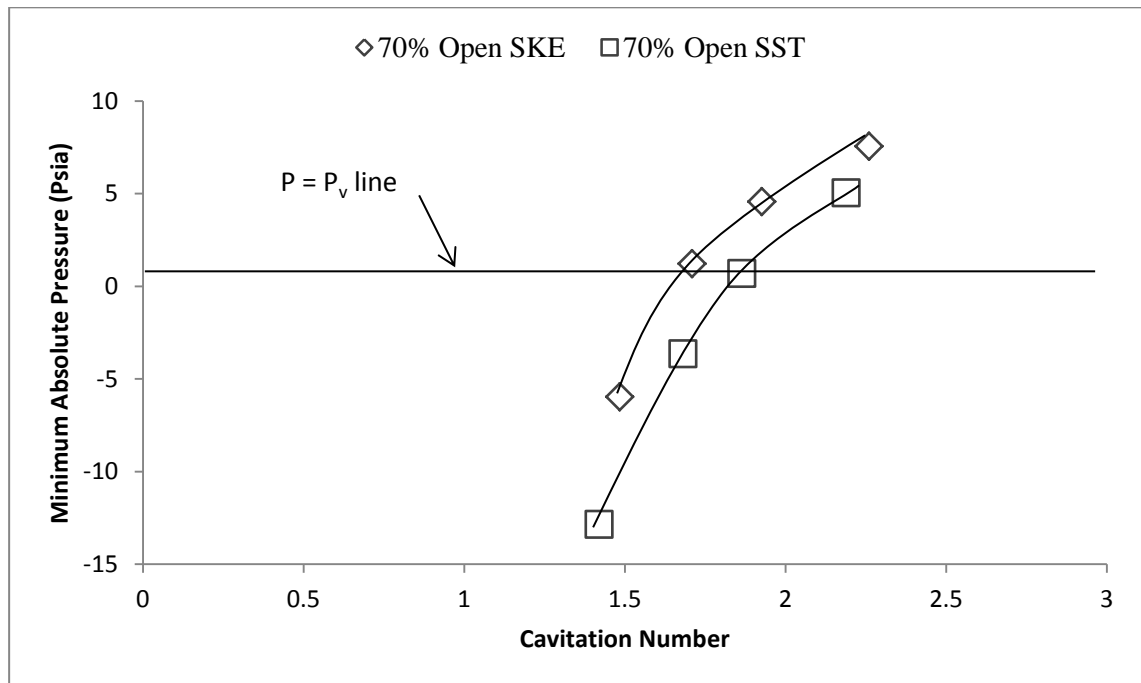


Figure 5-13 Minimum absolute pressure vs. cavitation number prediction of different turbulence models at 70% open

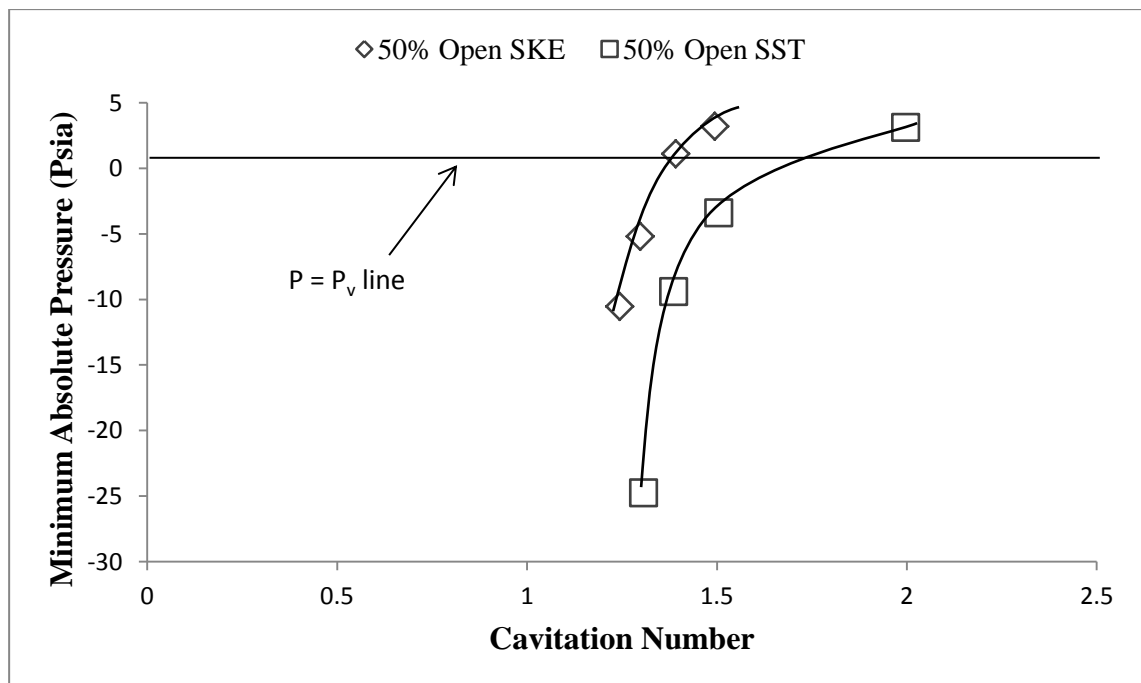


Figure 5-14 Minimum absolute pressure vs. cavitation number prediction of different turbulence models at 50% open

The minimum pressures obtained are not realistic as negative absolute pressures cannot be reached in reality. However the CFD code used does not have a cap on absolute pressures it calculates and therefore minimum absolute pressures can be achieved using CFD. Although it does not have realistic meaning, it provides a good cavitation detection technique because these negative absolute pressures can be plotted against cavitation number and when minimum local pressure reaches vapour pressure, cavitation is achieved as shown in figures above.

Figure 5-15 shows the comparison between experimental data and the CFD predictions for cavitation inception. The Experimental Cavitation Inception refers to the point where cavitation occurrence is first detected where the Experimental Developed Cavitation refers to the point where the rate of increase of energy is changed which is indicative of occurrence continuous established cavitation as shown on figure 5-16. This indicates that the pressure fluctuations are no longer causing the pressure drop resulting in cavitation and the mean properties of the flow are now the operating condition which causes cavitation.

Figure 5-16 suggests that at 100% opening, no cavitation was observed experimentally which is in agreement with the results obtained using CFD when maximum achieved velocity in experiments was used as boundary condition. The results of this study suggests that SST $k-\omega$ performs better than standard $k-\epsilon$ in predicting cavitation inception as shown by Figure 5-15 and since the flow coefficient prediction of the two models are very similar, it can be concluded that SST $k-\omega$ is a better model for conducting CFD studies in valves.

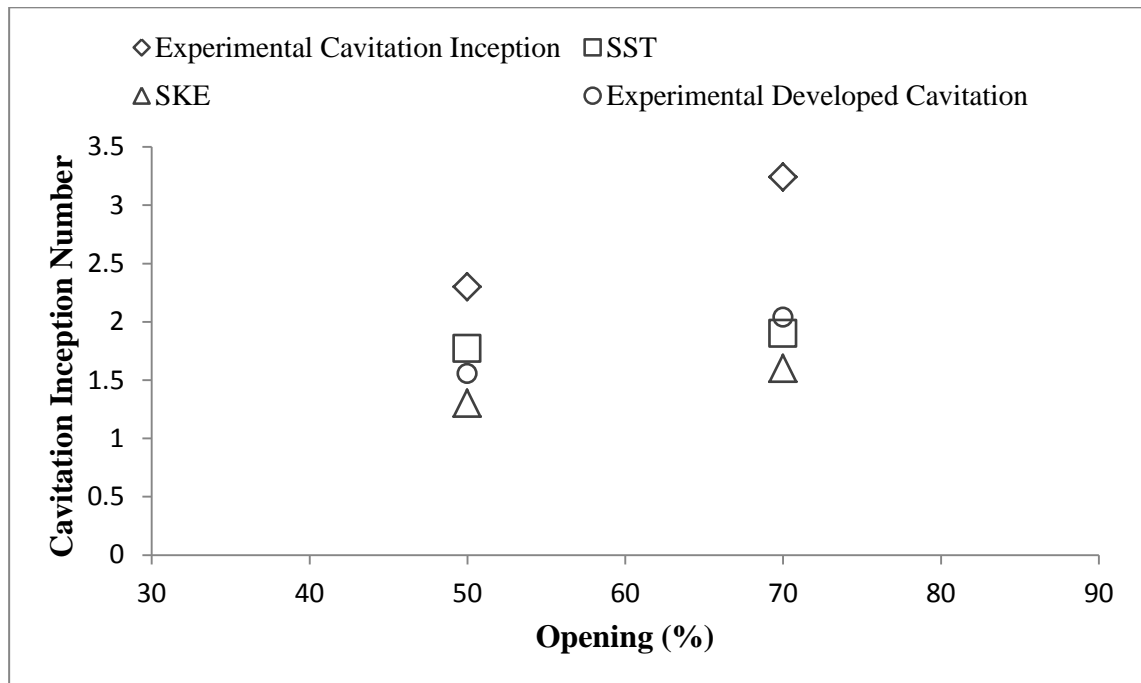


Figure 5-15 Comparison of cavitation inception prediction of different turbulence models vs. experimental data

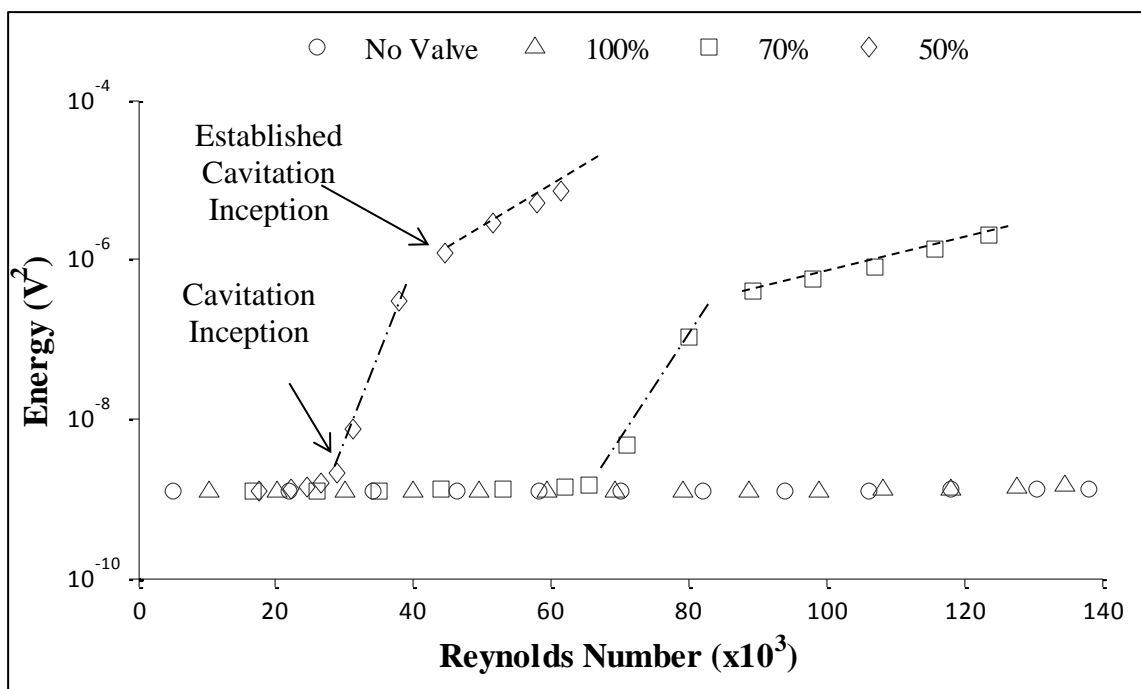


Figure 5-16 Downstream 2 to 5 kHz frequency range energy level for 1 inch 60V Full Port valve vs. no valve installed for various openings.

It can be concluded that as the turbulence models used are averaged, they predict the onset of developed cavitation to an acceptable accuracy. However prediction of intermittent cavitation inception is not a possibility using RANS turbulence models which is expected.

To understand cavitation inception, velocity and pressure contours were obtained as well as velocity vector fields. Figures 5-17 to 5-20 show the predicted pressure contours by the standard k- ϵ for 1 inch 60V full port valve at 70% opening with a pipe Reynolds number of 88,900 at various planes. These contours show the V inlet, inlet flange and the step after the V. The direction of the flow is from right to left.

The inlet pipe has the highest pressures and as the flow reaches the nozzle of the valve, the pressure begins to drop. The lowest pressures exist at the edges which cause the low minimum pressures. These regions are flow separation regions. It can be concluded that cavitation in the valves investigated is not due to effects of vena contracta but it is rather the effect of flow separation. This is in agreement with the experimental studies performed by Katz [19] which showed that flow separation is a cause of low pressures and cavitation inception.

Figures 5-21 to 5-24 show the velocity contours predicted by standard k- ϵ for 1 inch 60V full port valve at 70% opening. It is possible to see a high velocity stream at the core of the V (vena contracta) which has small recirculation zones near the walls of the V.

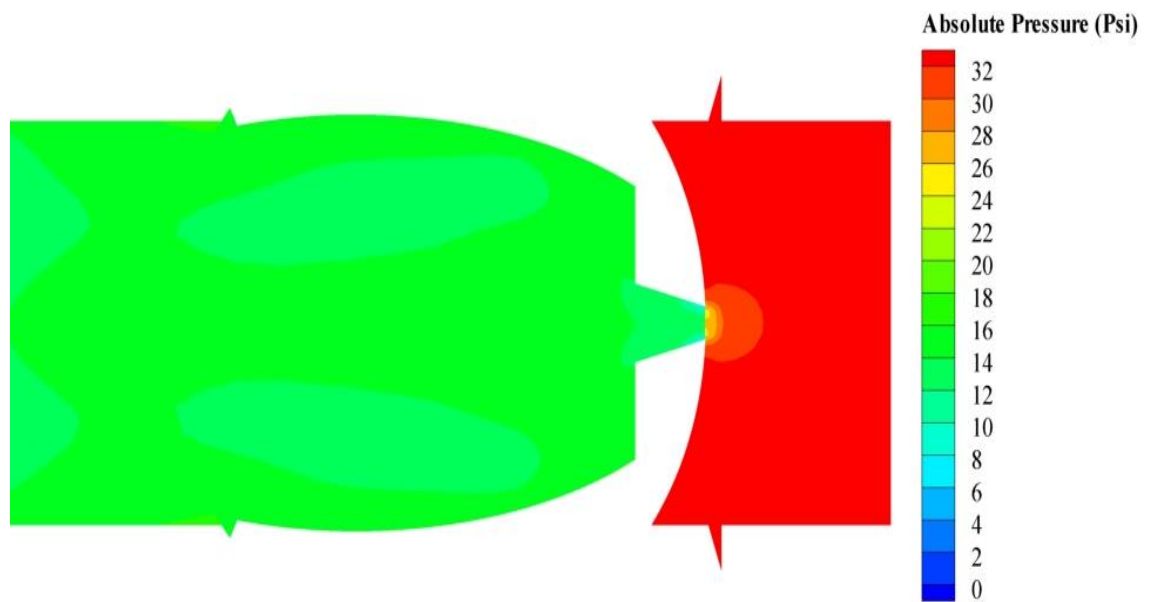


Figure 5-17 Pressure contours predicted by standard k- ϵ for 1 inch 60V FP valve at 70% opening, $Re = 88,900$ near the apex

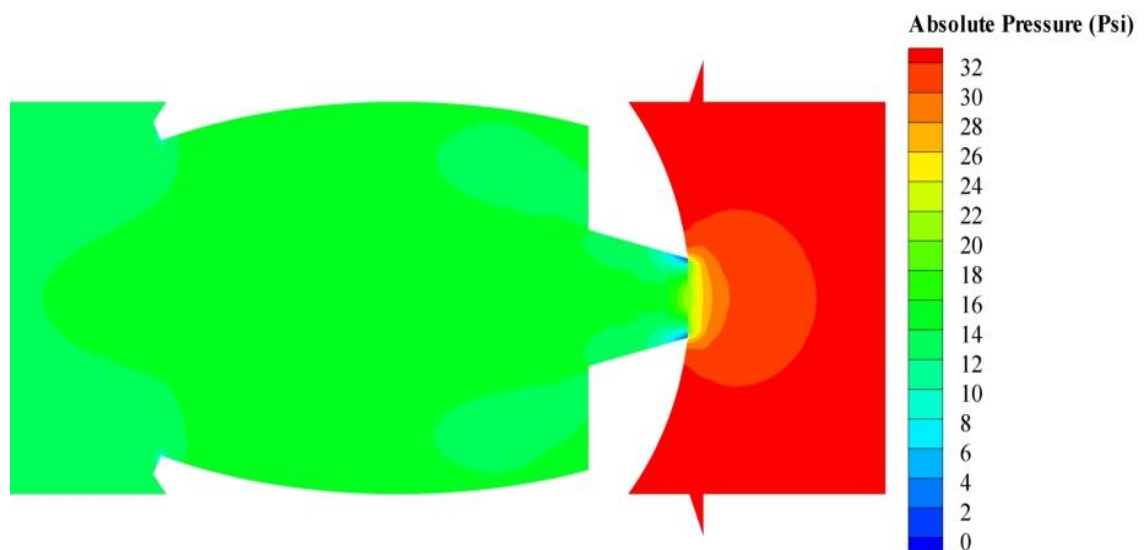


Figure 5-18 Pressure contours predicted by standard k- ϵ for 1 inch 60V FP valve at 70% opening, $Re = 88,900$ in the middle of the pipe

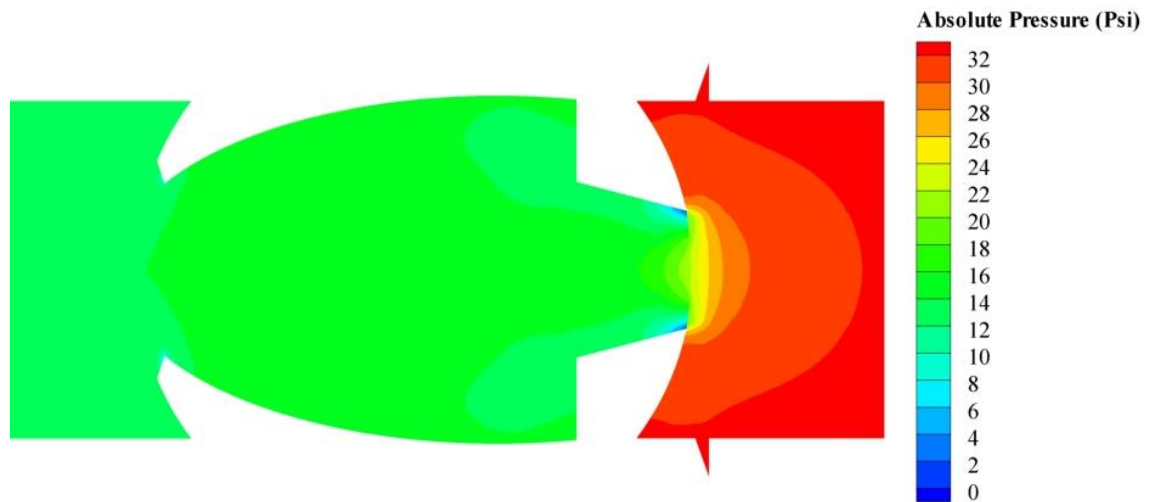


Figure 5-19 Pressure contours predicted by standard k- ϵ for 1 inch 60V FP valve at 70% opening, $Re = 88,900$ near the base of the V

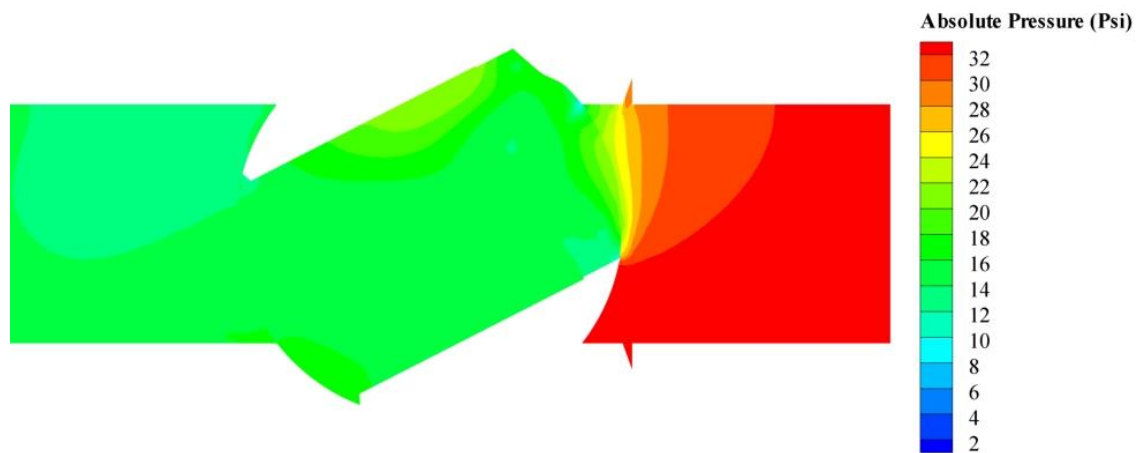


Figure 5-20 Top view of the pressure contours predicted by standard k- ϵ for 1 inch 60V FP valve at 70% opening. The cut plane is the symmetry plane

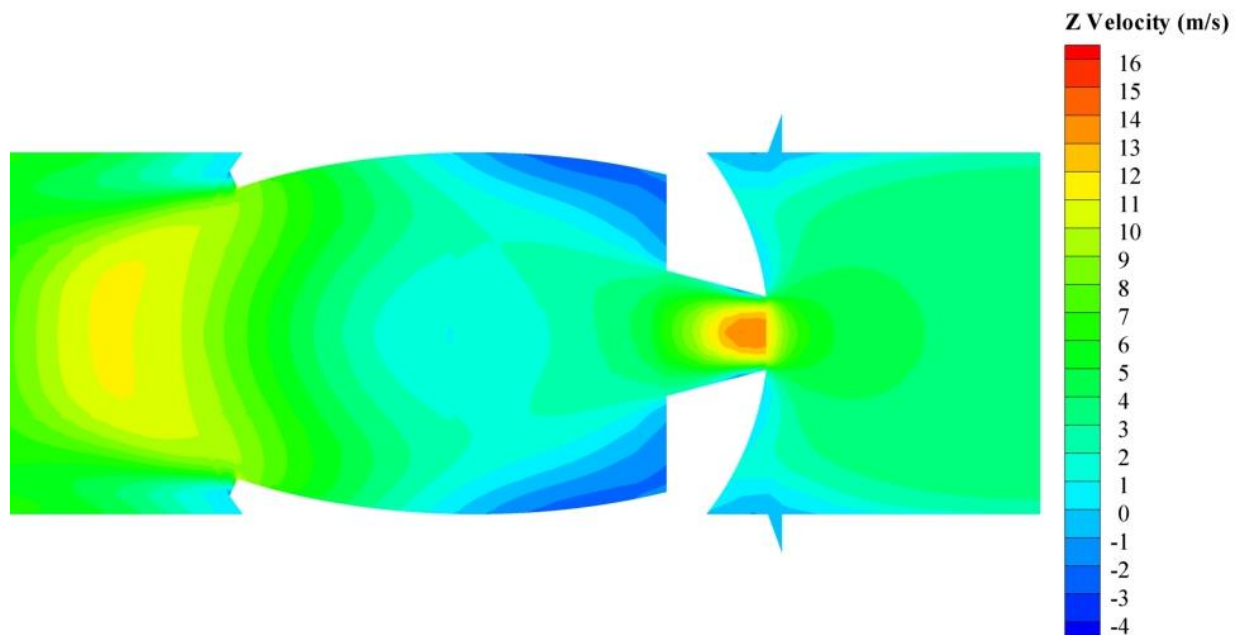


Figure 5-21 Velocity contours predicted by standard k- ϵ for 1 inch 60V FP valve at 70% opening at $Re = 88,900$ in the pipe mid plane

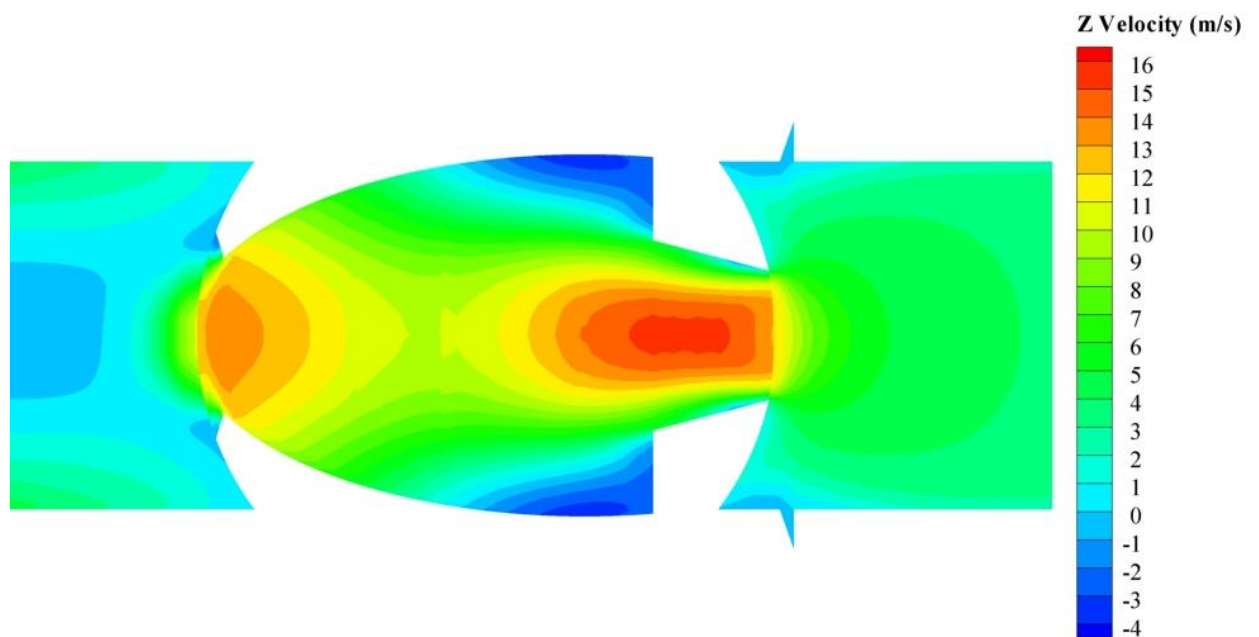


Figure 5-22 Velocity contours predicted by standard k- ϵ for 1 inch 60V FP valve at 70% opening at $Re = 88,900$ in the pipe mid plane

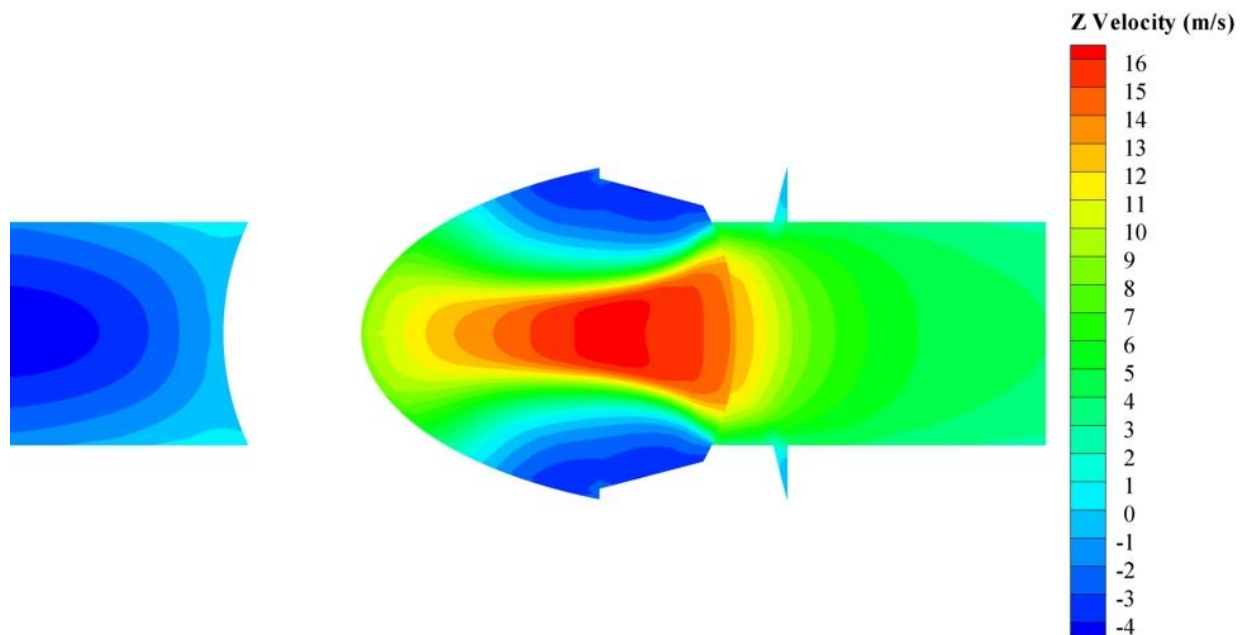


Figure 5-23 Velocity contours predicted by standard k- ϵ for 1 inch 60V FP valve at 70% opening at $Re = 88,900$ in the pipe mid plane

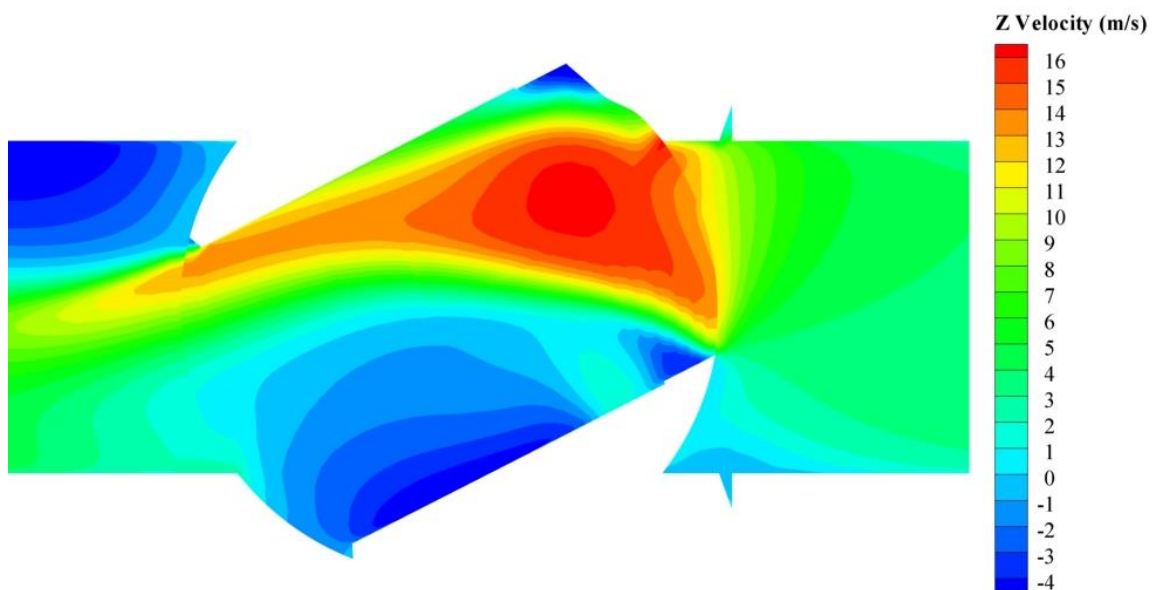


Figure 5-24 Top view of the velocity contours predicted by standard k- ϵ for 1 inch 60V FP valve at 70% opening. The cut plane is the symmetry plane

From the velocity contours, it is observed that as the flow passes through the valve opening, recirculation regions are formed immediately after the opening which indicates the existence of flow separation region at the inlet of the nozzle as flow separates from the wall. Also a small vortex forms in the space below the separated flow region. These regions show where bubbles are formed. However, no information is given about the location of bubble collapse which is the most important here as bubble collapse is the cause of damage and not bubble formation. As the contours move away from the apex of the V, the high velocity region becomes larger.

From figure 4-46, it is known that pitting occurs right after the step of the V; therefore the bubble created should be convected into that region and then collapse. Figure 5-25 shows the vector field of the contour. From this figure one can see how some streams could convect the bubble from the core high velocity stream to the wall after the step of the V where velocity decreases and pressure increases and bubble collapses. The possible trajectory of the bubble is shown using black circles.

Although standard $k-\epsilon$ predicts the cavitation occurrence to be due to flow separation, it does not explain why it only causes damage to the bottom and not the top of the wall of the ball since this model predicts bubble formation on top and bottom flow separation regions.

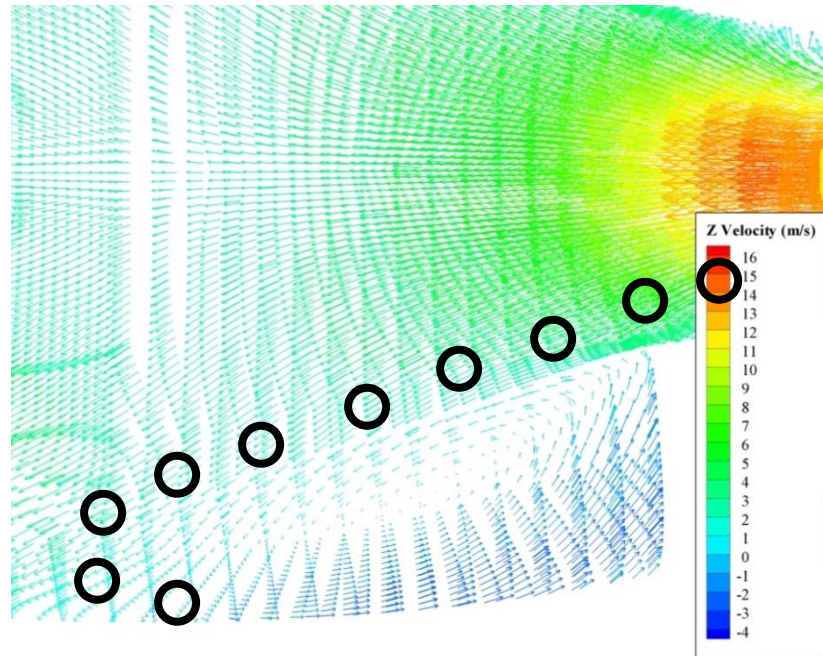


Figure 5-25 Velocity vector field predicted by standard $k-\epsilon$ for 1 inch 60V FP valve at 70% opening, $Re = 88,900$. The vector field is zoomed in the first half of the ball valve after the step of the V. The black circles show the probable trajectory of cavitation bubble convection

Figures 5-26 to 5-29 show the velocity contours predicted by SST $k-\omega$. The key difference between the two predictions is the direction of the high velocity stream after the nozzle. Here the direction of velocity field is towards the bottom of the valve and makes it more likely for the bubble to be convected toward bottom wall after the step in the V and collapse there causing damage. This is in agreement with the location of the pitting in the damaged ball.

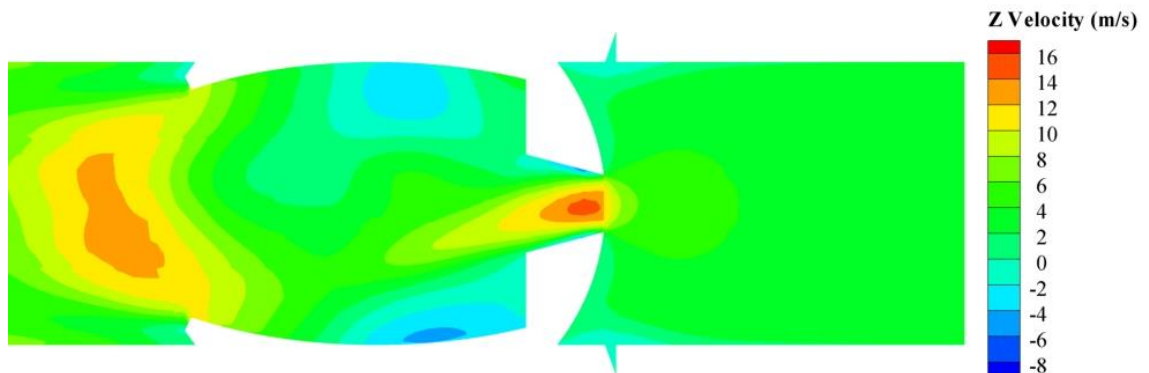


Figure 5-26 Velocity contours predicted by SST $k-\omega$ for 1 inch 60V FP valve at 70% opening at $Re = 88,900$ near the apex

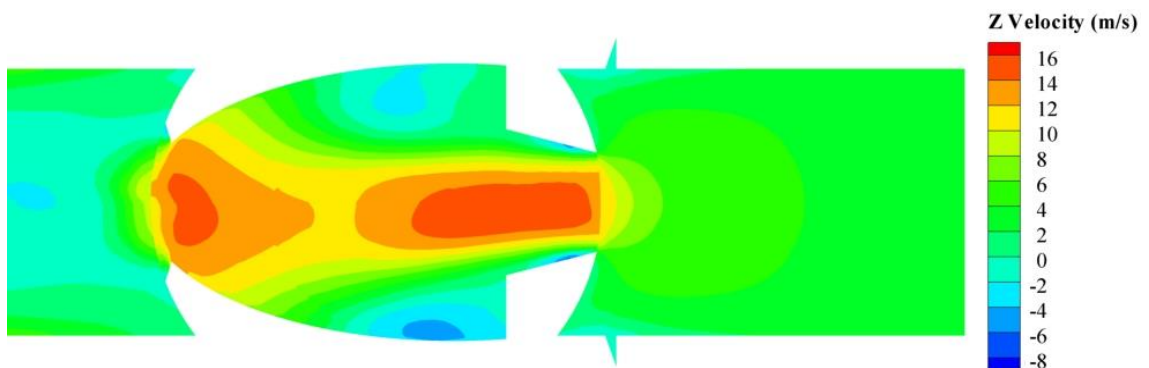


Figure 5-27 Velocity contours predicted by SST $k-\omega$ for 1 inch 60V FP valve at 70% opening at $Re = 88,900$ in the pipe mid plane

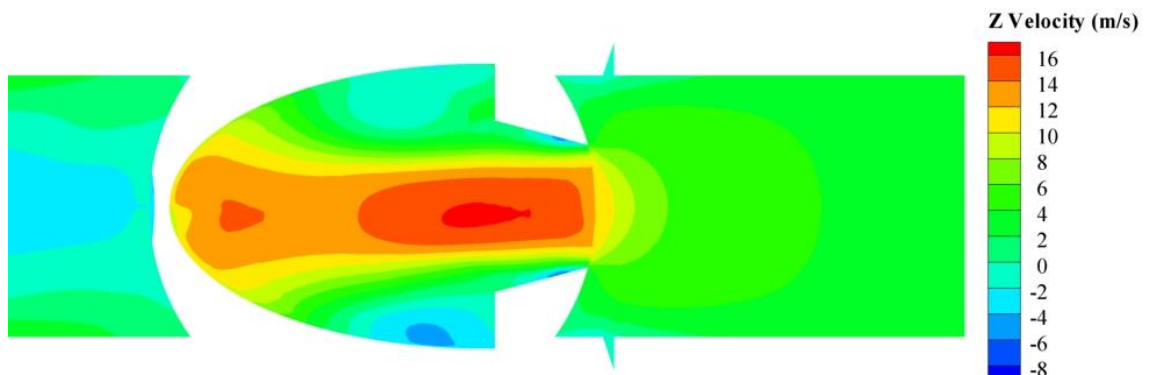


Figure 5-28 Velocity contours predicted by SST $k-\omega$ for 1 inch 60V FP valve at 70% opening at $Re = 88,900$ near the base of the V

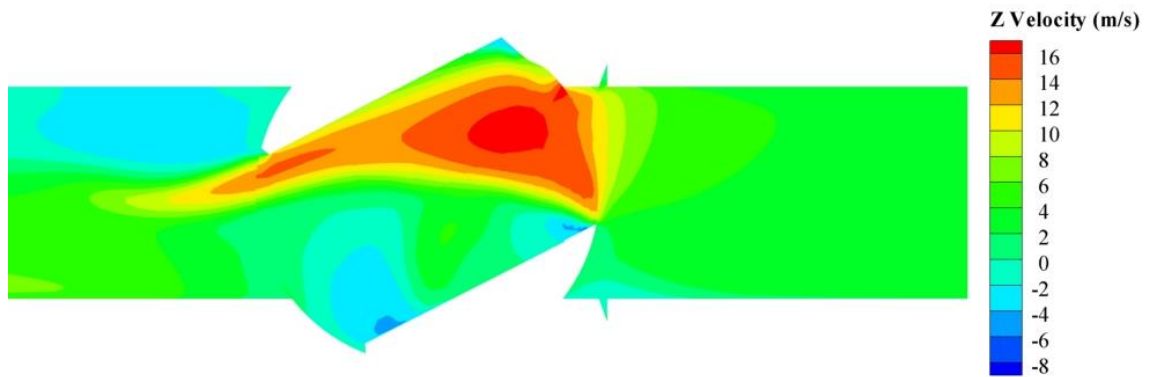


Figure 5-29 Top view of the velocity contours predicted SST k- ω for 1 inch 60V FP valve at 70% opening. The cut plane is the symmetry plane

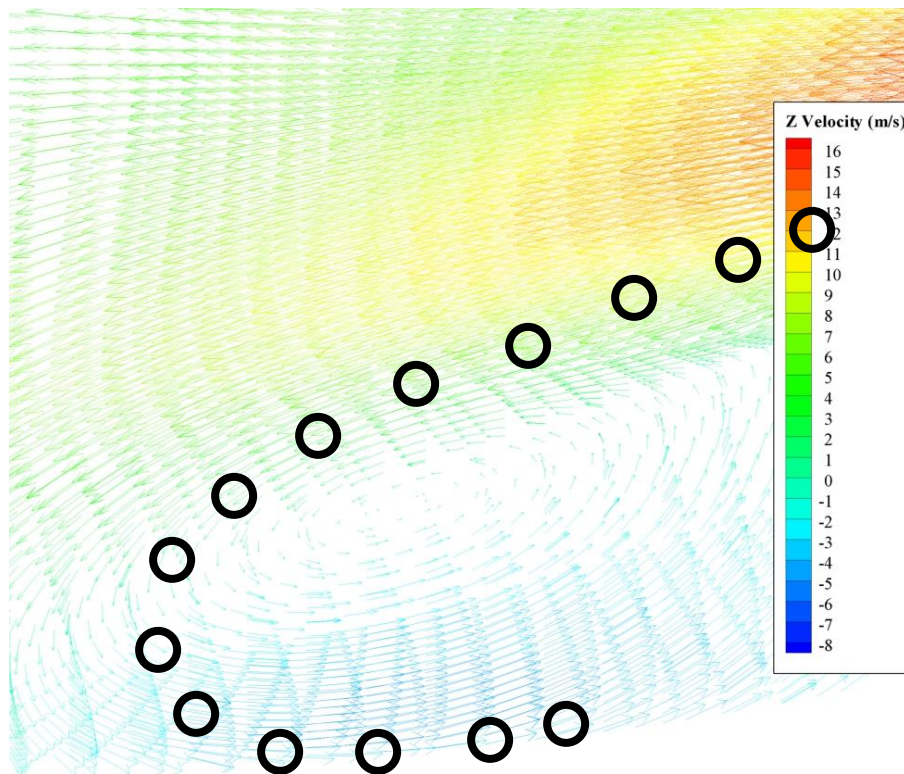


Figure 5-30 Velocity vector field predicted by SST k- ω for 1 inch 60V FP valve at 70% opening, $Re = 88,900$. The vector field only shows the first half of the ball valve after the step of the V. The black circle shows the probable trajectory of a cavitation bubble

Figure 5-30 shows the velocity vector field predicted by SST $k-\omega$. The view is zoomed in the region between right section of the ball and the step of the V where cavitation damage occurred in the experiments. Here it is clearly shown how the high velocity stream travels from the centre to the bottom of the wall of the V where velocity decreases and pressure increases and bubble collapse potentially occurs. These vortices also have greater velocity magnitudes compared to that predicted by standard $k-\epsilon$. This prediction also shows why SST $k-\omega$ is a better choice for valve modelling as the location of damage can be easily explained by the velocity field provided by this model. The probable trajectory of a bubble is shown using black circles.

Same trends were also observed in the CFD predictions of 1 inch 60V full port valves at 50% opening. Figure 5-31 shows the velocity vector predicted by SST $k-\omega$ for Reynolds number of 63,500.

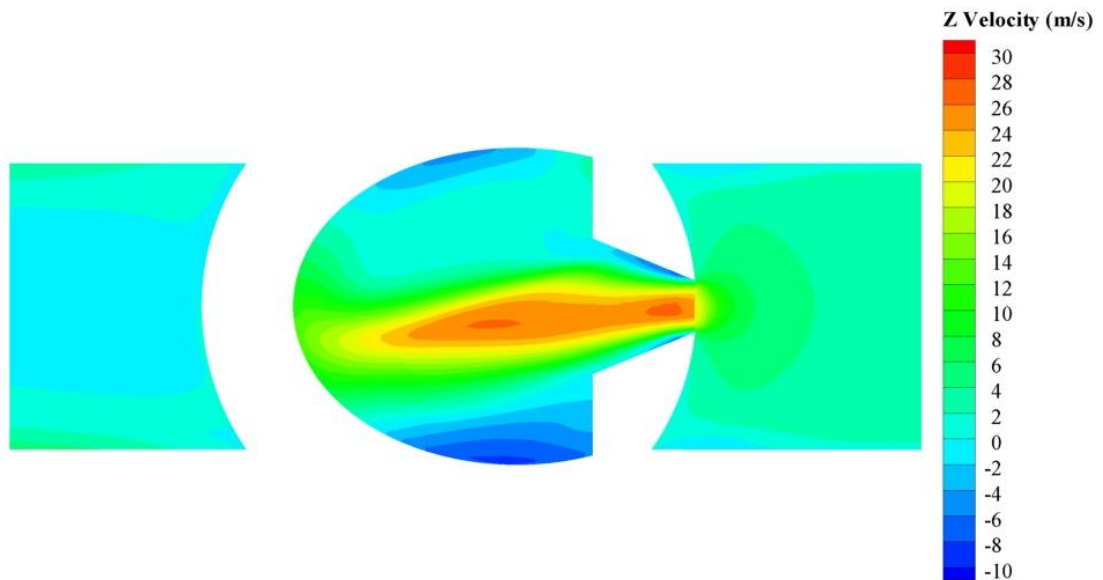


Figure 5-31 Velocity contours predicted by SST $k-\omega$ for 1 in. 60V FP valve at 50% opening, $Re = 63,500$

In the 50% open case, the direction of the accelerated stream is still downwards. However due to smaller cross section, the core stream has higher velocities compared to 70% open case and it requires more space to expand and vortices which convect bubbles into the bottom wall of the ball after the step of the V. The flow separation effects can again be seen which confirms that cavitation occurrence is most likely due to flow separation in valves. From the fundamental cavitation investigations performed by Katz et al. [19], it is known that flow separation plays a major role in cavitation inception.

5.3. Summary

It was observed that SST k- ω and standard k- ϵ perform almost the same in pressure drop predictions. However, it was established that SST k- ω performs better in predicting cavitation compared to standard k- ϵ . SST k- ω has been known to predict separating flows and adverse pressure gradients better than standard k- ϵ and therefore the local information provided by SST k- ω is probably more accurate. This was also established by comparing different velocity and pressure contours and it was confirmed that SST k- ω predicts the probable convection of cavitation bubble better.

6. Conclusions

Experimental investigations as well as numerical studies were conducted to characterise pressure drop and cavitation performance of vari-V ball valves with apex angles of 10, 30, 60 and 90 degrees with inlet diameters of 1, 1.5 and 2 in. The pressure drop performance was characterised using flow and pressure coefficients. The results of flow coefficient studies shows that the smaller apex angle V ball valves should be used for fine control applications where the larger apex angles should be used when a wide range of control is required.

From the pressure coefficient results, it is concluded that the full port valves are scalable if the size of the ball valve is larger than 1.5 in. A set of correlations were developed to characterise the pressure coefficient for a given geometry (apex angle) at different openings. A power law fitted the results the best. Scalability correlations were obtained for each valve only considering 1.5 and 2 in. valves.

Cavitation inception was also investigated here. An acoustic method was employed as well as vibration measurements and the high frequency energy content was monitored to detect cavitation. No trend could be obtained for cavitation inception with change in apex angle at constant bore size. However a trend was observed for cavitation inception for a specific geometry (apex angle) at different sizes. Generally as opening decreases, cavitation number also decreases. However some data points do not fit these trends. This is likely due to turbulent structures in the flow which for some geometry become more

dominant than the effect of the area. Cavitation inception scaling was approached. A correlation was obtained for each ball inlet profile (apex angle) at different sizes.

Numerical investigations were also performed using ANSYS FLUENT. The CFD studies showed that SST $k-\omega$ performs better than standard $k-\epsilon$ for cavitation detection. Local negative pressures were obtained numerically to detect cavitation. If local pressures reached were below vapour pressure, then that operating condition was assumed to be cavitating. It was established that SST $k-\omega$ predicts occurrence of cavitation better compared to the experimental results. Also SST $k-\omega$ turbulence model seems to be predicting the flow field better as the velocity vector field shows better convection of bubble which agrees with the location of damage in the experimental results. The two models predict the flow coefficient within 3% of each other. Therefore it is concluded that using SST $k-\omega$ is sufficient to provide good predictions of flow coefficient and cavitation inception.

The CFD investigations were also used to understand why cavitation occurs in the first place. The lowest pressures were seen in the flow separation regions. This explains the better predictions of SST $k-\omega$ as standard $k-\epsilon$ does not predict flow separation and adverse pressure gradients as well as SST $k-\omega$. However experimental cavitation inception was not determined correctly as the models used are Reynolds averaged which means unsteady flow phenomena are filtered.

6.1. Future Work

Different analysis methods can be investigated. In this study, fast Fourier transform was used. However, using Wavelet Analysis could prove a better technique as it can be used in real time. Also using multivariable analysis and cross correlation of the energies obtained from different devices, could be used to detect cavitation in a system with more than one cavitating components.

Also to predict cavitation inception, volume of fluid technique (VOF) can be employed to model cavitation as a two phase phenomena and observe the travel path of the bubbles and compare the results with experiments. Rayleigh Plesset equations could also be integrated to account for growth and collapse of a bubble. Also time dependent simulations should be performed to capture cavitation inception better. One can start using unsteady RANS models and improve the numerical predictions by performing large eddy simulations.

7. Appendices

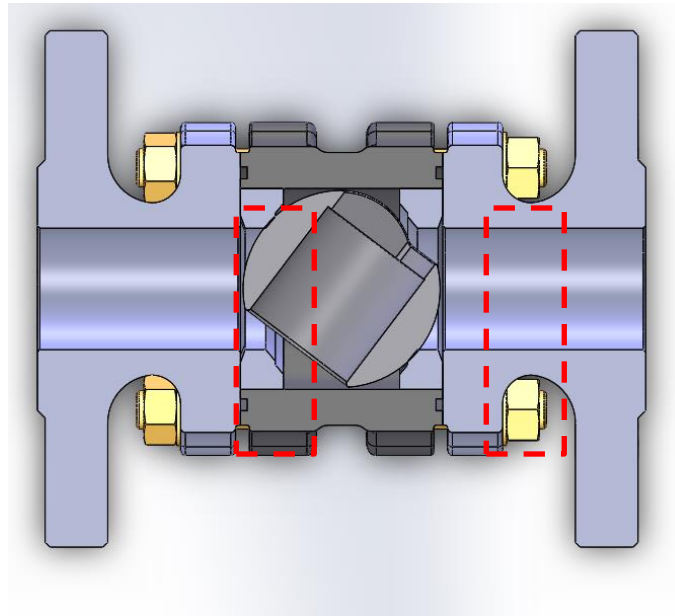


Figure 7-3 Full port valve; the diameter of the flange does not change and it is the same as the piping.

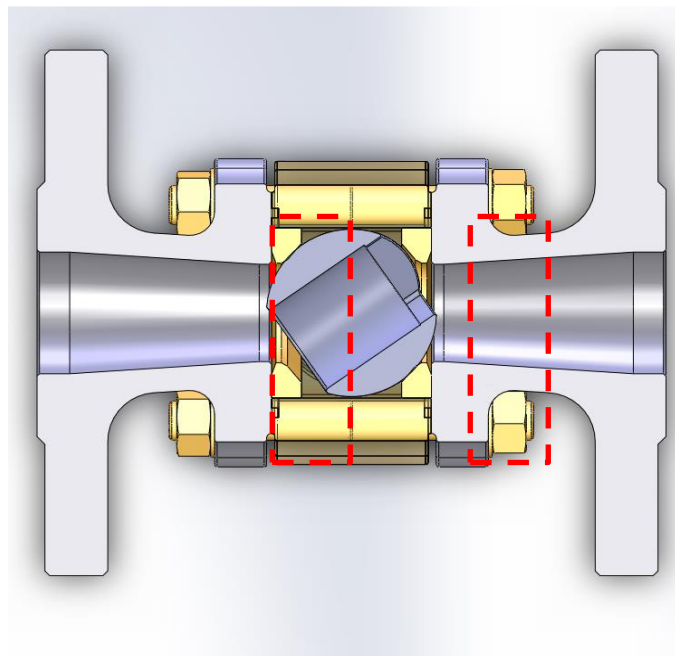


Figure 7-4 Standard port valve; the diameter of the flange changes from the size of the piping to the next smaller size (red dashed lines)

Appendix B. Standard Port Results

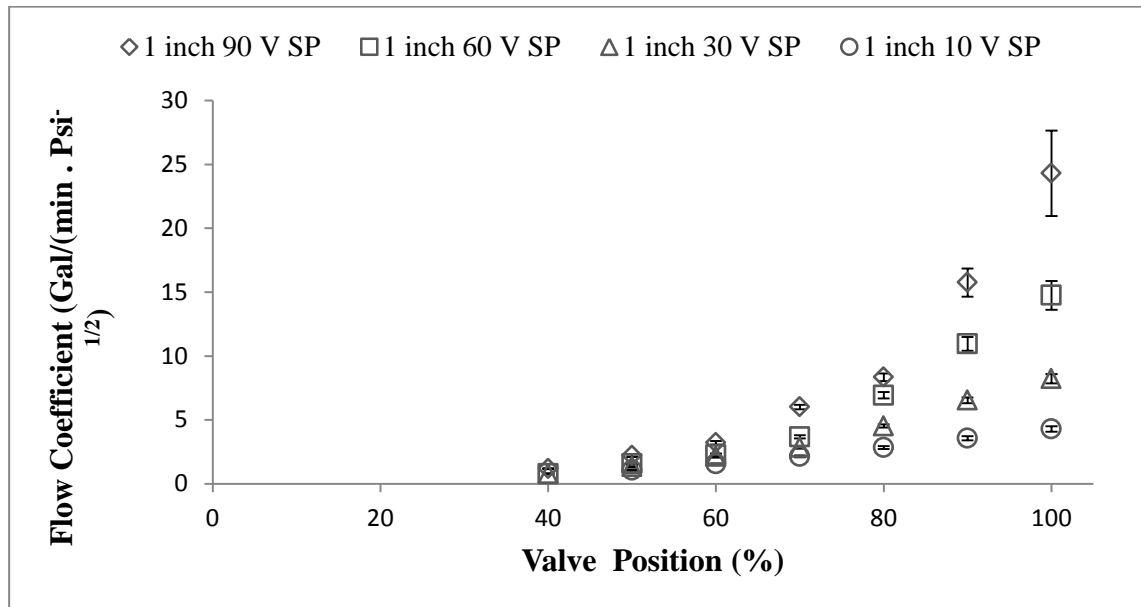


Figure 7-5 Variations of flow coefficient with opening for 1 inch standard port valves with different apex angles

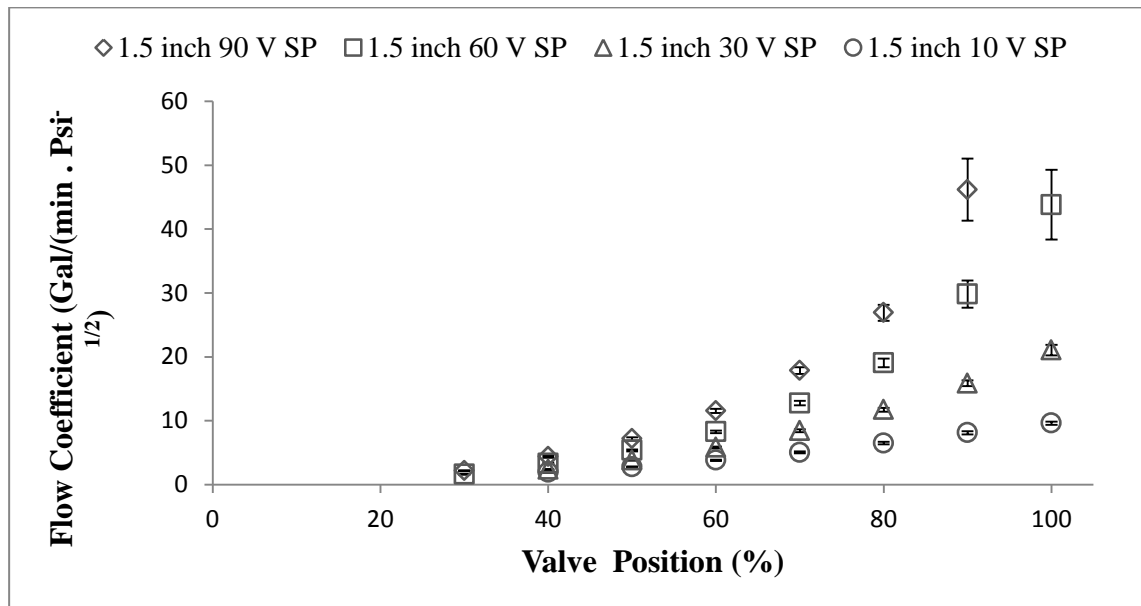


Figure 7-6 Variations of flow coefficient with opening for 1.5 inch standard port valves with different apex angles

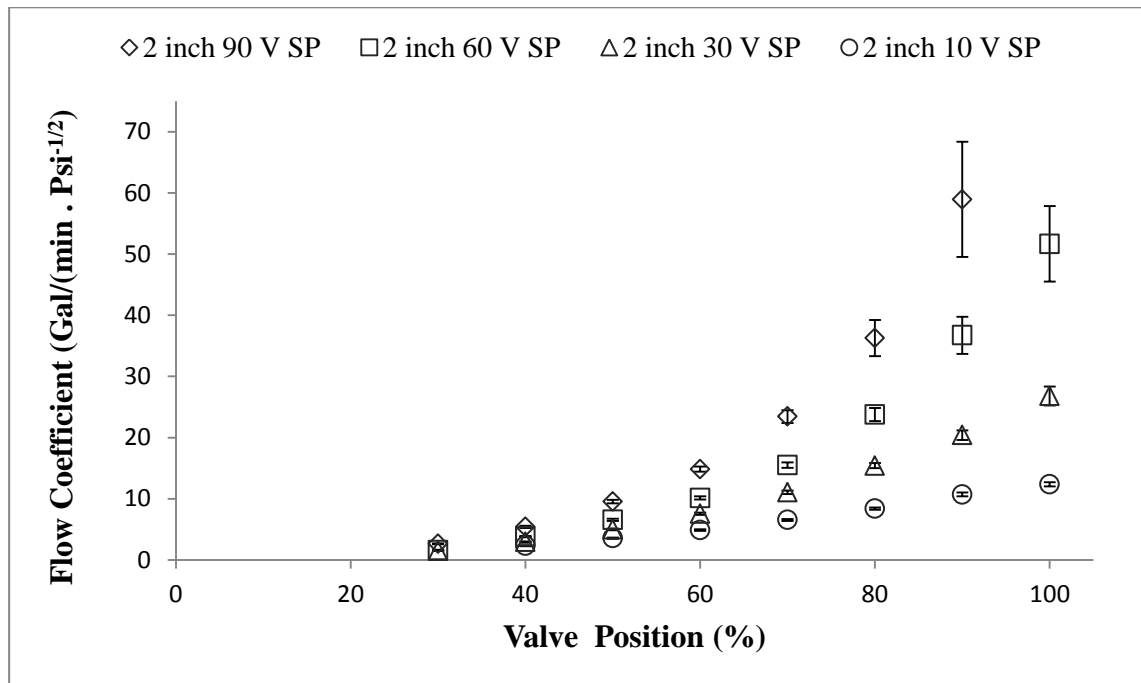


Figure 7-7 Variations of flow coefficient with opening for 2 inch standard port valves with different apex angles

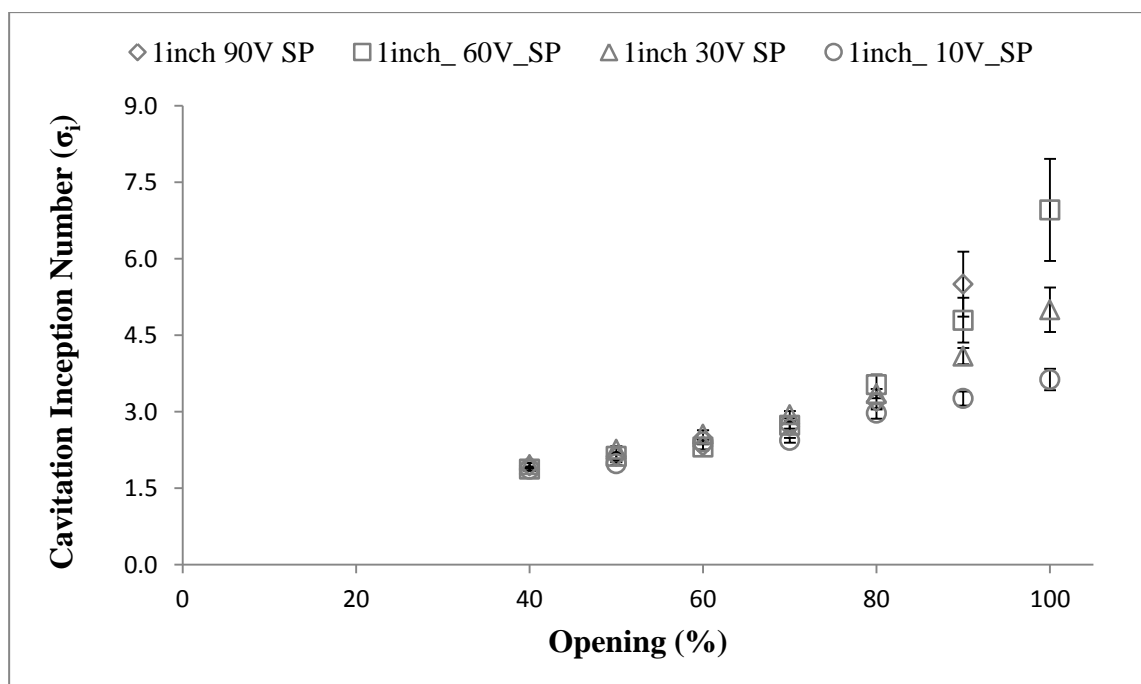


Figure 7-8 Inception cavitation number vs. opening for 1 inch standard port valves

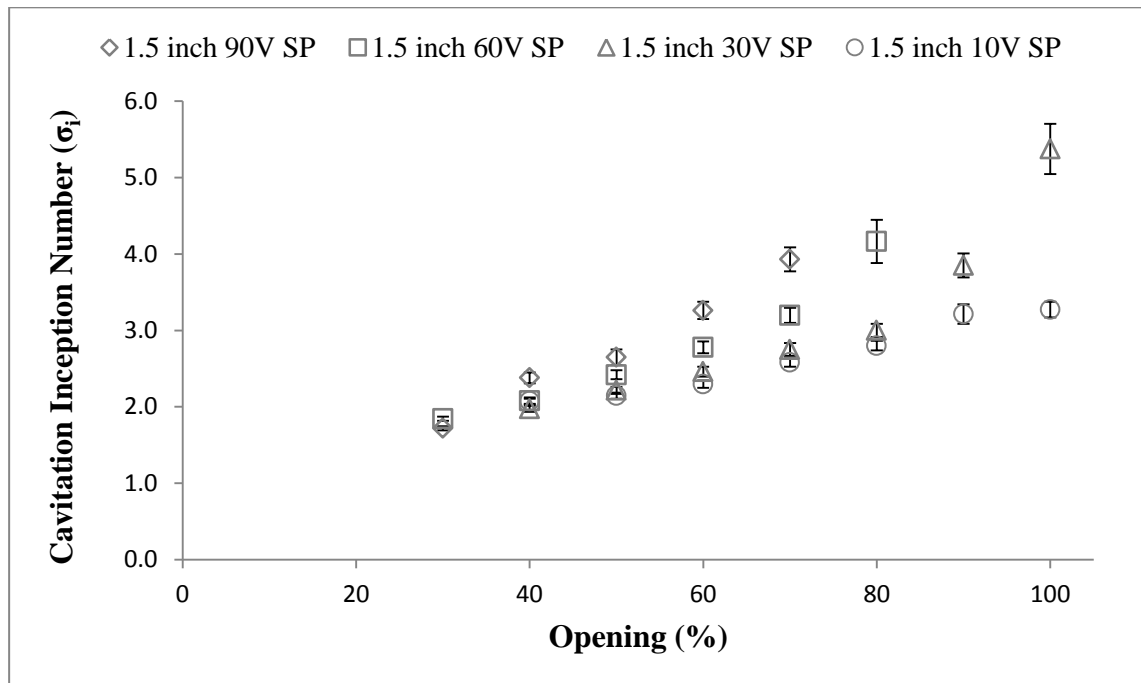


Figure 7-9 Inception cavitation number vs. opening for 1.5 inch standard port valves

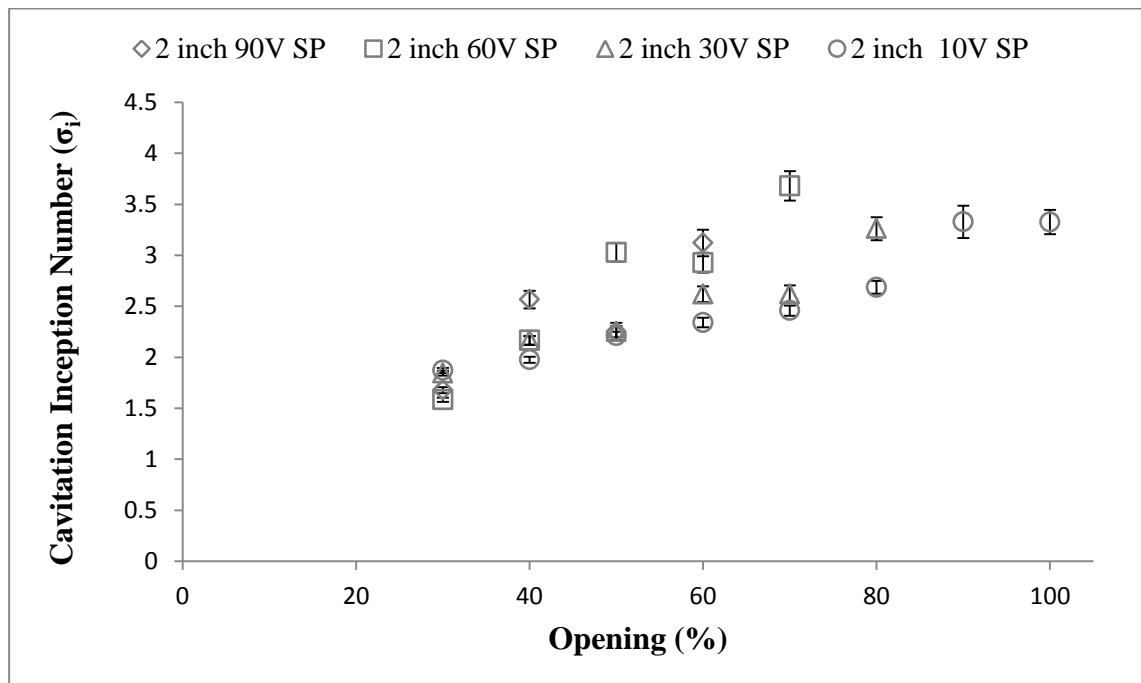


Figure 7-10 Inception cavitation number vs. opening for 2 inch full port valves

Appendix C. Derivations

Flow Coefficient

Starting from Buckingham Pi theory and dimensional analysis for a given geometry and a fully turbulent flow we have:

$$C_P = \frac{2 \Delta P}{\rho v^2}$$

Since flow coefficient is a non-dimensional number, then it is constant for a given opening for fully turbulent flows. If both sides of the equation are divided by square of the pipe cross-sectional area we have:

$$\frac{C_P}{A^2} = \frac{2 \Delta P}{\rho v^2 A^2}$$

But since $Q^2 = v^2 A^2$ and rearranging the equation we have:

$$\frac{C_P \rho}{2 A^2} = \frac{\Delta P}{Q^2}$$

If the equation is inverted then we have:

$$\frac{2 A^2}{C_P \rho} = \frac{Q^2}{\Delta P}$$

But since we require the left hand side to be constant both sides are multiplied by ρ/ρ_0 :

$$\frac{2 A^2}{C_P \rho_0} = \frac{\rho}{\rho_0} \frac{Q^2}{\Delta P}$$

By taking the square root of both sides we have:

$$\sqrt{\frac{2A^2}{C_P \rho_0}} = Q \sqrt{\frac{\rho/\rho_0}{\Delta P}}$$

and since area, flow coefficient, and reference density are all constant for a given opening for a fully turbulent incompressible flow, the value of flow coefficient will be constant.

$$C_v = \sqrt{\frac{2A^2}{C_P \rho_0}} = Q \sqrt{\frac{\rho/\rho_0}{\Delta P}}$$

Appendix D. Error Analysis

The error analysis was performed using the method described by [55]. This method reports the error with a 95% confidence. The general formulation is:

$$\delta f = \sqrt{\sum_{i=1}^n \left(\frac{\partial f}{\partial x_i} \Delta x_i \right)^2}$$

Uncertainty of Pressure Measurements Devices

Three transducers were used for different gauge pressures. The various uncertainties associated with each transducer are:

- i. Uncertainty of the transducer ($\pm 0.5\%$ of full scale)
- ii. The resolution of the pressure calibrator (0.001 psi for Pressures below 36 psi and 0.01 for pressures between 36 and 300 psi)

The uncertainty of each pressure reading is:

$$\delta P_{2.5 \text{ psi}} = \sqrt{(0.005 \times 2.5)^2 + (0.001)^2} = 0.013 \text{ psi}$$

$$\delta P_{25 \text{ psi}} = \sqrt{(0.005 \times 25)^2 + (0.001)^2} = 0.13 \text{ psi}$$

$$\delta P_{50 \text{ psi}} = \sqrt{(0.005 \times 50)^2 + (0.01)^2} = 0.25 \text{ psi}$$

$$\delta P_{\text{differential}} = \sqrt{(0.005 \times 80)^2 + (0.01)^2} = 0.40 \text{ psi}$$

where the 2.5 psi, 25 psi, 50 psi and differential correspond to 2.5 psi pressure transducer, 25 psi pressure transducer, 50 psi pressure transducer and differential pressure transducer.

Uncertainties of Volumetric Flow Meter

The flow rate in the loop was measured using two turbine flow meters. The calibration curve provided by the manufacturer indicates a 1.0 % (of reading) error for the FTB-1425 and a repeatability of 0.1%. The error of this device can be assumed 1.0%. The calibration of the display and connecting the display to a 16 bit DAQ with a resolution of 300 μ V reduced the significance of these errors and they were neglected.

The low flowmeter has an error of 2.0% (of reading) and a repeatability of 0.1%. However as this flowmeter could not be connected to the DAQ, the screen also has a 1% resolution accuracy associated with it. The total error of the low flow meter is:

$$\delta Q_{Low} = \sqrt{0.01^2 + 0.02^2 + 0.001^2} = 2.2 \%$$

Uncertainty of Pressure Drop Measurements

When pressure drops were measured by taking the difference between the two gauge pressure transducers, an uncertainty was associated with the pressure drop calculations. These uncertainties are calculated as:

$$\Delta P_{25-2.5} = \sqrt{\delta P_{50 \text{ psi}}^2 + \delta P_{2.5 \text{ psi}}^2} = 0.125 \text{ psi}$$

$$\Delta P_{50-2.5} = \sqrt{\delta P_{50 \text{ psi}}^2 + \delta P_{2.5 \text{ psi}}^2} = 0.25 \text{ psi}$$

$$\Delta P_{50-25} = \sqrt{\delta P_{50 \text{ psi}}^2 + \delta P_{2.5 \text{ psi}}^2} = 0.28 \text{ psi}$$

Uncertainty of Upstream Gauge Pressure Measurement Using Differential Pressure Transducer

If the differential pressure transducer is used then the error of gauge pressure at upstream is:

$$\delta P_{\text{differential}+2.5 \text{ psi}} = \sqrt{(0.4)^2 + (0.013)^2} = 0.40 \text{ psi}$$

$$\delta P_{\text{differential}+25 \text{ psi}} = \sqrt{(0.4)^2 + (0.13)^2} = 0.42 \text{ psi}$$

Maximum Uncertainty of Absolute Pressures

To calculate the maximum error of the absolute pressures, the errors of the gauge pressure was obtained as well as the error of atmospheric pressure. Three transducers were used for different absolute pressure determination. Due to lack of a barometer, the atmospheric pressure was obtained for each day from McMaster University weather measurement station and Hamilton central mountain weather. The uncertainties here are:

- i. Uncertainty of the transducer
- ii. The error in atmospheric pressure calculation (maximum of 1.3 kPa (0.18 psi) depending on atmospheric fluctuations in a day)

The uncertainties in absolute pressure measurements for each device are:

$$\delta_{ABS} P_{2.5 \text{ psi}} = \sqrt{(0.013)^2 + (0.18)^2} = 0.18 \text{ psi}$$

$$\delta_{ABS} P_{25 \text{ psi}} = \sqrt{(0.13)^2 + (0.18)^2} = 0.22 \text{ psi}$$

$$\delta_{ABS} P_{50 \text{ psi}} = \sqrt{(0.25)^2 + (0.18)^2} = 0.31 \text{ psi}$$

$$\delta_{ABS} P_{\text{differential \& 2.5 psi}} = \sqrt{(0.40)^2 + (0.18)^2} = 0.47 \text{ psi}$$

$$\delta_{ABS} P_{\text{differential \& 2.5 psi}} = \sqrt{(0.42)^2 + (0.18)^2} = 0.49 \text{ psi}$$

Pipe Average Velocity Uncertainties:

To evaluate Reynolds numbers and pressure coefficients, velocities had to be used. The velocity was calculated using:

$$u = \frac{4Q}{\pi d^2}$$

Uncertainties of the velocity calculated are due to:

- i. Uncertainties in diameters (± 0.005 inch and therefore negligible)
- ii. Uncertainty in flow rate determination (1% of the reading)

The error of the velocity can be obtained using:

$$\frac{\delta u}{u} = \sqrt{\left(\frac{\delta Q}{Q}\right)^2 + \left(\frac{\delta d^2}{d^2}\right)^2}$$

The maximum uncertainty of velocities obtained was not found individually and the value was carried forward in the calculation spreadsheet to calculate the error of pressure coefficient.

Pipe Reynolds Number Uncertainty:

To evaluate the uncertainty of pipe Reynolds numbers, each individual component which causes uncertainties must be identified. These variables are:

- i. Uncertainties in diameters (± 0.005 inch and therefore negligible)
- ii. Uncertainty in velocity calculation (Value Forwarded from previous calculation)
- iii. Neglecting changes in the properties of the fluid

The uncertainty of the pipe Reynolds number can be obtained using:

$$\frac{\delta Re}{Re} = \sqrt{\left(\frac{\delta u}{u}\right)^2}$$

The maximum uncertainty of the pipe Reynolds number was found to be less than 5%.

Flow Coefficient Uncertainty

The flow coefficient (C_v) is dependent on pressure drop and flow rate uncertainties. However it is also a function of pressure drop and uncertainty values which causes this parameter to be very sensitive to the actual values of flow rate and pressure drop. The uncertainty equation becomes:

$$\delta C_v = \sqrt{\left(\sqrt{\frac{SG}{\Delta P}} \times \delta Q\right)^2 + \left(\frac{-Q}{2\Delta P} \sqrt{\left(\frac{SG}{\Delta P}\right)} \times \delta \Delta P\right)^2}$$

The maximum uncertainty of flow coefficients was as high as 21.5 %. However, the nominal errors were less than 5%.

Cavitation Number Uncertainty

The cavitation number (σ) is dependent on pressure drop and absolute pressures. Again this value is sensitive to which sensor was used and how large the values of pressures are.

The uncertainty equation becomes:

$$\frac{\delta \sigma}{\sigma} = \sqrt{\left(\left(\frac{\delta(\Delta P)}{\Delta P}\right)^2 + \left(\frac{\delta ABS P_{up}}{ABS P_{up}}\right)^2\right)^{\frac{1}{2}}}$$

The maximum uncertainty of cavitation number in the experiments was 16.1%. The nominal errors were less than 4%.

Pressure Coefficient Uncertainty

Pressure coefficient is dependent on pressure drop and velocities obtained. Again this value is sensitive to which sensor was used and how large the values of pressure drops are. The uncertainty equation becomes:

$$\frac{\delta C_P}{C_P} = \sqrt{\left(\frac{\delta(\Delta P)}{\Delta P}\right)^2 + \left(\frac{2(\delta u)^2}{u^2}\right)^2}$$

The maximum error obtained in the experiments was 20.8%. However, the nominal errors are less than 5%.

Random Error Determination

From the experimental setup, 90,000 samples of pressure upstream of the valve and downstream of the valve were obtained. Since data acquisition was performed simultaneously (simultaneous data acquisition means that data were recorded from all channels at the same time rather than recording data from each channel in a sequence), the following becomes true:

$$\Delta P_i = P_{up(i)} - P_{down(i)}$$

Here “i” is the sample number. Therefore the pressure drop across the valve at any given time can be obtained. If this is performed for all 90,000 samples then a sampling train for ΔP can be obtained. However for each sample the error becomes:

$$\delta(\Delta P)_i = \sqrt{\Delta P_{up(i)}^2 + \Delta P_{down(i)}^2}$$

Using the equation above a ΔP sample can be obtained where each data point has an associated error. To calculate the final error of ΔP , the following is used:

$$\delta(\Delta P)$$

$$= \sqrt{\left(\frac{1}{N} \sum_{i=1}^N \delta(\Delta P)_i + 2 \left(\frac{1}{N} \sum_{i=1}^N (\delta(\Delta P)_i - \overline{\delta(\Delta P)})^2 \right) \right)^2 + \left(\frac{1}{N} \sum_{i=1}^N (\Delta P_i - \overline{\Delta P})^2 \right)^2}$$

Also a sample of 90,000 data points is obtained for the flow rate. The total error is calculated using:

$$\delta Q = \sqrt{\frac{1}{N} \sum_{i=1}^N \delta Q_i + \frac{1}{N} \sum_{i=1}^N (Q_i - \bar{Q})^2}$$

Average Flow Coefficient Analysis

To obtain a representative value of flow coefficient for all values of pipe Reynolds number in the turbulent region, one value had to be obtained. This value was determined to be the average of all non cavitating flow coefficients obtained. If the Reynolds number associated with a data point was less than 20,000 and the error was higher than 15%, that data point was neglected. Also, if the measured pressure values were less than 10% of the full scale of the static pressure transducer used, the data points were neglected. The error was calculated using:

$$\delta \overline{C_v} = \frac{1}{n} \sum_{i=1}^n \delta C_v$$

To determine the errors in the final values obtained, the total error in each transducer was obtained by calibrating the sensors individually. Figure 7-11 to Figure 7-15 show the

calibrations performed along with the obtained equations. Three types of linear, polynomial and power curves were fitted to each graph and the errors were calculated by subtracting the estimated value from the curves from the actual value and the maximum error was noted as the systematic error of calculations. The curve fit with lowest maximum error was chosen as the calibration equation.

Calibrations and Transducer Error

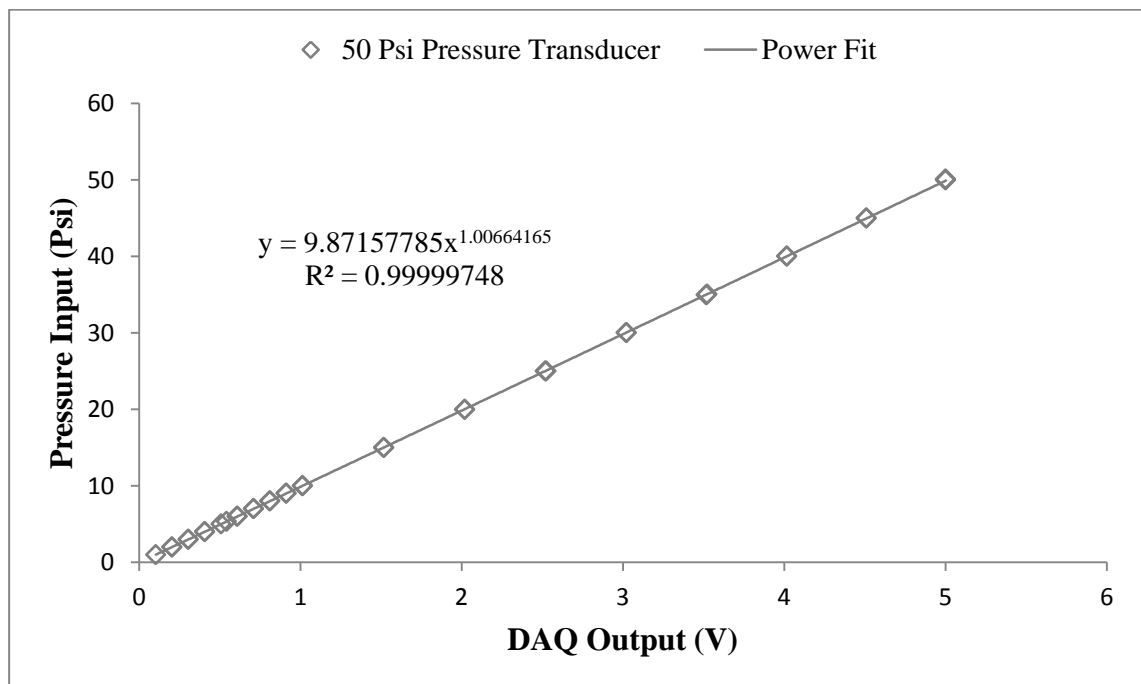


Figure 7-11 Pressure calibration curve for Honeywell 50 psi gauge pressure transducer

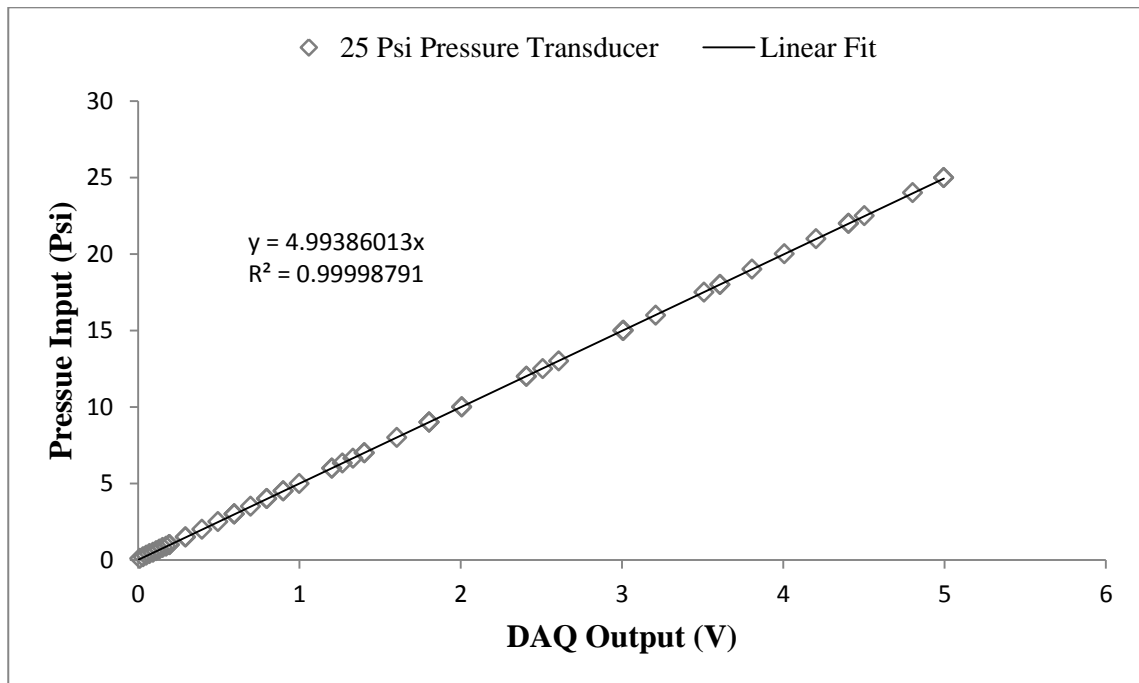


Figure 7-12 Pressure calibration curve for Honeywell 25 psi gauge pressure transducer

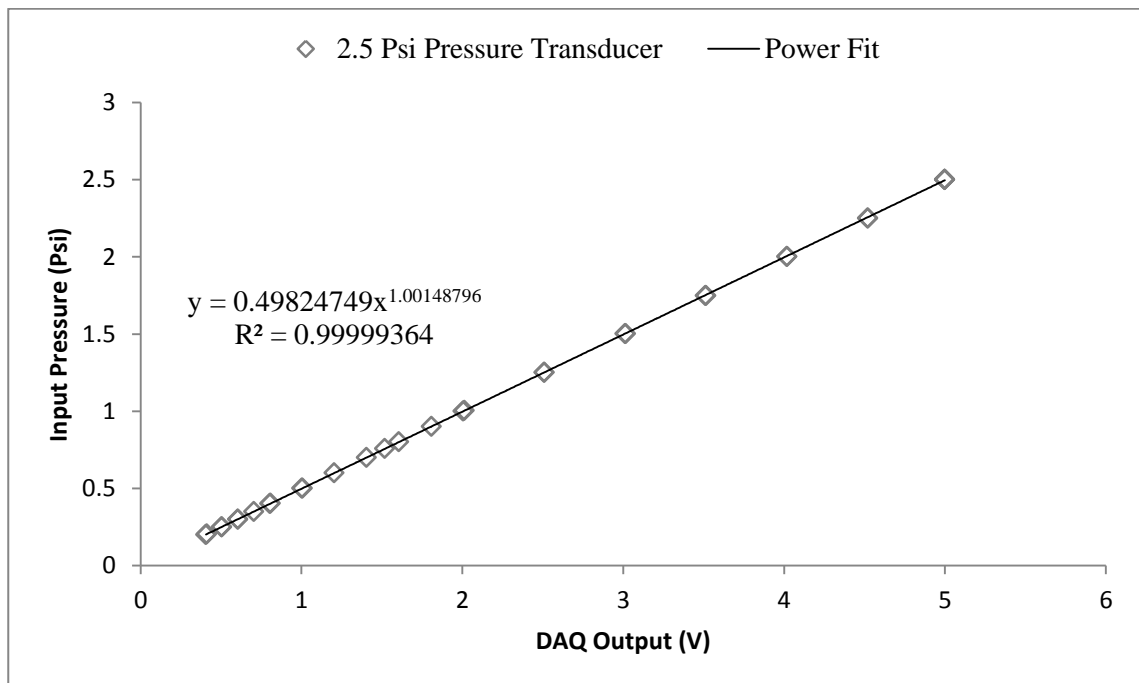


Figure 7-13 Pressure calibration curve for Honeywell 2.5 psi gauge pressure transducer

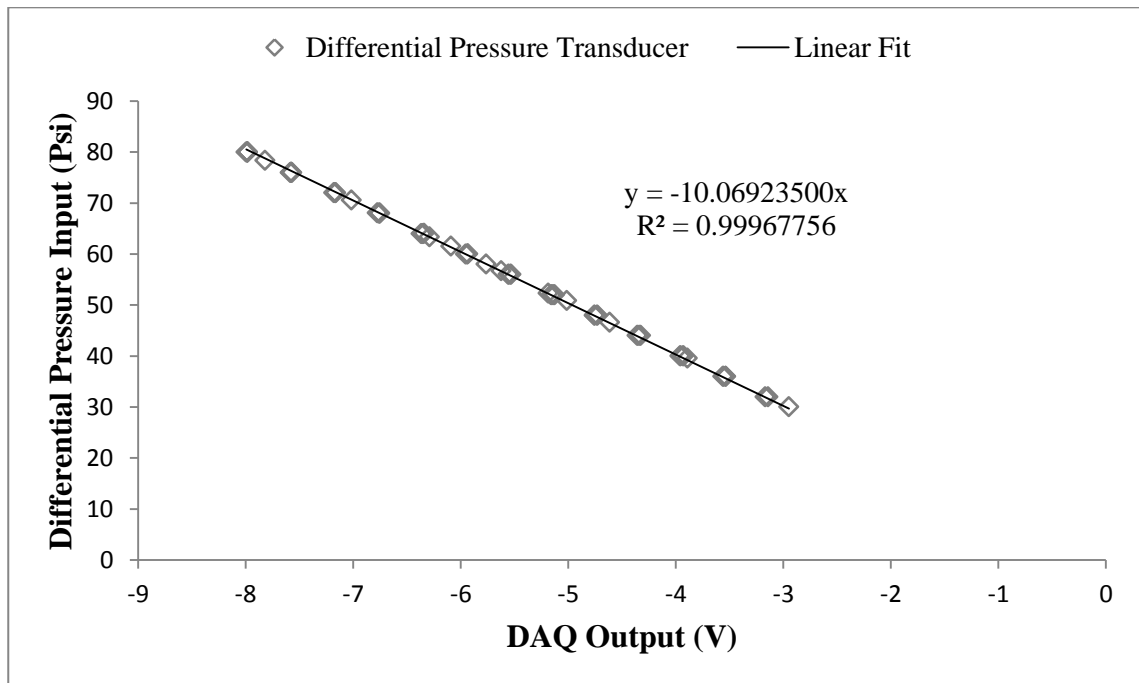


Figure 7-14 Pressure calibration curve for Validyne DP 15 differential pressure transducer

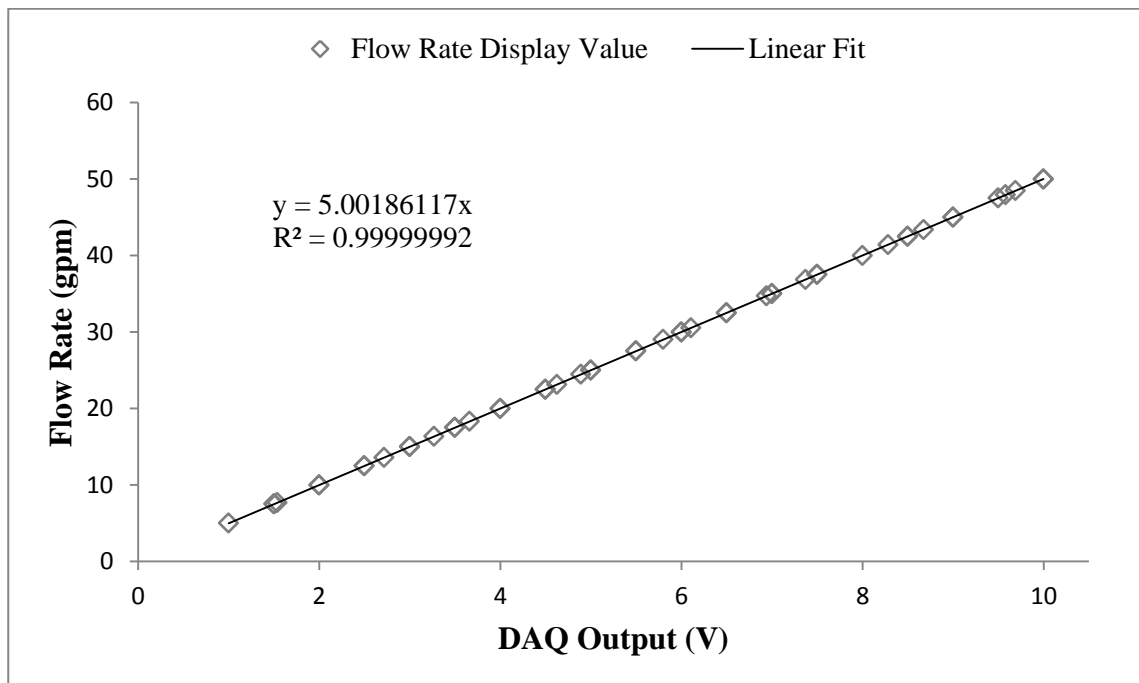


Figure 7-15 Flow rate calibration curve for Omega FTB-1425 Flow meter

Device	Measurement	Max. Uncertainty
Honeywell 50 psi Pressure Gauge	Pressure (psi)	0.42 %
Honeywell 25 psi Pressure Gauge	Pressure (psi)	0.82 %
Honeywell 2.5 psi Pressure Gauge	Pressure (psi)	0.38 %
Validyne DP-15 80 psi Differential Pressure	Pressure (psi)	1.18 %
Omega FTB-1425 Flow Meter	Flow Rate (gpm)	1.00 %

Table 7-1 Calibration Error Table

Accelerometer Calibration

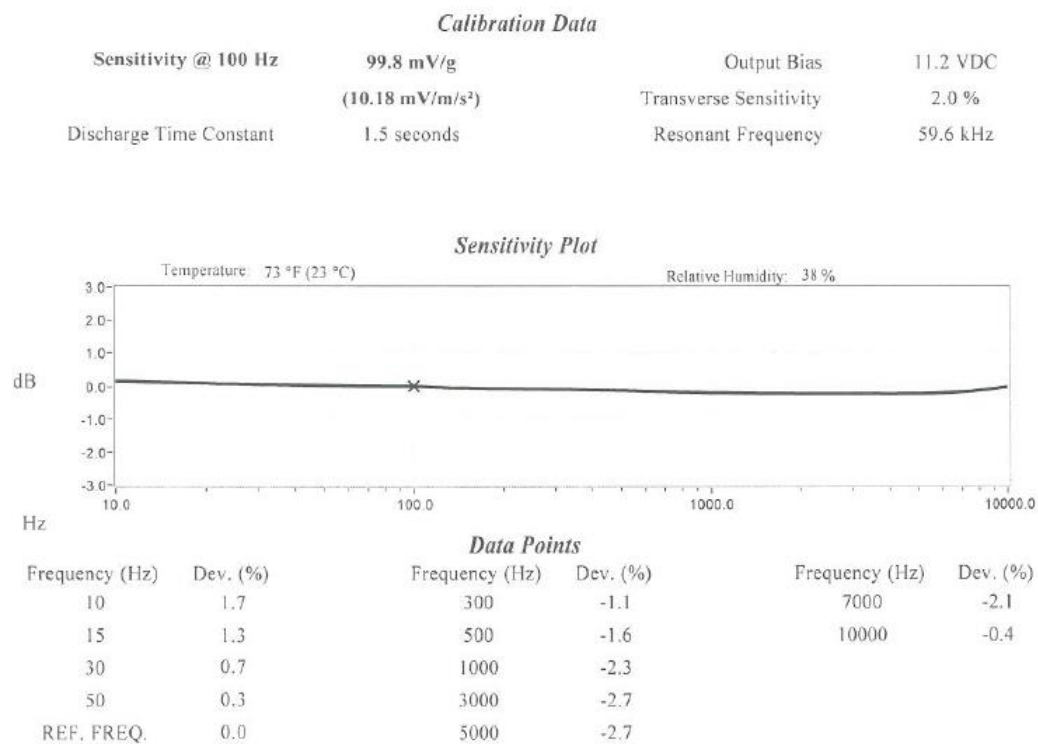


Figure 7-16 Calibration Sheet of the accelerometer

Appendix E. Pressure Fluctuations

Initially to detect pressure drop in valves, a new technique was developed and tested. In this technique, the pressure drop in downstream and upstream pipes was measured in 6 inch increments and they were extrapolated to obtain the pressure drop across the valve. Figure below demonstrates how the pressure drop across the valve was initially supposed to be determined.

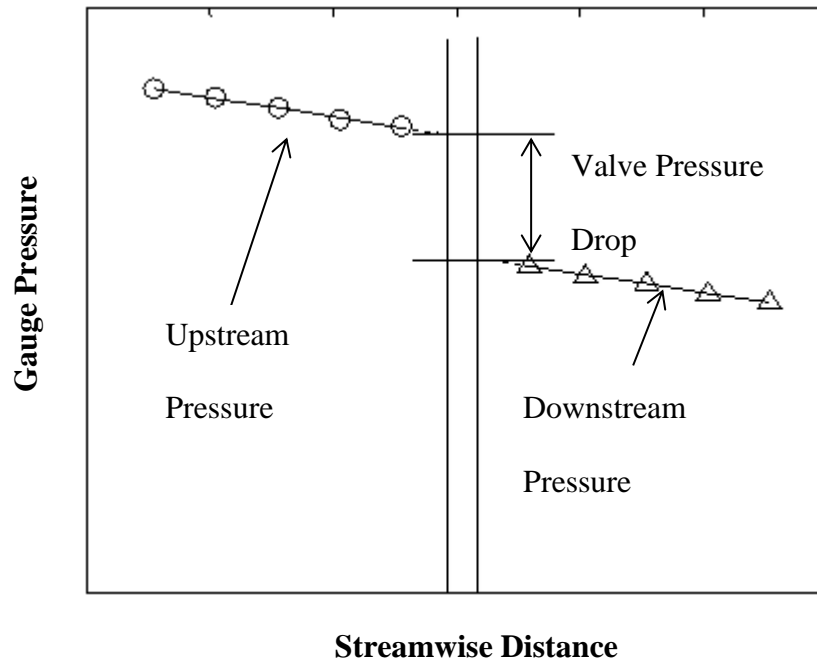


Figure 7-17 Valve pressure determination methodology

Although, using this technique is theoretically possible, in practice it was proven difficult and erroneous. This is due to the pressure fluctuations when a differential pressure transducer was used between two ports. To obtain accurate results, the range of the differential pressure transducer used was small. However, the pressure fluctuations were

also within the same range and this caused the standard deviations to be larger in some cases than the mean value.

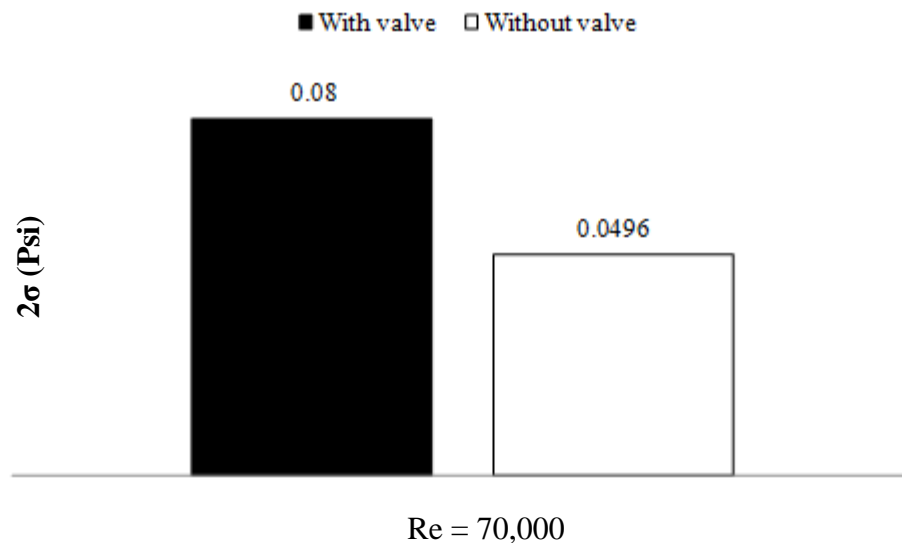


Figure 7-18 Standard deviation of pressure fluctuations in the pipe when a valve is installed compared to no valve case scenario

The figure above shows standard deviation of pressure fluctuations in a pipe. The existence of the valve increases the intensity of pressure fluctuations. This can be used to explain why cavitation inception is intermittent first in these valves as pressure fluctuations are stronger here compared to the time when no valve is installed.

Appendix F. Scaling Example

The 60V full port valve at 70% opening was chosen to evaluate the scalability correlations developed. The CFD model was scaled up to 4 inch pipe diameter and a numerical solution was obtained using standard k- ϵ in FLUENT. The flow coefficient value was obtained from the solution. Also by referring to the pressure coefficient correlations developed experimentally, the flow coefficient was estimated. The following table shows a comparison of CFD predictions of GOSCO (SolidWorks) and FLUENT with experimental correlation of pressure coefficient for 60V full port valves at 70% opening for three different sizes.

Size	FLUENT	GOSCO	Experimental Correlation	Discrepancy
4 inch	109.97	118.86	123.1	12.0 %
6 inch	247	272	277.0	11.9 %
8 inch	440.1	Not Available	492.5	11.9 %

Table 7-2 Comparison of prediction of flow coefficients obtained using different methods

In the table above, the discrepancy was calculated between the results of simulations in FLUENT and the experimental correlation. Assuming that the results of FLUENT predictions are within 3% of the actual value (as was the case for 1 inch FP valve), it can be concluded that using the pressure coefficient correlation predicts the flow coefficient within 12% of the FLUENT results and within 3.5% of the CFD code used by GOSCO. Given the computational and actual cost of using CFD, the correlation developed performs acceptably to obtain an estimate of the flow coefficient for larger valve sizes.

Appendix G. Computational Grid

The Block	Mesh Properties				
	First Node length	Last Node length	Expansion ratio	Number Of Nodes	Mesh Law
Inlet Pipe	0.102	0.102	1	50	BiGeometric
Outlet Pipe	0.101	0.101	1	80	BiGeometric
V O-grid (External)	0.010	0.010	1	7	BiGeometric
V O-grid (Internal)	0.012	0.012	1	60	BiGeometric
Ball Outlet O- Grid (External)	0.0036	0.0036	1	4	BiGeometric
Ball Outlet O- Grid (Internal)	0.012	0.012	1	7	BiGeometric
Inlet Flange	0.036	0.05	1.37	36	BiGeometric
Outlet Flange	0.05	0.05	1	40	BiGeometric
Inlet O-grid (External)	0.005	0.005	1	10	BiGeometric
Inlet O-grid (Internal)	0.0095	0.0095	1	18	BiGeometric

Outlet O-grid (Internal)	0.009	0.009	1	20	BiGeometric
Outlet O-grid (External)	0.0069	0.0069	60	20	BiGeometric

References

- [1] S. J. Thornycroft and S. W. Barnaby, "Torpedo Boat Destroyers," *Journal of American Society For Naval Engineers*, vol. 7, no. 4, pp. 711-736, 1895.
- [2] E. A. Weitendorf, *Fourth International Symposium on Cavitation*, Pasadena, CA: CaltechCONF, 2001, p. ID Code: 85.
- [3] E. N. Harvey, D. K. Barnes, W. D. McElroy, A. H. Whiteley, D. C. Pease and K. W. Cooper, "Bubble Formation in Animals," *Journal Of Cellular And Comparative Physiology*, vol. 24, no. 1, pp. 1-22, 1944.
- [4] L. Rayleigh, "On The Pressure Developed in a Liquid During The Collapse of a Spherical Cavity," *Philosophical Magazine*, vol. 34, no. 200, pp. 94 - 98, 1917.
- [5] M. S. Plesset, "The Dynamics of a Cavitation Bubble," *ASME Journal of Applied Mechanics*, vol. 16, pp. 228-231, 1949.
- [6] B. E. Noltingk and E. A. Neppiras, "Cavitation Produced by Ultrasonics," *Proceedings of The Physical Society*, vol. 63, pp. 674-685, 1950.
- [7] H. Poritsky, "The Collapse or Growth of a Spherical Bubble or Cavity in Viscous Fluid," *Proceedings Of The First U.S. National Congress Of Applied Mechanics*, pp. 813-821, 1952.

- [8] C. E. Brennen, *Cavitation and Bubble Dynamics*, New York: Oxford University Press, 1995.
- [9] M. S. Plesset and R. B. Chapman, "Collapse of an Initially Spherical Vapour Cavity in The Neighbourhood of a Solid Boundary," *Journal Of Fluid Mechanics*, vol. 47, no. 2, pp. 283-290, 1971.
- [10] W. Lauterborn and H. Bolle, "Experimental Investigation of Cavitation Bubble Collapse in The Neighbourhood of a Solid Boundary," *Journal of Fluid Mechanics*, vol. 72, no. 2, pp. 391-399, 1975.
- [11] H. M. Fitzpatrick and M. Strasberg, "Hydrodynamic Sources of Sound," in *Proceedings of 1st Symposium on Naval Hydrodynamics*, Washington, 1956.
- [12] W. K. Blake, *Mechanics of Flow-Induced Sound and Vibration*, vol. 1, Orlando, Florida: Academic Press, 1986.
- [13] C. S. Martin, H. Medlarz, D. C. Wiggert and C. Brennen, "Cavitation Inception in Spool Valves," *Transactions of the ASME: Journal of Fluid Engineering*, vol. 103, pp. 564-576, 1981.
- [14] S. L. Ceccio and C. E. Brennen, "Observations of the Dynamics and Acoustics of Travelling Bubble Cavitation," *Journal of Fluid Mechanics*, vol. 233, pp. 633-660, 1991.

- [15] E. A. Arndt, "Cavitation in Fluid Machinery and Hydraulic Structures," *Annual Review of Fluid Mechanics*, vol. 13, pp. 273-328, 1981.
- [16] V. P. Carey, *Liquid-Vapour Phase Change Phenomena*, Bristol, PA: Taylor & Francis, 1992.
- [17] R. T. Knapp, J. W. Daily and F. G. Hamitt, *Cavitation*, New York: McGraw-Hill, 1970.
- [18] D. Thoma, "Die Kavitation der Wasserturbinen," *Wasserkraftjahrbuch*, pp. 409-420, 1924.
- [19] J. Katz, "Cavitation Phenomena Within Regions of Flow Separation," *Journal Of Fluid Mechanics*, vol. 140, pp. 397-436, 1984.
- [20] K. K. Ooi, "Scale Effects on Cavitation Inception in Submerged Water Jets: a New Look," *Journal of Fluid Mechanics*, vol. 151, pp. 367-390, 1985.
- [21] T. J. O'Hern, "An Experimental Investigation of Turbulent Shear Flow Cavitation," *Journal of Fluid Mechanics*, vol. 215, pp. 365-391, 1990.
- [22] B. Ran and J. Katz, "Pressure Fluctuations and Their Effect on Cavitation Inception Within Water Jets," *Journal of Fluid Mechanics*, vol. 262, pp. 223-263, 1994.
- [23] Y. Kuhn de Chizelle, S. L. Ceccio and C. E. Brennen, "Observation and Scalling of

- Travelling Bubbles," *Journal of Fluid Mechanics*, vol. 293, pp. 99-126, 1995.
- [24] B. Belahadji, J. P. Franc and J. M. Michel, "Cavitation in The Rotational Structures of a Turbulent Wake," *Journal Of Fluid Mechanics*, pp. 383-403, 1995.
- [25] S. Gopalan, J. Katz and O. Knio, "The Flow Structure in The Near Field of Jets and Its Effects on Cavitation Inception," *Journal of Fluid Mechanics*, vol. 398, pp. 1-43, 1999.
- [26] C. O. Lyer and S. L. Ceccio, "The Influence of Developed Cavitation on the Flow of a Turbulent Shear Layer," *Physics of Fluids*, vol. 14, no. 10, pp. 3414-3431, 2002.
- [27] V. Aeschlimann, S. Barre and H. Djeridi, "Velocity Field Analysis in an Experimental Cavitating Mixing Layer," *Physics of Fluids*, vol. 23, no. 5, pp. 055105 (1-15), 2011.
- [28] L. Alfayez, D. Mba and G. Dyson, "The Application of Acoustic Emission for Detecting Incipient Cavitation and The Best Efficiency Point of a 60 kW Centrifugal Pump: Case Study," *NDT&E International*, vol. 38, pp. 354-358, 2005.
- [29] J. Cernetic, "The Use of Noise and Vibration Signals for Detecting Cavitation in Kinetic Pumps," *Proceedings of the Institution of Mechanical Engineers, Part C: Journal of Mechanical Engineering Science*, vol. 223, pp. 1645-1655, 2009.
- [30] K. Takahashi, H. Matsuda and H. Miyamoto, "Cavitation Characteristics of

Restriction Orifices," 2001.

[31] K. Sato and Y. Saito, "Unstable Cavitation Behavior in a Circular-Cylindrical Orifice Flow," in *Fourth International Symposium on Cavitation*, Pasadena, CA, 2001.

[32] Y. S. Liu, Y. Huang and Z. Y. Li, "Experimental Investigation of Flow and Cavitation Characteristics of a Two-Step Throttle in Water Hydraulic Valves," *Proceedings of the Institution of Mechanical Engineers, Part A: Journal of Power and Energy*, vol. 2016, pp. 105-111, 2002.

[33] X. Fu, L. Lu, X. Ruan, J. Zou and X. Du, "Noise Properties in Spool Valves with Cavitating Flow," in *Intelligent Robotics and Applications, Lecture Notes in Computer Science*, vol. 5315, Berlin Heidelberg, Springer-Verlag, 2008, pp. 1241-1249.

[34] X. Fu, L. Lu, X. Du and J. Zou, "Investigation on Cavitation Behaviour and Noise in Hydraulic Valves," in *Proceedings of the 7th JFPS International Symposium on Fluid Power*, Toyama, 2008.

[35] J. Zou, X. Fu, X. W. Du, X. D. Ruan, H. Ji, S. Ryu and M. Ochai, "Cavitation in a Non-circular Opening Spool Valves with U Grooves," vol. 222, pp. 413-420, 2008.

[36] A. Osterman, M. Hocevar, B. Sirok and M. Dular, "Characterization of Incipient Cavitation in Axial Valve by Hydrophone and Visualisation," *Experimental Thermal and Fluid Sciences*, vol. 33, pp. 620-629, 2009.

- [37] S. Mizuyama, M. Murase, Y. Fujii and Y. Yagi, "Detection of Cavitation With Accelerometers Mounted on Piping Outer Surface," *Journal of Environment and engineering*, vol. 5, no. 1, pp. 200-212, 2010.
- [38] Y. Nagaya, M. Murase and S. Mizuyama, "Detection of Cavitation with Microphones Placed Outside Piping," *Journal of Environment and Engineering*, vol. 6, no. 2, pp. 427-438, 2011.
- [39] Y. Nagaya and M. Murase, "Detection of Cavitation with Directional Microphones Placed Outside Piping," *Nuclear Engineering and Design*, vol. 249, pp. 140-145, 2012.
- [40] P. Merati, M. Macelt and R. Erickson, "Flow Investigations Around a V-sector Ball Valve," *Transactions of ASME: Journal of Fluid Engineering*, vol. 123, pp. 662-671, 2001.
- [41] M. J. Chern and C. C. Wang, "Control of Volumetric Flow Rate of Ball Valve Using V-port," *Transactions of The ASME: Journal of The Fluids Engineering*, vol. 126, pp. 471-481, 2004.
- [42] M. J. Chern, C. C. Wang and C. H. Ma, "Performance Test and Flow Visualization of Ball Valve," *Experimental Thermal and Fluid Sciences*, vol. 31, pp. 505-512, 2007.

- [43] J. A. Davis and M. Stewart, "Predicting Globe Control Valve Performance—Part I: CFD Modelling," *Transactions of The ASME, Journal of Fluids Engineering*, vol. 124, pp. 772-777, September 2002.
- [44] S. W. Kim, J. H. Kim, Y. D. Choi and Y. H. Lee, "Flow Characteristics of Butterfly Valves by PIV and CFD," *Proceedings of the Fifth International Conference on Fluid Mechanics*, 15-19 August 2007.
- [45] A. Ozdomar, K. Turgut Gursel, Y. Pekbey and B. Celikag, "An Experimental and Numerical Study on Pressure Drop Coefficient of Ball valves," *International Energy Journal*, vol. 8, 2007.
- [46] S. F. Moujaes and R. Jagan, "3D CFD Predictions and Experimental Comparisons of Pressure Drop in a Ball Valve at Different Partial Openings in Turbulent Flow," *Journal of Energy Engineering*, vol. 134, no. 1, pp. 24-28, March 2008.
- [47] S. F. Moujaes and S. Deshmukh, "Three-Dimensional CFD Predications and Experimental Comparison of Pressure Drop of Some Common Pipe Fittings in Turbulent Flow," *Journal of Energy Engineering*, vol. 132, no. 2, pp. 61-66, 2006.
- [48] A. H. Glenn and G. Decker, "Using Computational Fluid Dynamics To Predict The Onset of Cavitation (xFz)," in *Valve World Conference*, Maastricht, Netherlands, 2008.

[49] ANSI/ISA–S75.02, "Control Valve Capacity Test Procedures," American National Standard, 1996.

[50] S. Smith, "The Scientist and Engineer's Guide to Digital Signal Processing," California Technical Publishing, 2011.

[51] ANSYS Inc., "ANSYS Fluent User's Guide 14.0," ANSYS Inc., Canonsburg, PA, 2011.

[52] F. R. Menter, "Two-Equation Eddy-Viscosity Turbulence Models for Engineering Applications," *AIAA Journal*, vol. 32, no. 8, August 1994.

[53] D. C. Wilcox, "Re-assessment of the Scale-determining Equation for Advanced Turbulence Models," *AIAA Journal*, vol. 26, no. 11, pp. 1299-1310, 1988.

[54] C. K. Lam and K. Bremhorst, "A Modified Form of The k-e Model for Predicting Wall Turbulence," *Journal of Fluids Engineering*, vol. 103, no. 3, pp. 456-460, 1981.

[55] S. J. Kline and F. A. McClintock, "Describing Uncertainties in Single-Sample Experiments," *Mechanical Engineering*, vol. 75, pp. 3-8, 1953.